



Computational Design and Characterization of New Battery Materials

Mýrdal, Jón Steinar Garðarsson

Publication date:
2013

Document Version
Publisher's PDF, also known as Version of record

[Link back to DTU Orbit](#)

Citation (APA):
Mýrdal, J. S. G. (2013). *Computational Design and Characterization of New Battery Materials*. Department of Energy Conversion and Storage, Technical University of Denmark.

General rights

Copyright and moral rights for the publications made accessible in the public portal are retained by the authors and/or other copyright owners and it is a condition of accessing publications that users recognise and abide by the legal requirements associated with these rights.

- Users may download and print one copy of any publication from the public portal for the purpose of private study or research.
- You may not further distribute the material or use it for any profit-making activity or commercial gain
- You may freely distribute the URL identifying the publication in the public portal

If you believe that this document breaches copyright please contact us providing details, and we will remove access to the work immediately and investigate your claim.

Jón Steinar Garðarsson Mýrdal

Computational Design and Characterization of New Battery Materials

Submitted in candidacy for the degree Doctor of Philosophy

Supervisors

Tejs Vegge, DTU Energy Conversion

Jan Rossmeisl, DTU Physics

Computational Design and Characterization of New Battery Materials

Author

Jón Steinar Garðarsson Mýrdal

E-mail: jsmy@dtu.dk

Supervisors

Assoc. Prof. Tejs Vegge

Atomic scale Modeling and Materials

DTU Energy Conversion and Storage

Technical University of Denmark

E-mail: teve@dtu.dk

Assoc. Prof. Jan Rossmeisl

Center for Atomic-scale Materials Design

DTU Physics

Technical University of Denmark

E-mail: jross@dtu.dk

Atomic Scale Modeling and Materials, DTU Energy Conversion and Storage

Technical University of Denmark

Frederiksborgvej 399

DK-4000 Roskilde

Denmark

www.ecs.dtu.dk

Tel: (+45) 46 77 58 00

E-mail: info@ecs.dtu.dk

Center for Atomic-scale Materials Design, DTU Physics

Technical University of Denmark

Fysikvej 311

DK-2800 Kongens Lyngby

Denmark

www.camd.dtu.dk

Tel: (+45) 45 25 32 24

E-mail: info@camd.dtu.dk

Release date: December 14th, 2012

Preface

This thesis is submitted in candidacy for the Ph.D. degree from the Technical University of Denmark (DTU). The work was carried out between September 2009 and December 2012 at the section for Atomic-scale Modeling and Materials, DTU Energy Conversion and at the Center for Atomic-scale Material Design, DTU Physics, both at the Technical University of Denmark. A part of the work was also carried out in two external research stays, first at Prof. Orimos laboratory at the Institute for Material Research, Tohoku University in Sendai, Japan and later with the SUNCAT group at the Center for Interface Science and Catalysis, SLAC National Accelerator Laboratory, Menlo Park, CA, USA. The project was supervised by Assoc. Prof. Tejs Vegge, Head of Section at DTU Energy Conversion and Assoc. Prof. Jan Rossmeisl at DTU Physics. The project was financially supported by DTU Energy Conversion (previously AFM, Risø DTU), DTU Physics (CAMD), Copenhagen Graduate School for Nanoscience and Nanotechnology (C.O.N.T.) and the ReLiAble project

Abstract

This thesis is dedicated to the investigation and design of new functional materials for energy storage. The focus of the presented work is on components for the successful Li-ion and the promising Li-air batteries.

First principle density function theory calculations are applied to screening studies for new materials, as well as to more detailed investigations on interesting properties of different battery components. In the screening studies simple predictors are used to search for desired material properties and reduce the number of materials that need to be studied in more detail.

Solid electrolytes are believed to increase safety in Li based batteries as they would prevent metallic growth in the electrolyte. LiBH_4 has a solid superionic conducting HT phase that is stable above 390 K. The HT phase can be stabilized at room temperature with substitution of I into the LiBH_4 structure. Here we show how the stabilization of the HT phase can be described with calculations of relative structural stability. Relative structural stability is then used as a descriptor in a screening study, searching for new stable solid ionic conductors that could be used in an all solid state battery. The mechanisms for ionic conduction in the HT phase of LiBH_4 is studied with the nudged elastic band method and harmonic transition state theory. The results show that the high ionic conductivity originates from formation of Li interstitial and vacancy defects and the high mobility of the defects in the HT phase.

It is hoped that high energy dense Li-air batteries will be able to replace Li-ion batteries in the future. There are however number of challenge that need to be solved before that can happen. We have studied the growth and decomposition of Li_2O_2 , which is the main discharge product of Li- O_2 batteries. The results show that both growth during discharge and decomposition during charge can take place at low overpotentials. The energy of formation and the diffusion rate of V_{Li} in bulk Li_2O_2 are calculated and the effect the vacancies have on electronic conductance in the semiconducting Li_2O_2 is discussed. Finally we have studied adsorption of S and SO_2 on Li_2O_2 ($1\bar{1}00$) and (0001) surfaces. We show that SO_2 binds preferably to step ($1\bar{1}00$) sites and makes discharge growth close to the step less favorable. The possibility of using selective poisoning with SO_2 to control the growth of Li_2O_2 is discussed.

Resumé

Denne afhandling omhandler undersøgelse og design af nye funktionelle materialer til energilagring med særlig fokus på allerede anvendte Li-ion batterier og lovende Li-luft batterier.

Tæthedsfunktional teori (DFT) beregninger er anvendt til screening af nye materialer samt til mere detaljerede undersøgelser af forskellige batterityper med interessante egenskaber. I screeningsundersøgelserne anvendtes simple markører i søgningen efter de ønskede materialeegenskaber for at reducere antallet af materialer, der skulle undersøges nærmere.

Faststof elektrolytter menes at øge sikkerheden i Li baserede batterier, da de vil forhindre vækst af metallisk Li gennem elektrolytten. LiBH_4 er et superionisk ledende faststof med en højtemperatur (HT) fase, der er stabil over 390 K. HT fasen kan stabiliseres ved stuetemperatur ved substitution af BH_4 med I i LiBH_4 strukturen. Vi viser her hvordan stabiliseringen af HT fasen kan beskrives med beregninger af den relative strukturelle stabilitet. Den relative strukturestabilitet anvendes derefter som en deskriptor i en screeningsundersøgelsen efter nye stabile faste ionledere, der kan anvendes i faststof batterier. Mekanismerne for ionledning i LiBH_4 HT fasen er studeret med nudged elastic band metoden og harmonic transition state theory. Resultaterne viser, at den høje ioniske ledningsevne stammer fra dannelsen af Li i interstitielle positioner og deraf følgende Li vakancer. Disse Frenkel defektpar giver den høje defektmobilitet i HT fasen.

Li-luft batterier kan forhåbentlig, qua deres høje teoretiske energitæthed, erstatte Li-ion batterier i fremtiden. Der er dog mange udfordringer, som skal løses, før det kan ske. Vi har undersøgt dannelse og opløsning af Li_2O_2 , som er det primære afladningsprodukt i Li- O_2 batterier. Resultaterne viser, at både væksten under afladning og opløsningen under opladning kan foregå ved lave overpotentialer. Dannelsesvarmen og diffusionshastigheden af V_{Li} i bulk Li_2O_2 er beregnet, og den virkning vakancerne har på den elektroniske ledningsevne i den halvledende Li_2O_2 er diskuteret. Endelig har vi undersøgt adsorption af S og SO_2 på Li_2O_2 (1 $\bar{1}$ 00) og (0001) overfladerne. Vi demonstrerer at SO_2 fortrinsvis binder til step (1 $\bar{1}$ 00) sites, hvilket giver en mindre gunstig vækst af Li_2O_2 tæt på disse step sites. Muligheden for at anvende en sådan selektiv SO_2 forgiftning med henblik på at kontrollere væksten af Li_2O_2 er diskuteret.

Acknowledgements

The three years I have lived in Denmark and studied at DTU have truly been a wonderful time. I've had the challenges I needed to grow academically and hopefully also as a person. I have had the opportunity to travel to many new places and gained many good friends along the way. Therefore, there are many I would like to thank for making this time as educational and enjoyable as it turned out to be. So thanks go to

My supervisors, Tejs Vegge and Jan Rossmeisl for making my stay and this project a possibility. Also, special thanks to Tejs for keeping me motivated when things were uphill, for being a infinite source of new ideas and for great guidance and enjoyable collaboration.

My colleagues both at Risø and CAMD for a good working environment and fun times. Special thanks to Steen, Daði, Didier and Nonni for good collaboration and help along the way and to Steen, Daði and Rune for the help with proof-reading and translation help for the thesis.

Prof. Shin-Ichi Orimo and all the members of his research group for opening up their doors for my visit to Tohoku University and for making the visit as good as it was.

Prof. Jens K. Nørskov and other member of the SUNCAT group at SLAC for warm welcomes during my visit.

The computer staff at CAMD, Ole, Marcin and Jens Jørgen for great work at keeping the computers crunching seamlessly and for always be willing to give a helping hand.

Lene Danielsen for always finding a solution to my, sometimes unnecessarily complicated, problems with a smile on her face.

My family for all their support through the years and Þórveig for all the good times, despite long times apart and for the patience during busy months leading up to this thesis.

Lastly but not least, the members of the secret bicycle gang The Black Leopards.

Copenhagen, December 14th, 2012
Jón Steinar Garðarsson Mýrdal

Contents

Preface	v
Abstract	vii
Resumé / Ágrip	ix
Acknowledgements	xi
List of Figures	xv
List of Tables	xvii
1 Introduction	1
1.1 Ideology of This Work	2
1.1.1 Computational Screening	2
1.2 Outline of Thesis	3
2 Theory	7
2.1 Overview	7
2.2 Electronic Structure Calculations	7
2.2.1 Born Oppenheimer Approximation	7
2.2.2 Density Functional Theory	8
2.3 Chemical Rates	11
2.3.1 The Problem of Different Time-Scales.	11
2.3.2 Transition State Theory	12
2.3.3 Methods for Finding Saddle Points	13
2.4 Free Energy	14
2.4.1 Free Energy Diagrams	14
3 Solid Electrolytes	17
3.1 Introduction	17
3.1.1 Fast Ionic Conduction in LiBH_4	17
3.1.2 Stabilizing LiBH_4 's High Temperature Structure	18
3.1.3 The High Temperature Structure of LiBH_4	19
3.1.4 New Structures	19

3.1.5	Chapter Outline	19
3.2	Predicting the Stability of $\text{Li}(\text{BH}_4)_{1-x}\text{I}_x$ Solid Solutions	20
3.2.1	Computational Parameters	21
3.2.2	Results and Discussions	21
3.3	Mechanisms for Li^+ Conduction in $\text{Li}(\text{BH}_4)_{1-x}\text{I}_x$ Solid Solutions	22
3.3.1	Computational Parameters	24
3.3.2	Defect Free Conduction Mechanisms	25
3.3.3	Lithium Defects in $\text{Li}(\text{BH}_4)_{1-x}\text{I}_x$ Solid Solution.	26
3.3.4	Diffusion of Lithium Defects in the $\text{Li}(\text{BH}_4)_{1-x}\text{I}_x$ Solid Solution.	30
3.3.5	Comparison to QENS	32
3.4	Screening for New Solid Electrolytes	33
3.4.1	Computational Parameters	34
3.4.2	Mixed Alkali Borohydrides	34
3.4.3	Transition Metal Substitution	37
3.4.4	$\text{LiBH}_4\text{-LiBF}_4$	39
3.4.5	$\text{LiBH}_4\text{-LiI-LiNH}_2$	40
3.5	Solid Electrolytes Conclusions	43
4	Li-Air	45
4.1	Introduction	45
4.1.1	The Li- O_2 Battery	45
4.1.2	Challenges to Overcome	46
4.1.3	Chapter Outline	46
4.2	Reaction Mechanisms on Li_2O_2 Surfaces	46
4.2.1	Computational Parameters	48
4.2.2	Screening Setup	48
4.2.3	4 Step Mechanisms	49
4.2.4	6 Step Mechanisms	50
4.2.5	Recent Findings	51
4.3	O_2 Reaction Barriers	52
4.4	The role of Li Vacancies in Li_2O_2 Electronic Transport	54
4.5	Selective Sulfur Poisoning	56
4.6	Summary	57
	Bibliography	59
	Papers	68
	Paper A	71
	Paper B	81
	Paper C	107
	Paper D	115

List of Figures

2.1	Example of a free energy diagram. The diagram shows oxygen reduction on a Pt(111) surface. The diagram shows that even though the equilibrium potential is 1.23 V then 0.78 V is the highest potential the reaction runs at with all the steps as exothermic.	15
3.1	Temperature dependence of the conductivity of LiBH_4 .	18
3.2	High ($P6_3mc$) and low ($Pnma$) temperature structures of LiBH_4 .	20
3.3	Relative structural stability of $\text{LiBH}_4\text{-LiI}$.	22
3.4	Relative energy as a function of transition temperature for $\text{LiBH}_4\text{-LiI}$.	23
3.5	HT structure of $\text{Li}(\text{BH}_4)_{0.75}\text{I}_{0.25}$.	24
3.6	Minimum energy path for a Li^+ row mechanism in the LiBH_4 HT phase.	25
3.7	Minimum energy paths for row mechanism in $\text{Li}(\text{BH}_4)_{0.75}\text{I}_{0.25}$ HT phase.	27
3.8	Minimum energy path or a Li^+ row mechanism in $\text{Li}(\text{BH}_4)_{0.75}\text{I}_{0.25}$ LT structure.	28
3.9	A single atom dimer search in $\text{Li}(\text{BH}_4)_{0.75}\text{I}_{0.25}$ HT phase.	29
3.10	Minimum energy path for the formation of a Frenkel pair and the corresponding atomic structure.	30
3.11	Minimum energy path for a Li_{int}^+ jump from a 1/3 to a 2/3 site, passing through a 1/3* site.	33
3.12	Minimum energy path for a V_{Li}^- hopping from an I^- to an I^- site.	34
3.13	Relative structural stability in alkali borohydrides.	35
3.14	Relative structural stability in $\text{LiBH}_4\text{-NaBH}_4$.	36
3.15	Relative structural stability in $\text{LiBH}_4\text{-KBH}_4$.	37
3.16	Relative structural stability in $\text{LiBH}_4\text{-CsBH}_4$.	38
3.17	Relative structural stability in $\text{NaBH}_4\text{-KBH}_4$.	39
3.18	Impedance measurements on LiBH_4 , NaBH_4 and a 50/50 mixture of the two.	40
3.19	Relative structural stability in transition metal substituted LiBH_4 .	41
3.20	Relative structural stability in $\text{LiBH}_4\text{-AgBH}_4$.	41
3.21	Relative structural stability in $\text{LiBH}_4\text{-LiBF}_4$.	42
3.22	Schematic phase diagram of $\text{LiBH}_4\text{-LiI-LiNH}_2$ system.	42

3.23	Crystal structure of $\text{Li}_3(\text{NH}_2)_2\text{I}$	43
3.24	Alloy stability of $\text{Li}_3(\text{NH}_2)_{(2-x)}(\text{BH}_4)_x\text{I}$	44
4.1	Discharge-charge cycle for an aprotic Li-O ₂ cell	47
4.2	3x3x1 repetition of the calculation supercell of a stepped Li ₂ O ₂ (1 $\bar{1}$ 00) surface.	49
4.3	Free energy diagram for discharge and charge at a stepped Li ₂ O ₂ (1 $\bar{1}$ 00) surface.	51
4.4	A free energy diagram for discharge and charge at a stepped Li ₂ O ₂ (1 $\bar{1}$ 00) surface.	52
4.5	Translational and rotational freedom of O ₂	54
4.6	A minimum free energy path for removal of O ₂ from a stepped Li ₂ O ₂ surface.	55
4.7	The minimum energy path for V _{Li} diffusion in bulk Li ₂ O ₂	56

List of Tables

1.1	Energy density and specific energy of different energy storage mediums.	2
3.1	Formation and relative energies of lithium defects	31
3.2	Transition barriers, jump lengths and rates for lithium defects. . .	32
3.3	Atomic and ionic radii.	38

The work presented in this thesis has been carried out in 3 continents and in a number of different countries. Being able to do this kind of work without being tied to a specific workplace is made possible by a number of different technological progresses carried out in the last couple of decades, one of them being the development of high energy density batteries. The fact that you can carry with you all the tools you need to perform your work and communicate with your coworkers, from where you want to be at any given time, is a valuable freedom we have gained with the mobilization of electronic devices. A mobilization, that can be argued to have started by the introduction of the Li-ion battery in the early 1990's [1, 2].

Even though batteries are the dominating energy storage medium in hand-held devices, they have certain limitations when it comes to more energy demanding applications. An example of this is electric vehicles, where batteries are in competition with fossil fuels or hydrogen fuel cells. In this comparison, it turns out that what we refer to as high energy density when we talk about batteries is low when compared to chemical fuels (see table 1.1). In the table the energy density and specific energy for a few energy storage solutions are displayed, not in the favor of batteries. Batteries do, however, possess an advantage that evens this comparison out slightly, that is the high efficiency compared to the chemical fuels. With efficiency of around 90% [3] compared to about 20-30% and 60-70% for internal combustion engines and fuel cells respectively, batteries have the most sustainable energy cycle and lowest fuel cost. Still there is a big gap in the extractable energy densities between the Li-ion battery and the compared fuels. This has lead people to look for new battery chemistries and the high energy density of Li-metal has sparked the interest in developing Li-air batteries. A few other challenges face the Li-ion battery, such as limited cycle lifetime and safety concerns regarding metallic growth in liquid electrolytes. In this thesis we will discuss the possibility of using solid electrolytes in Li-based batteries as well as the emerging Li-air technology.

Table 1.1: Energy density and specific energy of different energy storage mediums. [4, 3]

Medium	Energy Density [kWh/L]	Specific Energy [kWh/kg]
Li-ion	0.3	0.2
H ₂ 200 bar	0.7	39.2
H ₂ liquid	2.8	39.2
H ₂ in LiBH ₄	4.0	6.0
Li-metal	12.0	11.7
Gasoline	9.3	13.3

1.1 Ideology of This Work

For the work presented in this thesis the goal was to combine the strengths of computational and experimental tools in a way that would make the search for and the investigation of new materials more effective. The way this is approached can be described as three steps:

- **Search for new materials.** Simple describing parameters are used to search for materials with specific properties. The goal of the study is to decrease the number of materials that need to be studied experimentally and thereby making the search for functional materials more effective.
- **Synthesis of promising materials.** Materials that are promising from the screening results are synthesized and measured.
- **Unexpected and interesting properties investigated.** Material properties that are unexpected or interesting in any way and seen from the original measurements are studied in more detail. Here computational and experimental techniques should be combine to get a more complete understanding of the studied properties.

1.1.1 Computational Screening

The fast improvements in computational resources and first principle modeling methods, like density functional theory (DFT), have made it possible to apply computational methods in material design.

Computational studies are generally significantly cheaper than experiments, meaning that in practice a much larger number of materials can be studied with simulations. The number of possible material compositions that are of interest for a given design criteria can be enormous and the ability to reduce possible candidates heavily, before experimental methods are applied, is valuable. Computer simulations are, however, based on models and therefore their results must always be verified with experiments.

Simulations and experiments give different insight into material properties and each have their strengths and weaknesses. In experiments the effects from external conditions, such as temperature, gas composition and applied potential

can easily be measured, but at the same time details at the atomic level can be hard to follow. For simulations this is almost opposite, atomic and electronic structure can be easily visualized and step by step information about reaction mechanisms can often be gathered. The simpler nature of atomic models, compared to real systems, can also make it easier to study the specific change with regards to composition, different adsorbates or defects. At the same time simulations have a hard time when it comes to study the effects from the macroscopic environment, temperature, pressure and etc.

The crystal structure of materials in screening studies is generally not known. It has, however, been shown that thermodynamic properties can be predicted with acceptable accuracy, using simple model structures [5]. Computational screening studies have been successfully applied for a number of different systems [6] and an example of such a study is a search for tetrahydroborates for hydrogen storage [7]. In the study 757 potential alloys were calculated and screened for alloy stability, e.g.

$$\Delta E_{\text{alloy}} = E_{\text{LiSc(BH}_4)_4} - (E_{\text{Li(BH}_4)} + E_{\text{Sc(BH}_4)_3}) \quad (1.1)$$

and stability against decomposition to highly stable components, e.g.

$$\Delta E_{\text{decomposition}} = E_{\text{LiMn(BH}_4)_3} - (E_{\text{LiH}} + E_{\text{Mn}} + 3E_{\text{B}} + 5.5E_{\text{H}_2}). \quad (1.2)$$

The screening resulted in 22 promising candidate materials, of which ~ 10 were considered highly promising. The results from the study agreed well with previously measured materials, even though in some cases the real atomic structure was different from the simulated model structure [7].

1.2 Outline of Thesis

The outline of the thesis is as follows:

- **Theory.** In the chapter the theoretical background of the work is presented, such as electronic structure calculations with DFT, reaction theory with the NEB and Dimer methods and calculations of free energy.
- **Solid Electrolytes.** The topic of this chapter is the design of new solid electrolytes and description of the mechanisms of ionic conduction in those materials. The recently discovered high conductivity of the high temperature LiBH₄ phase is discussed and work showing how DFT ground state calculations can predict the stabilization of the HT phase in a Li(BH₄)_(1-x)I_x solid solution is presented. The mechanisms for ionic conduction in the HT phase is shown to originate from high mobility of lithium defects in the structure. Finally a screening study on possible new solid electrolyte materials is presented. *The subject of this chapter is also discussed in Papers A and B.*
- **Li-Air.** In this chapter the Li-air battery technology is presented. Discharge and charging reaction mechanisms are studied at reactive Li₂O₂

surface sites and the effective potentials during discharge and charging are evaluated. The existence of a transition state for O_2 desorption is investigated, for a better understanding of Li_2O_2 decomposition during charging. The role of Li vacancies on electronic transport in bulk Li_2O_2 is discussed and the possibility of using selective surface poisoning to control Li_2O_2 growth is investigated. *The subject of this chapter is also discussed in Papers C and D.*

List of Included Publications

Paper A

The effect of heat treatment on the lithium ion conduction of the $\text{LiBH}_4\text{-LiI}$ solid solution

D. Sveinbjörnsson, J. S. G. Mýrdal, D. Blanchard, J. J. Bentzen, T. Hirata, M. B. Mogensen, P. Norby, S. Orimo, and T Vegge.
J. Phys. Chem. submitted (2012)

Paper B

Li-ion conduction in the $\text{LiBH}_4\text{-LiI}$ system from Density Functional Theory calculations and Quasi-Elastic Neutron Scattering

J. S. G. Mýrdal, D. Blanchard, D. Sveinbjörnsson, and T Vegge.
J. Phys. Chem. submitted (2012)

Paper C

The role of transition metal interfaces on the electronic transport in lithium-air batteries

J. Chen, J. S. Hummelshøj, K. S. Thygesen, J. S. G. Mýrdal, J. K. Nørskov, and T. Vegge.
Catalysis Today 165 (2011) 2-9

Paper D

DFT study of selective poisoning of Li-Air batteries for increased discharge capacity

J. S. G. Mýrdal, and T Vegge.
To be submitted

List of Publications Not Included

Bookchapter

Computational design of catalysts , electrolytes and materials for energy storage

T. Vegge, J. G. Howalt, S. Lysgaard, J. S. G. Mýrdal, N. Bork, and J. S. Hummelshøj

New and future developments in catalysis: Batteries, hydrogen storage and fuel cells

ed. S. L. Suib, Elsevier, (2013)

Paper E

DFT+U study of polaronic conduction in Li_2O_2 and Li_2CO_3 : Implications for Li-air batteries

J. M. Garcia-Lastra, J. S. G. Mýrdal, K. S. Thygesen and T. Vegge

J. Phys. Chem. *submitted* (2012)

Paper F

First principle investigation of zinc-anode dissolution in zinc/air battery

V. Tripković, S. Siahrostami, K. T. Lundgård, K. E. Jensen, H. A. Hansen, J. S. Hummelshøj, J. S. G. Mýrdal, T. Vegge, J. K. Nørskov, J. Rossmeisl

Phys. Chem. Chem. Phys. *submitted* (2012)

2.1 Overview

In this chapter the theoretical basis for the work presented in this thesis will be introduced. Density functional theory (DFT) is the main method used throughout the thesis, its origin and the implementation used here are discussed in the chapter. Then chapter continues with introduction to transition state theory and the methods that are used in this thesis find transition states. Finally free energy calculations are discussed.

2.2 Electronic Structure Calculations

A chemical system can be described with the time independent Schrödinger equation,

$$H\Psi = E\Psi. \quad (2.1)$$

Where H is the systems hamiltonian, the operator associated with the total energy of the given system. Ψ is the wave function describing the quantum state of the system and E is the energy for that state. By solving the Schrödinger equation it is possible to extract all observable material properties of the given system. But even though the Schrödinger equation looks simple in this form it is in fact only solvable analytically for two particle systems and numerically for only very few particles.

It is therefore clear that to do calculations on some reasonable chemical systems, some approximations must be done.

2.2.1 Born Oppenheimer Approximation

The mass of protons and neutrons are approximately 2000 times the mass of an electron. However, the dominating force on the atomic level is the coulomb force which acts equally on electrons and protons, having the same magnitude of charge. Because of this the electrons travel at a speed that is perhaps 3-5 orders of magnitude faster than the motion of much heavier nuclei. In most

cases it is therefore safe to assume that on the timescale of the nuclei motion the electrons will always have had time to reach their ground state. This assumption is the basis of the first approximation that is done in most electronic structure calculations, or the so called Born Oppenheimer approximation [8].

In the Born Oppenheimer approximation the total wave function of the system is split up into a electronic and a nuclear part

$$\Psi(\mathbf{r}, \mathbf{R}) = \phi(\mathbf{r}, \mathbf{R})\chi(\mathbf{R}), \quad (2.2)$$

where $\phi(\mathbf{r}, \mathbf{R})$ is the electronic part and $\chi(\mathbf{R})$ is the nuclear part and \mathbf{r} and \mathbf{R} are the electrons and nuclei positions respectively. For the electronic part it is assumed that the nuclei are fixed and therefore \mathbf{R} is a parameter, but not a variable. The electronic energy for a given nuclei positions is then given as

$$\hat{H}_e(\mathbf{r}, \mathbf{R})\phi(\mathbf{r}, \mathbf{R}) = E_e\phi(\mathbf{r}, \mathbf{R}). \quad (2.3)$$

This makes it possible to calculate the electronic energy E_e as a function of the nuclei positions \mathbf{R} generally referred to as the potential energy surface (PES).

After solving the electronic part of the system it is possible to go on and solve the quantum mechanical problem for the nuclei part as well. For the work in this thesis we will however stop here as the nuclei will be treated as classical particles moving on the PES.

2.2.2 Density Functional Theory

Density functional theory is today one of the most successful methods for solving the ground state electronic structure for realistic sized systems in solid state physics, quantum chemistry and surface science. Instead of the $3n_e$ dimension many-electron wave function $\phi(\mathbf{r}, \mathbf{R})$, DFT is based on the electron 3 dimensional electron density, $\rho(\mathbf{r})$.

In theory DFT is an exact method up to the Born Oppenheimer approximation, however in practice further approximations are needed to calculate the electronic ground state.

The Hohenberg-Kohn Theorems

For a known electronic state the electron density is given as

$$\rho(\mathbf{r}) = n \int |\phi(\mathbf{r}, \mathbf{R})|^2 d^3\mathbf{R}, \quad (2.4)$$

so by definition there is one and only one electron density for each electronic state. Until 1964 it was however not known if the opposite was true, but that year P. Hohenberg and W. Kohn published two theorems [9].

Theorem 2.1. (Hohenberg-Kohn 1, 1964) *The external potential $V(\mathbf{r})$ is uniquely determined by the corresponding ground-state electronic density $\rho(\mathbf{r})$, to within an additive constant.*

The theorem tells us that all of the systems properties are defined by the electron density. More precisely the ground state energy can in principle be written as a functional of the electron density

$$E[\rho(\mathbf{r})] = T[\rho(\mathbf{r})] + U[\rho(\mathbf{r})] + V[\rho(\mathbf{r})]. \quad (2.5)$$

Here the electronic energy has been separated into three parts, a kinetic part T , a electron-electron interaction part U and a part from the external potential (the fixed nuclei) V .

The theorem does however not tell us how this should be solved in practice but at the time of its publication it gave hope that such method could be constructed.

Theorem 2.2. (Hohenberg-Kohn 2, 1964) *For any trial density $\rho(\mathbf{r})$ it holds $E_0 \leq E[\rho(\mathbf{r})]$, where E_0 is the ground-state energy for the system.*

The second theorem then tells us that the ground state can be found in a variational way since the ground state electron density will always minimize $E[\rho(\mathbf{r})]$, or

$$E_0 = \min_{\rho} E[\rho(\mathbf{r})]. \quad (2.6)$$

The Kohn-Sham Equations

The next year, 1965, Kohn and Sham published a paper where they proposed a scheme for calculating the ground state electron energy from the density [10], this scheme is the basis for modern day DFT. [11]

First let us construct a system of N non-interacting electrons in an effective potential,

$$V_s = \int v_s(\mathbf{r})\rho(\mathbf{r})d^3\mathbf{r}, \quad (2.7)$$

that has the same ground state electron density $\rho_0(\mathbf{r})$ as a given interacting system. The total energy of the non-interacting system is then

$$E_s[\rho] = T_s[\rho] + \int v_s(\mathbf{r})\rho(\mathbf{r})d^3\mathbf{r} = \sum_i^N \epsilon_i, \quad (2.8)$$

which is just the sum of the energies for the individual particles and can be rewritten as

$$T_s[\rho] = \sum_i^N \epsilon_i - \int v_s(\mathbf{r})\rho(\mathbf{r})d^3\mathbf{r}. \quad (2.9)$$

Let us now write the total energy of the interacting system as

$$\begin{aligned} E[\rho] &= T_s[\rho] + U_H[\rho] + (T - T_s + U - U_H)[\rho] + V[\rho] \\ &= T_s[\rho] + U_H[\rho] + E_{xc}[\rho] + V[\rho]. \end{aligned} \quad (2.10)$$

Where $U_H[\rho]$ is the Hartree potential and $E_{xc}[\rho]$ is the exchange and correlation functional, which will be discussed later. Kohn and Sham showed that the derivative of the effective potential V_s can be written as

$$v_s(\mathbf{r}) = v(\mathbf{r}) + \int \frac{\rho(\mathbf{r}')}{|\mathbf{r} - \mathbf{r}'|} d^3\mathbf{r}' + v_{xc}(\mathbf{r}), \quad (2.11)$$

where

$$v_{xc}(\mathbf{r}) = \frac{\delta E_{xc}[\rho]}{\delta \rho(\mathbf{r})}. \quad (2.12)$$

By inserting an initial guess for the electron density into equation 2.11 it is possible to go on and solve the non-interacting problem

$$-\frac{\hbar^2}{2m_e} \nabla^2 \psi_i(\mathbf{r}) + v_s \psi_i(\mathbf{r}) = \varepsilon_i \psi_i(\mathbf{r}), \quad (2.13)$$

which again gives a new electron density

$$\rho(\mathbf{r}) = \sum_i^N |\psi_i(\mathbf{r})|^2. \quad (2.14)$$

Equations (2.11) and (2.13) are known as the Kohn-Sham equations. When they have been solved self consistently it is possible to calculate the ground state energy of the interactive system

$$E[\rho] = \sum_i^n \varepsilon_i - U_H[\rho] + E_{xc}[\rho] - \int v_{xc}(\mathbf{r}) \rho(\mathbf{r}) d^3\mathbf{r}. \quad (2.15)$$

Approximating the E_{xc}

As has been mentioned about DFT in general, here previously, the Kohn-Sham equations are in principle exact up to the Born-Oppenheimer approximation. But as is very evident from the last section then the Kohn-Sham scheme is written with approximations in mind, where all the parts that do not have a known solution are gathered into a single object, the exchange and correlation functional $E_{xc}[\rho]$

There are quite a few ways to approximate the $E_{xc}[\rho]$. The simplest one and originally the most popular is the local density approximation (LDA) [10]. In the LDA only the density at the coordinates where the functional is evaluated is used,

$$E_{xc}^{LDA} = \int \epsilon_{xc}(\rho) \rho(\mathbf{r}) d^3\mathbf{r}. \quad (2.16)$$

Here $\epsilon_{xc}(\rho)$ is the exchange correlation energy density of a homogeneous electron gas. The exchange part of the exchange and correlation energy density is known exactly but the correlation part has been mapped out with high accuracy quantum Monte-Carlo simulations [12]. The LDA, even for its simplicity has had great success, especially in solid state physics and is still widely used in that field. It is however not as good at calculating chemical bonds of molecules [13, 14].

A better description of molecular bonds can be reached by using the generalized gradient approximation (GGA). The GGA is similar to the LDA besides

that instead of only using the local density it also takes the densities gradient into account,

$$E_{xc}^{GGA} = \int \epsilon_{xc}(\rho_{\uparrow}, \rho_{\downarrow}, \nabla \rho_{\uparrow}, \nabla \rho_{\downarrow}) \rho(\mathbf{r}) d^3\mathbf{r}. \quad (2.17)$$

In contrast to the LDA there are many different parametrizations of the GGA, some fitting certain kind of chemical systems better than other. Among the more common once are the PW-91 [15], PBE [16] and RPBE [17]. PW-91 used to be almost the standard functional in physical science, but has been replaced by PBE in recent years. In the research presented in this thesis the PBE and the RPBE [17] functionals were used. But the RPBE functional is a revised version of PBE developed to describe surfaces and surface adsorption.

Hybrid functionals are another category of E_{xc} , that incorporates a portion of exact exchange from Hartree-Fock theory, to improve molecular properties such as atomization energies, bond lengths and vibration frequencies. Examples of hybrid functionals are B3LYP [18] and HSE [19]. B3LYP is one of the most commonly used functional in molecular calculations.

Implementation

There are different ways to implement DFT, the different implementations are generally first categorized by the choice of basis sets that are used. Most commonly used basis sets in DFT are either based on localized functions (e.g. gaussians) or plane waves.

The work presented here is performed with the DFT software GPAW unless otherwise stated. GPAW uses real-space basis sets that are calculated on a uniform grid [20, 21]. GPAW also uses the projector augmented wave method (PAW) [22, 23] to describe the non-valence electrons in a frozen core approximation. The real-space grid method gives the advantage of not having to use expensive fourier transformations as has to be done in the plane wave approach, giving more efficient parallelization. The PAW method is used since the inner electron are expensive to describe with the Kohn-Sham equations at the same time as they contribute little to the chemistry. The PAW method uses pseudo wave functions, from which physical properties can be extracted and is an all-electron method, with a frozen core approximation.

2.3 Chemical Rates

Chemical rates are an important part of understanding dynamical chemical events, like chemical reactions or diffusions in solid materials. This section is dedicated to discussing shortly the theory behind calculating chemical rates and the methods that are used to do so in this thesis.

2.3.1 The Problem of Different Time-Scales.

We are used to thinking of chemical reactions as something that happens fast, where the average time between reaction is often on the order of ms or even μs . From the viewpoint of an atom that is really not the case, as atomic vibrations

are happening at the timescale of tens of fs [24]. At this timescale the previously discussed chemical reactions become a very rare event.

Molecular modeling of such reactions are therefore computationally demanding since most of the simulation goes into atomic vibrations and small local re-ordering. Even though there are elegant methods to increase the probability of seeing reactions for certain or all species in the system [25, 26, 27], then it is hard to evaluate if the seen events are common or not.

But the problem of different timescales can be turned into an advantage since it opens up the possibility to treat the reactions in a statistical manner.

2.3.2 Transition State Theory

In transition state theory (TST) space is divided into areas around stable state, i.e. a reactants state (R) and at least one product state (P). The hypersurface separating the two is referred to as the transition state (TS). The TS should be devised in such a way that all reaction paths along the PES from R to P cross it. The basic assumption in TST is that the rate constant can be written as

$$k^{TST} = (\text{Probability of reaching the TS}) \times (\text{Flux through the TS}). \quad (2.18)$$

For this to be a good assumption few things must apply. Firstly the Born Oppenheimer approximation must hold, if that was not the case we could not construct a single PES that the trajectories from R to P will move along. Secondly classical dynamics must apply since the TST does not take quantum effects like tunneling into account. Thirdly the two states must be at thermal equilibrium, so Boltzmann distribution applies. As a rule of thumb this is usually a good approximation when $k_B T = E_{TS}/5$ [28]. The fourth and last criterion is that there should be no trajectory from R to P that crosses the TS more than once, this point is the one that is most likely to be broken. An example of this would be a trajectory crossing the TS but instead of going to P it would be reflected and return to R.

It can be a very difficult task to devise the hyperplanar TS, which is why we are going to do one more approximation.

Harmonic Transition State Theory

There exists a saddle point (SP), which is the lowest possible peak point along a trajectory between the two stable states R and P. In HTST we construct our TS around the SP and approximate the PES around the SP as harmonic. This leads to a great simplifications for the calculation of the rate as it becomes

$$k^{HTST} = \frac{\prod_i^{3N} \nu_{R,i}}{\prod_i^{3N-1} \nu_{SP,i}} e^{-\frac{(E_{SP}-E_R)}{k_B T}}, \quad (2.19)$$

where $\nu_{R,i}$ and $\nu_{SP,i}$ are the atomic vibrational frequencies at R and SP respectively [29]. The HTST expression of the rate constant agrees with the temperature dependence of the empirically seen Arrhenius equation [30, 31].

2.3.3 Methods for Finding Saddle Points

We have now reduced our problem from finding the whole TS hyperplane down to finding a SP. In this section two different methods for finding SP will be presented. The first one is a two point problem, that is both an initial and a final state need to be known, while in the second method only an initial state is needed.

Nudged Elastic Band Method

In the nudged elastic band (NEB) method an initial guess for a path between two stable states is mapped out with several images. If the energy for every images would be minimized, then, they would end up in either the initial or final state (unless there is a previously unknown stable state along the path).

To search for a minimum energy path between the initial and final state and to keep the images evenly distributed along the path an effective force is applied to all the images along the path,

$$\mathbf{F}_i^{\text{nudged}} = -\nabla V(\mathbf{R}_i)|_{\perp} + (\mathbf{F}_i^s \cdot \hat{\tau}_{\parallel})\hat{\tau}_{\parallel}. \quad (2.20)$$

The effective force only uses the component of the real force, $-\nabla V(\mathbf{R}_i)$, that is perpendicular to the tangent of the path,

$$\nabla V(\mathbf{R}_i)|_{\perp} = \nabla V(\mathbf{R}_i) - (\nabla V(\mathbf{R}_i) \cdot \hat{\tau}_{\parallel})\hat{\tau}_{\parallel}. \quad (2.21)$$

The spring force, \mathbf{F}_i^s , on the other hand provides the force component along the tangent of the path ($\hat{\tau}_{\parallel}$), keeping the image distribution even.

$$\mathbf{F}_i^s \equiv k_{i+1}(\mathbf{R}_{i+1} - \mathbf{R}_i) - k_i(\mathbf{R}_i - \mathbf{R}_{i-1}) \quad (2.22)$$

The effective force is now minimized for all the images simultaneously until a minimum energy path has been found [32, 33].

After the initial minimization we can not be sure that one of the images is lying at the SP. In the so called climbing image method of NEB [34] the image with highest energy is released from the spring constants and relax with regards to

$$\mathbf{F}_{max}^{\text{CI}} = -\nabla V(\mathbf{R}_{max}) + 2(\nabla V(\mathbf{R}_{max}) \cdot \hat{\tau}_{\parallel})\hat{\tau}_{\parallel}. \quad (2.23)$$

That is the SP is effectively changed into a minimum by reversing the force component in the direction of the path.

The Dimer Method

The basic idea behind the dimer method [35] is to find a SP by following the minimum eigenvalue mode of the Hessian,

$$H_{ij} = \frac{\partial^2 V}{\partial x_i \partial x_j}, \quad (2.24)$$

calculating the Hessian is however not an easy task. The clever idea behind the dimer method is to locate the minimum mode without having to calculate the Hessian directly [26].

The first thing that needs to be done is to shift the system out of the stable initial state, this is typically done with a random displacement to a point we shall call \mathbf{R}_0 . The second step is to create a pair of replicas (a dimer) of the system at an equal distance from \mathbf{R}_0 . The dimer which is allowed to rotate around \mathbf{R}_0 is then relaxed to find the direction of the minimum mode. The system is then relaxed towards a SP in a way analogous to what we previously saw in the CI-NEB method (equation 2.23). That is by effectively changing the force in such a way that the SP becomes a minimum.

2.4 Free Energy

The output from a DFT calculation is a total energy of the calculated system. To calculate reaction energies we simply subtract the energies of the reactants from the energies of the products. An example of this can be molecular adsorption on a surface, where the adsorption energy becomes

$$\Delta E_{\text{adsorption}} = E_{\text{surface+adsorbant}} - E_{\text{surface}} - E_{\text{adsorbant}} \quad (2.25)$$

Chemical reactions are governed by the free energy change over the reaction. We can calculate the free energy by considering the change in zero-point energy ΔZPE and entropy ΔS between the reactants and the products.

$$\Delta G = \Delta E + \Delta ZPE - T\Delta S \quad (2.26)$$

For reactions in and between solid materials the change in ΔZPE and ΔS is often small and ΔE becomes the dominating factor in chemical stability. On the other hand in reactions of molecules, especially from gas phase, the change in entropy can be substantial and needs to be taken into account. The ΔZPE and ΔS can be calculated from the eigen frequencies of the given system [36], where the frequencies are found with a finite difference approximation to the Hessian.

2.4.1 Free Energy Diagrams

Free energy diagrams where the reaction steps of a chemical process are plotted as a function of their free energy, are a helpful medium to visualize the roles and limitations of different steps along the process.

In case of electrochemical reactions the effect from an applied bias can be studied by using a standard electrode. The most commonly used is the standard hydrogen electrode, where the potential is defined to be zero ($U = 0$) when the reaction



is at equilibrium. At an applied potential, U , the free energy of a reaction is shifted by $-neU$, where n is the number of electrons that are to be reacted from the electrode [37].

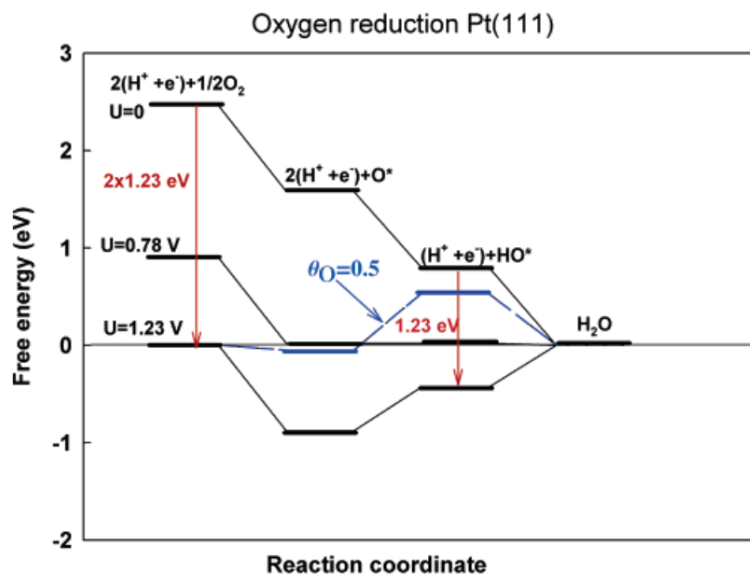


Figure 2.1: Example of a free energy diagram. The diagram shows oxygen reduction on Pt(111) surface. The diagram shows that even though the equilibrium potential is 1.23 V then 0.78 V is the highest potential the reaction runs at with all the steps as exothermic, the figure is from [37]

Figure (2.1) shows an example of such a free energy diagram. The figure shows O_2 reduction over Pt(111) surface. The diagram clearly shows that at the equilibrium potential, $U_0 = 1.23 \text{ V}$, two of the reaction steps have become endothermic. The highest potential at which all the steps are exothermic is $U_{\text{eff}} = 0.78 \text{ V}$. This simple approach, therefore, gives a clear insight into the origin of the experimentally seen overpotential, $U_{\text{eff}} - U_0 = 0.45 \text{ V}$ [37].

In the diagram no transition barriers are taken into account. This has been shown to be a good approximation for oxygen reduction reactions [37] and oxygen evolution reactions [38], but should be considered explicitly for every studied system. The approach has also been successfully applied in theoretical predictions of new catalysts for oxygen reduction [39] and hydrogen evolution [40].

3.1 Introduction

Lithium dendrite formation, i.e. a neural like network of metallic growth that can form at the anode/electrolyte solid/liquid interface during charging, is one of the main challenges in terms of safety and durability of the Li-ion battery technology, since they can short circuit the battery cell and cause the battery to catch on fire. This challenge is even more pronounced for higher energy density battery technologies using lithium anodes, e.g. Li-metal and Li-air batteries [41, 42, 43]. A possible solution to this problem is to use a solid electrolyte instead of the organic liquid electrolytes used today, since the dendrites would not be able to form in the solid.

A good electrolyte combines high ionic and poor electronic conductivity with high chemical and electrochemical stability, and is preferably lightweight. Among investigated materials for solid electrolytes are perovskite structured lithium lanthanum titanate [44, 45], NASICON [46, 47], LISICON [48], Thio-LISICON [49] and garnet-type $\text{Li}_5\text{La}_3\text{M}_2\text{O}_{12}$ metal oxides [50]. Kamaya et al. published the findings of $\text{Li}_{10}\text{GeP}_2\text{S}_{12}$ that shows conduction on the order of $10^{-2} \text{ S cm}^{-1}$ at room temperature, which is comparable to conventional organic liquid electrolytes [51].

3.1.1 Fast Ionic Conduction in LiBH_4

Lithium borohydride (LiBH_4) has been studied extensively as a material for hydrogen storage, because of its light weight and high hydrogen content. It has been found to possess an orthorhombic ($Pnma$) phase below approximately 390 K and a hexagonal ($P6_3mc$) phase above that temperature at ambient pressures [52, 53]. In 2007, M. Matsuo et al. reported that when lithium borohydride undergoes its structural transformation, the conductivity jumps three orders of magnitude (see figure 3.1) [54]. From ^7Li nuclear magnetic resonance (NMR) measurements it has been shown that the increased conductivity is caused by increased Li^+ motion [54, 55]. With an ionic conductivity around $10^{-3} \text{ S cm}^{-1}$ at the phase transition temperature, the high temperature phase of lithium

borohydride is classified as a superionic conductor [54]. Furthermore, M. Matsuo et al. reported that lithium borohydride has a large electrochemical window with no hydride decomposition up to an applied potential of 5 V [56]. The chemical stability can, however, be a problem, since LiBH_4 is a strong reducing agent when it comes in contact with e.g. oxides. This problem can, at least in some cases, be overcome by coating as Takahashi et al. showed recently when they made a stable all solid state battery cell with a LiBH_4 electrolyte and a LiCoO_2 cathode. In their reported cell the cathode was coated with 25 nm thick Li_3PO_4 layer [57]. Lithium borohydride would therefore be a good candidate for a solid electrolyte, if the high temperature phase was stable at room temperature.

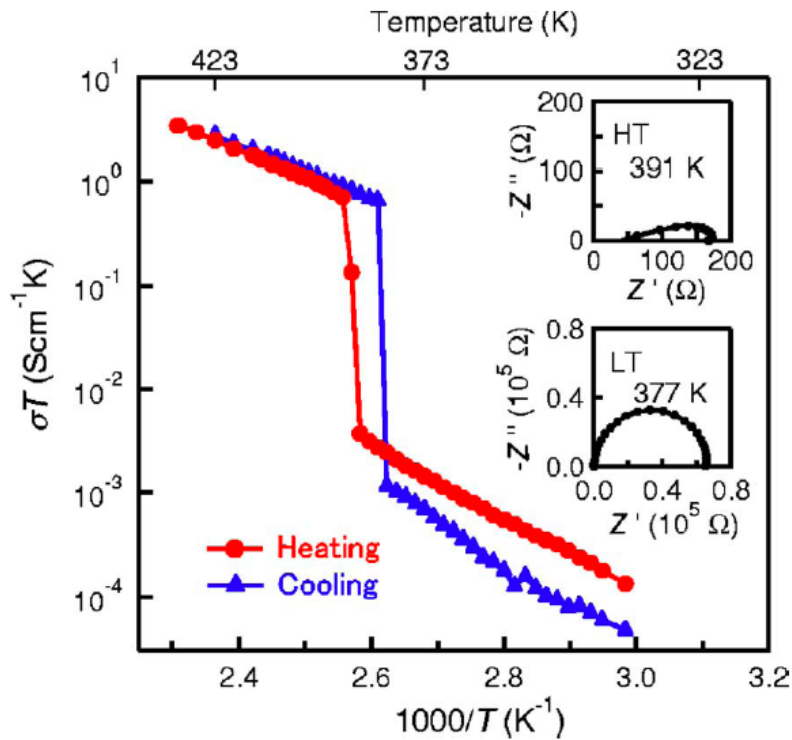


Figure 3.1: Temperature dependence of the conductivity of LiBH_4 . The phase transformation is very evident at around 390 K, where the conductivity jumps up three orders of magnitude. Figure is from [54].

3.1.2 Stabilizing LiBH_4 's High Temperature Structure

Maekawa et al. showed that by ball milling LiBH_4 with Li-Halides (Cl^- , Br^- , I^-) it is possible to lower the LiBH_4 phase transition temperature [58]. Mixtures of LiBH_4 and LiI show the highest conductivity and have been shown to form a solid solution [59]. In an investigation on the phase transition temperature and conductivity of the $\text{Li}(\text{BH}_4)_{(1-x)}\text{I}_x$ solid solution, Miyazaki et al. showed that the highest conductivity at room temperature was obtained with a LiBH_4 : LiI mixture in the ratio of 3:1 [60].

3.1.3 The High Temperature Structure of LiBH_4

The structure of the HT phase of LiBH_4 has been the cause of some debate. Original publications in the 70's referred to the structure as being tetragonal [61, 62]. Soulié et al. investigated the structure with X-ray diffraction and concluded that it belonged to the $P6_3mc$ spacegroup [63]. However, Lodziana et al. published their investigation on the structural stability of the HT structure from DFT calculations, concluding that the previously published $P6_3mc$ structure was unstable at finite temperature with respect to lattice vibrations. Instead they suggested a new structure with a Cc symmetry [64, 65].

Following the theoretical investigation the HT structure was revisited by neutron powder diffraction [66] and by synchrotron diffraction on single crystals and powder [67, 68]. The neutron studies support the $P6_3mc$ structure for the HT phase, but at the same time report orientational disorder of the BH_4 groups [69].

In his PhD thesis Jens S. Hummelshøj presents two possible Li sites along the c-axis, of the $P6_3mc$ structure, seen from DFT calculations [4]. The Li double splitting is further seen in the molecular dynamics simulations presented by Ikeshoji et al. [70] and Aeberhard et al. [71]. This double splitting is likely to be the origin of the dynamical instability seen in theoretical calculations.

In the work presented in this chapter, the structures used for the calculations on the HT phase are based on the structure presented by Filinchuk et al. [69]. The hexagonal $P6_3mc$ HT structure and the orthorhombic $Pnma$ LT structure of LiBH_4 can be seen in figure 3.2.

3.1.4 New Structures

Mixtures of LiBH_4 and LiNH_2 have two known stable phases, $\text{Li}_2(\text{BH}_4)(\text{NH}_2)$ and $\text{Li}_4(\text{BH}_4)(\text{NH}_2)_3$ [72, 73, 74, 75, 76, 77]. Although they have different anion configurations from LiBH_4 they both exhibit fast ionic conductivity at room temperature [78]. In addition to this Matsuo et al. have presented fast ionic conduction in $\text{Li}_3(\text{NH}_2)_2\text{I}$ in a Laves type structure [79]. This indicates that there is still a large phase space for searching for new materials based on LiBH_4 , LiI and LiNH_2 .

3.1.5 Chapter Outline

The outline of the work presented on solid electrolytes is as follows:

- **Predicting the Stability of $\text{Li}(\text{BH}_4)_{1-x}\text{I}_x$ solid solutions.** Calculations on the relative energy difference between the LT and HT structure of LiBH_4 as a function of iodine substitution into the structures are discussed. The calculations are compared to experiments and the possibility of using the energy difference as a descriptor for designing new solid electrolytes is discussed.
- **Mechanisms for Li^+ Conduction in $\text{Li}(\text{BH}_4)_{1-x}\text{I}_x$ solid solutions** Presents investigations on the origin of the super-ionic conductivity in the HT structure of LiBH_4 , after it has been stabilized with iodine. The role of

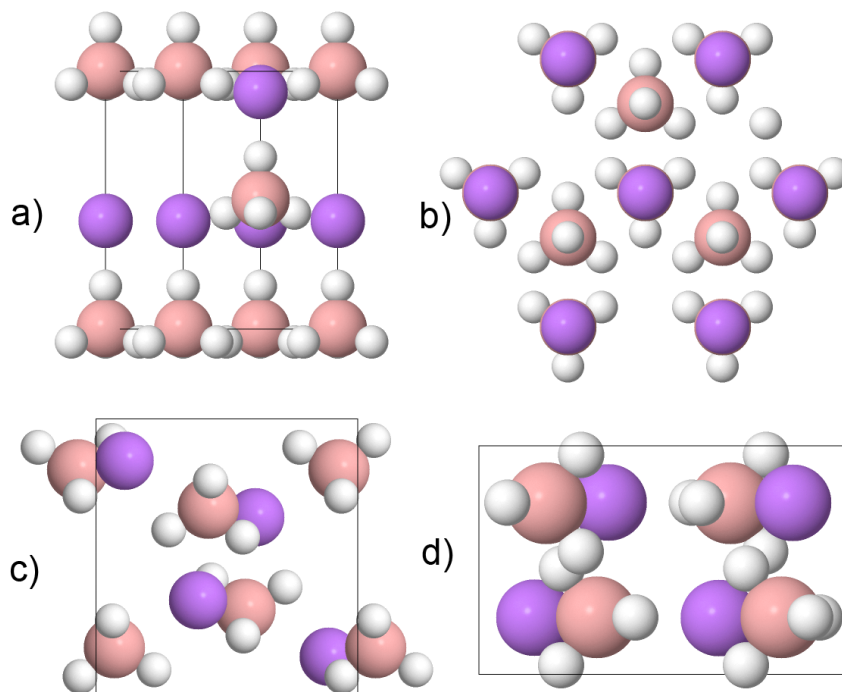


Figure 3.2: High ($P6_3mc$) and low ($Pnma$) temperature structures of LiBH_4 . a) Shows one unit cell and neighboring atoms of the HT structure from the side, b) shows the hexagonal structure of the HT phase from the top, c) shows one unit cell and neighboring atoms of the LT structure from the side, d) shows one unit cell and neighboring atoms of the LT structure from the top. Li: pale purple, B: pink and H white.

lithium defects is investigated and discussed and the results are compared to previous theoretical work and QENS measurements.

- **Screening for new Solid Electrolytes** Presents screening on the stability of LiBH_4 's HT structure, when Li is substituted with larger alkali metal atoms or transition metals as well as work done looking for stable compounds of LiBH_4 , LiI and LiNH_2

3.2 Predicting the Stability of $\text{Li}(\text{BH}_4)_{1-x}\text{I}_x$ Solid Solutions

The subject of this section is presented in paper A, but will be summarized here.

As was mentioned in this chapter's introduction, the HT phase of LiBH_4 can be stabilized with LiI , where the two form a solid solution of $\text{Li}(\text{BH}_4)_{1-x}\text{I}_x$ [59]. For the work in this chapter we were interested in seeing if a simple descriptor, like the ground state energy difference, could be used as a guide in the search for new solid electrolyte materials. The idea here is that the stability change, with increased concentration of iodine in the solid solution will be dominated by the relative change in ground state energy rather than entropy. If this is

true then the ground state energy can be used as a guide rather than the more computationally demanding free energy.

3.2.1 Computational Parameters

Calculations were performed using density functional theory as it is implemented in the Vienna Ab-initio Simulation Package (VASP) [80] with a plane wave basis set. All lithium electrons were used in the calculations. For other non-valence electrons the projector augmented wave method (PAW) [22, 23] was used. For exchange and correlation the PBE functional [16] was picked. The energy cut-off was set to 350 eV and a 4x4x4 Monkhorst-pack k-point mesh was used. The preparation of atomic structures and the setup of computational parameters was performed using the Atomic Simulation Environment (ASE) [81]. The ground state energy for the $\text{Li}(\text{BH}_4)_{(1-x)}\text{I}_x$ system was calculated for seven different values of x , that is $x = \{0, 1/16, 1/8, 3/16, 1/4, 1/2, 1\}$, in both the LT ($Pnma$) and HT ($P6_3mc$) crystal structures of LiBH_4 . For structural optimization all forces were relaxed down to < 0.01 eV/Å.

3.2.2 Results and Discussions

Figure 3.3 shows the calculated energy difference between the $P6_3mc$ HT and $Pnma$ LT structures as a function of iodine content in the $\text{Li}(\text{BH}_4)_{(1-x)}\text{LiI}_x$ solid solution. Up to a LiI content of 25%, there is a close to linear stabilization with increasing iodine content, about 33 kJ/mol I. There seems to be little addition in stability by going from 25% iodine content to 50%, but for pure LiI the HT structure has become more stable than the LT structure. This increased stability of the HT structure versus the LT structure is, however, a poor indicator of the real HT stability for pure LiI because the LT structure of LiBH_4 is not the ground state structure of LiI. We do, nonetheless, believe that for smaller iodine contents the ground state energy calculations give a good estimate of the real stabilization in the $\text{Li}(\text{BH}_4)_{(1-x)}\text{LiI}_x$ solid solution since we expect them to have a similar entropy behavior as a function of temperature.

In paper A we present differential scanning calorimetry (DSC) measurements on the transition temperature as a function of iodine ratio. In figure 3.4, the calculated energy differences $\Delta E(x)$ between the two phases are plotted against the transition temperatures measured using DSC. At each phase transition temperature the Gibbs free energy difference between the two phases is zero. Since contributions from the zero point energy difference and the volume change between the two phases are small, we set $\Delta H(x) \approx \Delta E(x)$, where $\Delta H(x)$ is the enthalpy change for a given ratio of iodine x . Therefore we can write

$$\Delta E(x) = T\Delta S(x). \quad (3.1)$$

For the iodine free system, the entropy difference between the two phases is the slope of the dashed line in figure 3.4, $\Delta S(0) = 34.7$ J/(mol K). If the addition of iodine was purely an enthalpy effect, $\Delta S(x)$ should remain constant for the different contents of iodine and all data points should fall on the dashed line. It is apparent that the entropy difference $\Delta S(x)$ is not a constant, but rather reduced with addition of iodine. The reduction is roughly 0.5 J/(mol K) per percentage

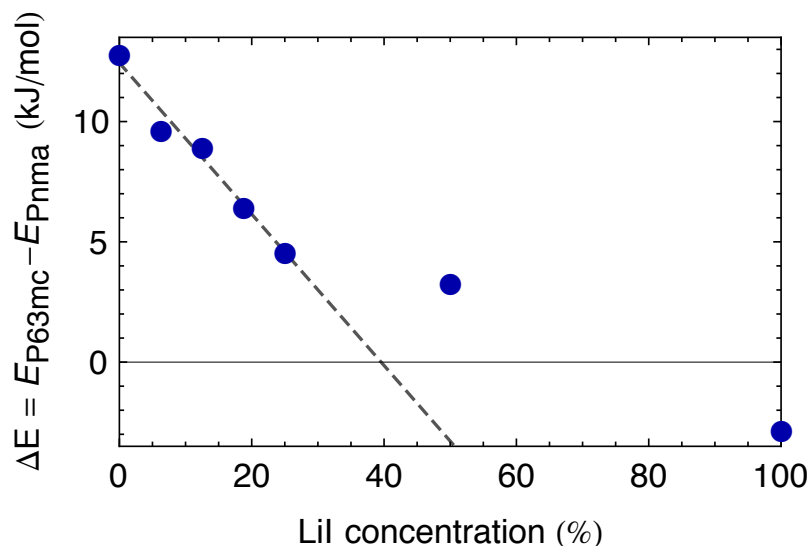


Figure 3.3: The ground state energy difference between the $P6_3mc$ (HT) and $Pnma$ (LT) structures of LiBH_4 as a function of the content of LiI that has been substituted into the system. The stabilization of the HT structure relative to the LT structure is approximately linear up to a LiI content of 25%. The dashed line shows a linear fit of the datapoints for LiI contents from 0% to 25% to emphasize this.

point of increased iodine content in the system, but it is not possible to quantify how much should be attributed to the changes in the LT or HT respectively, resulting from e.g. changes in directional bonding or configurational entropy.

The calculated value of $\Delta E(0) = 12.8 \text{ kJ}/(\text{mol K})$ is significantly higher than the published enthalpy values from Kharbachi et al. [82]. ($\Delta H_{Kharbachi} = 5.1 \text{ kJ}/(\text{mol K})$) and Gorbunov et al. [83]. ($\Delta H_{Gorbunov} = 6.2 \text{ kJ}/(\text{mol K})$). This overestimate of the ground state energy difference also leads to an overestimate of the entropy difference between the two phases. Our calculated value is $\Delta S(0) = 34.4 \text{ J}/(\text{mol K})$ compared to the published values from Pistorius et al. [61] ($\Delta S_{Pistorius} = 16.5 \text{ J}/(\text{mol K})$) and from Kharbachi et al. [82] ($\Delta S_{Kharbachi} = 13.1 \text{ J}/(\text{mol K})$). Assuming that $\Delta E(x)$ is similarly overestimated for other values of x , then $\Delta S(x)$ should probably be scaled down by a factor of 2.0-2.5.

Although $\Delta S(x)$ varies with iodine content, the governing factor in the stabilization of the HT phase comes from the change in the ground state energy difference $\Delta E(x)$. This suggests that $\Delta E(x)$ can be used as a predictor or a guide in the search for interesting materials for a more thorough investigation.

3.3 Mechanisms for Li^+ Conduction in $\text{Li}(\text{BH}_4)_{1-x}\text{I}_x$ Solid Solutions

In paper B we present the results from our DFT study on the conduction mechanisms in $\text{Li}(\text{BH}_4)_{1-x}\text{I}_x$ solid solutions, as well as our QENS measurements. In this section the theoretical part will be discussed in more detail, followed by a summary of the results from comparison of the two studies.

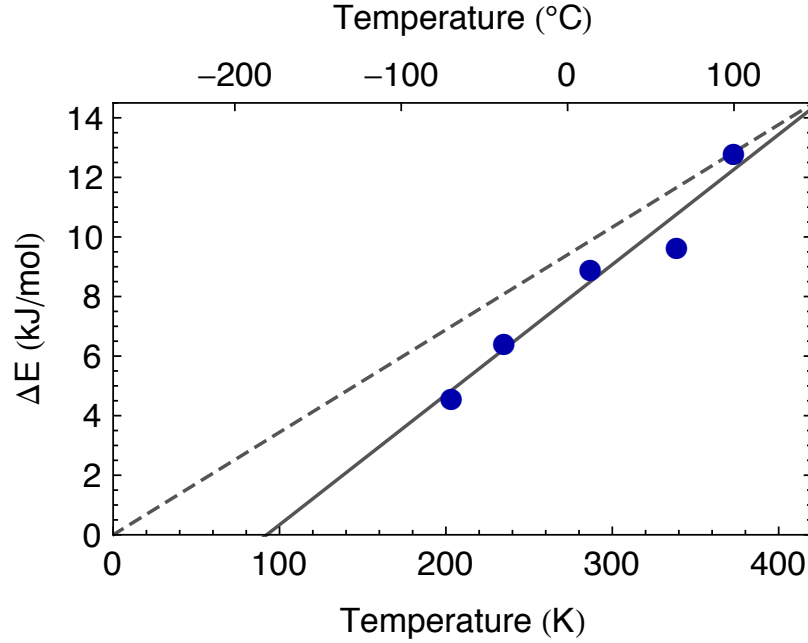


Figure 3.4: The calculated ground state energy difference between the HT and the LT structures, $\Delta E(x)$, for different iodine contents x as a function of the measured phase transition temperature. The slope of the dashed line gives the entropy for $x = 0$. In the limit of $\Delta S(x) = 0$, that is no change in entropy with increased iodine ratio, all the points should lie on the dashed line. The fitted line shows that this is not the case and $\Delta S(x)$ is decreased with increased concentration of iodine.

Beside the work presented in this chapter we know of two first principles studies on the ionic motion in the HT structure of LiBH_4 . Ikeshoji et al. [70] investigated the Li^+ motion with first principle molecular dynamics (FPMD). To increase the probability of seeing Li^+ hopping events, the atomic masses were scaled and the simulated temperature was raised to 560 K. The calculations were started from a defect free system of 200 formula units (f.u.) of LiBH_4 . During the 15 ps simulation time several Li^+ hopping events were observed. Frenkel pair formation, where a Li^+ leaves its lattice site forming an interstitial and a vacancy, was observed. Here the interstitial site was seen at approximately 2.5 Å distance away from the lattice site and the formation energy (FE) of the defect pair is evaluated as 0.29 eV. A diffusion process is suggested, in which a Frenkel pair is formed and a neighboring Li^+ moves into the vacancy. Hopping between hexagonal planes is also observed, where the transition barriers are seen as $E_{\text{TS}} = 0.31$ eV. Their conclusions discuss the Li^+ double splitting along the c-axis as an important factor in the high ionic conductivity.

Aeberhard et al. [84, 71] investigated the Li^+ motion, as well as the BH_4^- rotations, with ab initio molecular dynamics (AIMD). The AIMD results indicate a double splitting in the Li^+ along the c-axis, but also a smaller double splitting for the boron placement along the c-axis. They state that the BH_4 groups show no favorable orientation in the HT phase, while in the LT phase they follow C_2 and C_3 rotations. No Li^+ diffusion mechanisms were observed for the unaltered

MD. To observe the Li^+ hopping events they apply a non equilibrium AIMD method. From the NE-AIMD they report some lithium density in the interstitial region previously presented by Ikeshoji et al., as well as they present a similar diffusion mechanism.

3.3.1 Computational Parameters

All calculations presented here were prepared and executed using the Atomic Simulation Environment (ASE) [81]. We used the PBE exchange and correlation functional [16], a $4 \times 4 \times 4$ Monkhorst-pack k-point mesh and a grid spacing of 0.15 \AA . For ground state energy calculations the atomic positions were relaxed until all atomic forces were smaller than 0.01 eV/\AA . The formation of Li^+ interstitials, Li_{int}^+ , and vacancies, V_{Li}^- , have been studied by addition or removal respectively of Li^+ to the supercell, which was kept neutral by adding a uniform compensation charge.

The configuration of the iodide ions in the $\text{Li}(\text{BH}_4)_{0.75}\text{I}_{0.25}$ solid solution is not known. The model structure we use for the calculations on the HT phase is simply constructed by replacing one of the BH_4^- ions with an I^- ion in a $2 \times 1 \times 1$ lattice unit supercell (4 f.u.). The relaxed lattice unit lengths are $a = 4.31 \text{ \AA}$, $b = 4.19 \text{ \AA}$ and $c = 6.95 \text{ \AA}$. When performing calculations on lithium defects a larger supercell was used, consisting of $2 \times 2 \times 1$ lattice units for all calculated defects. The only exception to this was the calculation of a Frenkel pair defect, where a supercell of $4 \times 2 \times 1$ lattice units was used.

For the larger supercells there are several possible configurations of the I^- ions. We did, however, decide to stick with the same configuration as is present in the $2 \times 1 \times 1$ cell and its periodic images. The main reason for this is that, instead of having a uniform distribution of I^- through the cell, we now have different concentrations of I^- in different regions of the cell, see figure 3.5.

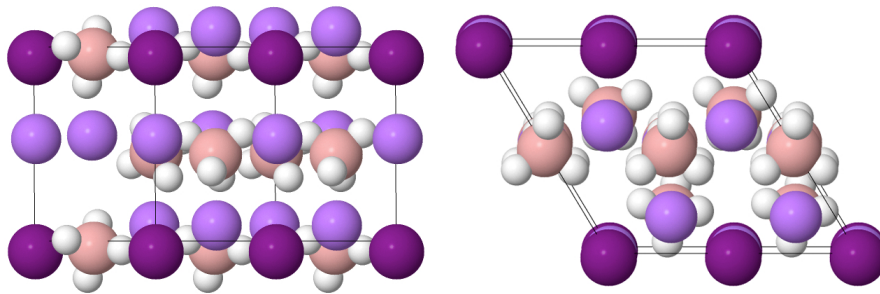


Figure 3.5: A $2 \times 2 \times 1$ lattice unit supercell of $\text{Li}(\text{BH}_4)_{0.75}\text{I}_{0.25}$ in the HT structure, along with few neighboring atoms. All defect calculations in the HT phase are performed with this model structure. The figure displays the difference in local environments in the structure; iodide rich areas close to neighboring I^- ions, iodide sparse areas in iodide free crystal planes and areas with moderate iodide concentration between neighboring BH_4^- and I^- ions. Li: pale purple, I: dark purple, B: pink and H white.

3.3.2 Defect Free Conduction Mechanisms

In the first calculations presented in this section we look at mechanisms where no defects are introduced in the system, beside the diffusing Li^+ ion. The mechanism is calculated in a $2 \times 1 \times 1$ supercell, where a Li^+ diffuses to an identical site in the next supercell. With the periodic boundary conditions, this effectively means that there is an infinite number of Li^+ ions diffusing in a row. We will, therefore, refer to the mechanism as a row-mechanism. This is of course not likely to happen in reality, simply since the statistical chance of a large number of ions moving in the same direction at the same time is very slim. We do, however, hope to get an initial feeling for the different barriers between the HT and the LT structures, as well as this might be a reasonable approximation to the event of few ions jumping one after another.

In figure 3.6 a NEB path for a row mechanism is presented for pure LiBH_4 in the HT structure. This figure shows very clearly the problem with doing calculations on the HT structure using 0 K ground state DFT calculations. The structure is only metastable and as soon as the Li^+ ion moves out of its lattice site, the total energy of the system is reduced. We are therefore completely unable to draw any conclusions from this calculation, since the transition barrier comes out as being more favorable than the initial and final states.

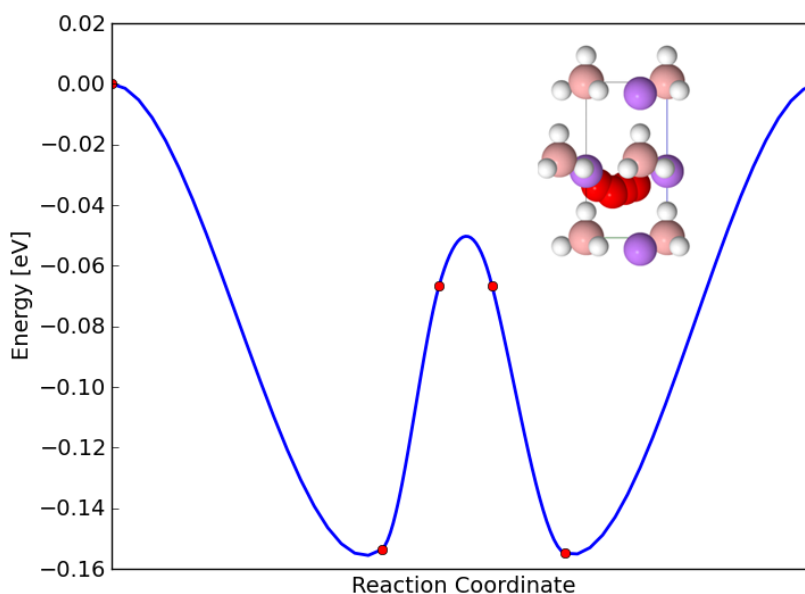


Figure 3.6: NEB minimum energy path for a Li^+ row mechanism in the LiBH_4 HT phase. The path clearly exhibits the problem of running calculations on the HT structure for pure LiBH_4 , as it is not stable and the system goes down in energy when the Li ion moves out of its crystal site. The inserted figure shows the presented path, where the red atoms are the Li ions along the path. Li: pale purple, I: dark purple, B: pink and H white.

As already presented in section ch:LiBH4cond the HT phase of LiBH_4 can be stabilized by substituting I^- into a part of the BH_4^- sites. In figure 3.7 we can

see the same row mechanism as in figure 3.6, except this time a 4th of the BH_4^- has been substituted with I^- . In the top figure the diffusing Li^+ is neighboring I^- in the surrounding layers, while in the bottom figure the Li^+ only has BH_4^- neighbors. The introduction of iodide in the system clearly stabilizes the HT structure, making the diffusion calculations possible. For the two cases presented here the HT structure, the diffusion in the neighborhood of I^- is more favorable with a transition barrier of $E_{\text{HT-I,TS}} = 0.17$ eV, while the second path gives $E_{\text{HT-BH}_4,\text{TS}} = 0.25$ eV.

In figure 3.8 a row mechanism in the LT structure is presented. Like for the more stable path in the HT structure, the diffusing Li^+ , has I neighbors. The transition barrier in LT structure is significantly higher than in the HT structure with $E_{\text{HT-BH}_4,\text{TS}} = 0.55$ eV.

3.3.3 Lithium Defects in $\text{Li}(\text{BH}_4)_{1-x}\text{I}_x$ Solid Solution.

It is quite clear that defects are either formed during Li^+ diffusion or that the diffusion is originated from them. For a solid electrolyte in a battery cell surface defects are constantly formed at the electrode/electrolyte interfaces when Li^+ is removed from or introduced to the electrolyte. We are, however, also interested in calculating the cost of forming defects inside the bulk material.

In figure 3.9 we see a path from a dimer calculation where only a single Li^+ ion is allowed to move during the simulation. The calculation shows two different minima along the path, in the first one the Li^+ has moved 0.94 \AA away from the initial lattice site and in the second one it has moved 2.76 \AA . The placement of the ion is shown at the different minima in the inserted figures as a red atom. According to the dimer run the formation energy of the defect pair is $E_{\text{F}} = 0.53$ eV and there is a substantial transition barrier with $E_{\text{TS}} = 0.71$ eV. Only allowing a single atom to move is, however, a very rough approximation and to get more reliable numbers we relaxed the system from the two new found minima. The first one did not turn out to be stable when all the atoms are allowed to move and relaxed back to the initial structure. For the second dimer minima it relaxed to a Frenkel pair state. In the relaxed Frenkel pair state the distance from the lattice site is increased up to 3.32 \AA and the formation energy is reduced to $E_{\text{F,Frenkel}} = 0.44$ eV. In figure 3.10 a NEB minimum energy path for the formation of the Frenkel pair is shown. As can be seen from the figure, then it is not only the formation energy that is reduced in the relaxed Frenkel pair state, but also the stability since, the transition state is sitting only 0.02 eV above the minimum with $E_{\text{TS,Frenkel}} = 0.46$ eV. The low stability of the defect agrees well with the reportings of Ikeshoji et al. [70], while in our calculations, the interstitial site of the Frenkel pair is positioned further away from the lattice site and the formation energy is somewhat higher.

$\text{Li}(\text{BH}_4)_{(1-x)}\text{I}_x$ is an ionic material and lithium defects in the system are therefore likely to be charged. Furthermore, it is clear that the material has some charged lithium defects, since they are the charge carrier in the material. It is easy to do calculations on the Frenkel pair defects since the pair consists of a positively charged Li_{int}^+ and a negatively charged V_{Li}^- , making the supercell charge neutral. Performing calculations on single charged defects can only be done by adding a uniform charge in the background to keep the supercell neutral.

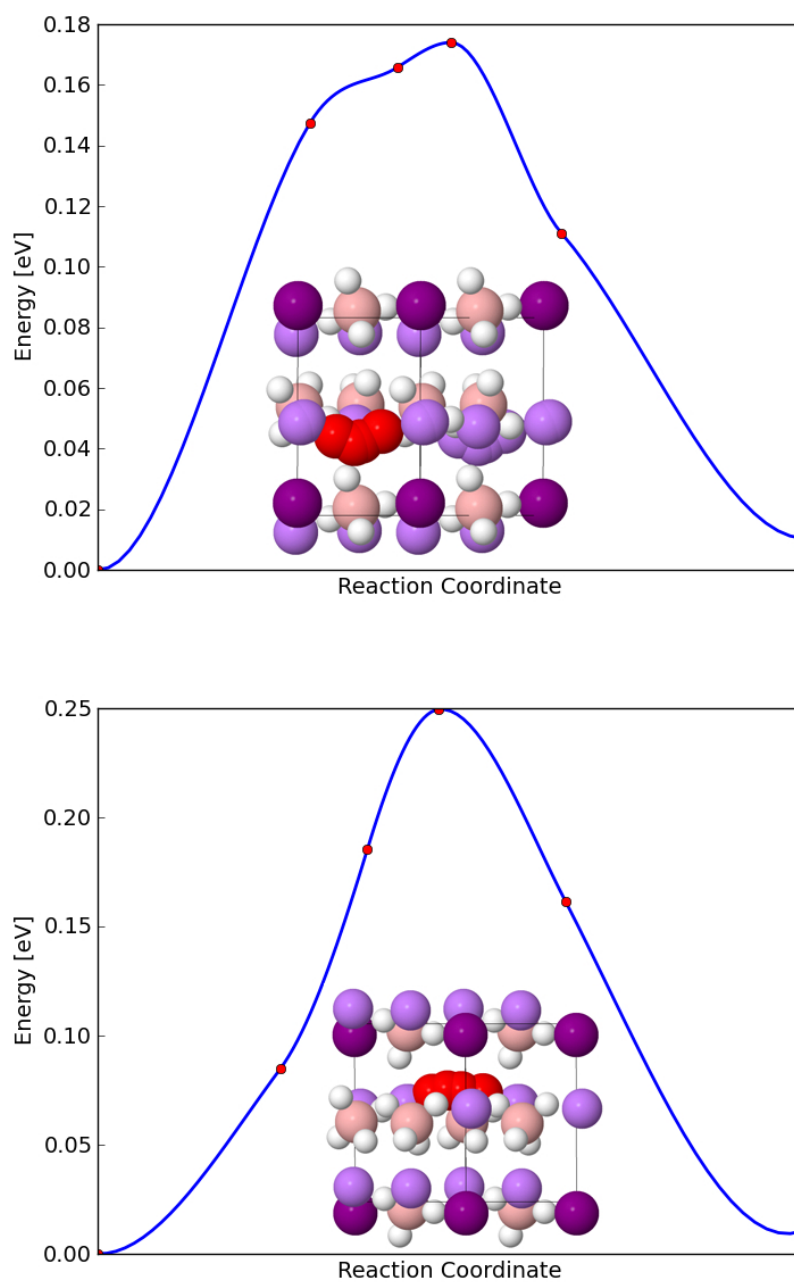


Figure 3.7: NEB minimum energy paths for a Li^+ row mechanism in $\text{Li}(\text{BH}_4)_{0.75}\text{I}_{0.25}$, in the hexagonal HT structure. Opposite to the pure LiBH_4 the path shows stable initial and final states, giving us usable barriers. The top figure shows a path for a Li^+ with iodide neighbors above and below. The transition barrier for the first path is $E_{\text{TS}} = 0.17$ eV. The bottom figure shows a path for a Li^+ with only BH_4 nearest neighbors. The transition barrier for the second path is higher than for the first one, $E_{\text{TS}} = 0.25$ eV. Moving Li: red, other Li: pale purple, I: dark purple, B: pink and H white.

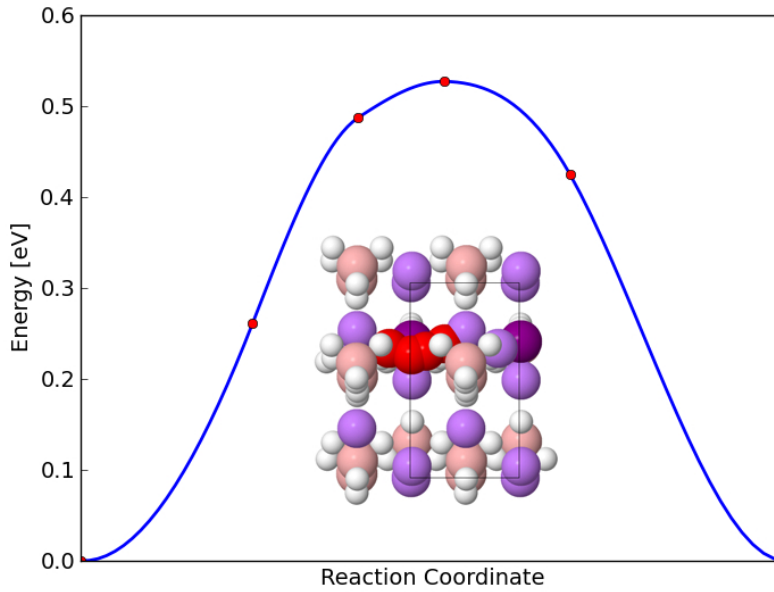


Figure 3.8: NEB path for a Li^+ row mechanism in $\text{Li}(\text{BH}_4)_{0.75}\text{I}_{0.25}$, in the orthorhombic LT structure. The figure shows a path between iodide neighboring sites. The transition barrier in the LT structure is significantly higher than the analogous paths in the HT phase, with a transition barrier of $E_{\text{TS}} = 0.55$ eV. Moving Li: red, other Li: pale purple, I: dark purple, B: pink and H white.

It is not trivial how formation energy for the charged defect should be calculated since there is no obvious reference for the added charge. Therefore, we will only discuss the relative stability of the single charged defects in this section.

We have not only performed calculations on charged Li_{int}^+ and V_{Li}^- , but also on charge neutral Li_{int} and V_{Li} . The main reason for doing calculations on the charge neutral defects is to see if the addition of charge will affect the diffusion mechanisms greatly. For the charge neutral defects we will evaluate the FE in accordance with equation 2.25.

In the HT hexagonal crystal structure, triangular areas exist between all groups of three neighboring Li^+ ions. Each Li^+ ion has an anion neighbor placed directly below it, about 2.5 \AA for the pure BH_4^- layers and about 2.9 \AA for the layers that include I^- . Together these neighboring an- and cations form a triangular prism. The crystal layers then have a ABAB stacking, which means that centered above (about 0.8 \AA) every other triangular prism there is an anion from the next layer (see figures 3.5, 3.10 and 3.11). We performed calculations on Li_{int} and Li_{int}^+ interstitials placed inside these triangular prism structures with 3 different local environments. We will refer to the 3 calculated sites as 1/3, 2/3 and 3/3 sites. For Li_{int}^+ we also performed calculations on a site we will refer to as the 1/3* site. The labeling refers to the ratio of surrounding BH_4^- ions in the prism grid (see figure 3.11). The first three sites do not have ions from the neighboring crystal planes positions directly above or below the site, while the 1/3* site is centered between ions from neighboring layers. In

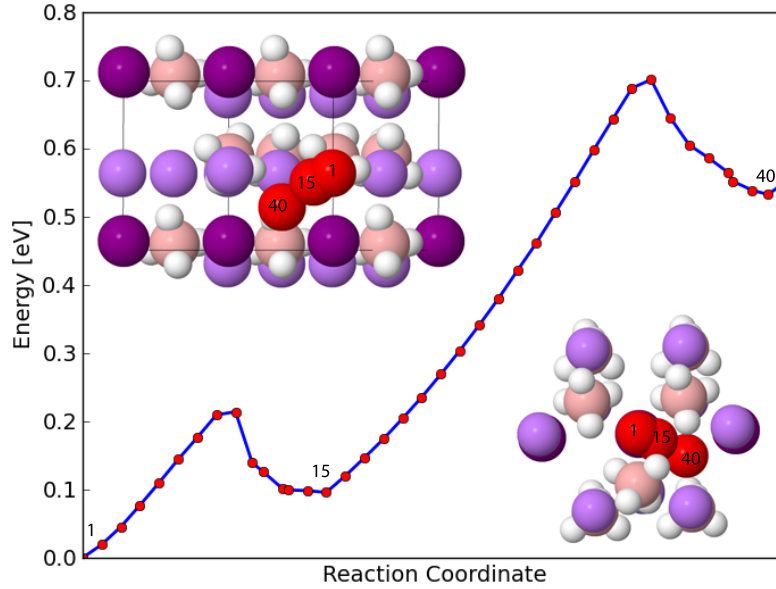


Figure 3.9: A dimer search from defect free $\text{Li}(\text{BH}_4)_{0.75}\text{I}_{0.25}$. For the dimer run only the red atom is allowed to move. The dimer finds two new minima in the run, where a frenkel pair is created. In the inserted figures the moving atom along the dimer is shown, as red atom, at the three different minima along the path, that is at the initial image and at images 15 and 40. Other atoms are Li: pale purple, I: dark purple, B: pink and H white.

the three non-"sandwiched" sites, the interstitials can be found about 0.8-1.1 Å above (differs between ratios of I- neighbors) the central position between the three neighboring anions in the hexagonal plane. In the $1/3^*$ site the Li_{int}^+ is located significantly closer to the two neighboring I^- ions than the in plane BH_4^- ion. Calculations were performed on V_{Li} and V_{Li}^- vacancies in two different local environments, i.e. with a neighboring I^- ion (an iodide site) and a second site without iodide neighbors (a BH_4^- site).

The FEs of neutral defects and relative stability of all comparable defects can be seen in table 3.1. Compared to the low cost of forming the Frenkel pair ($E_{\text{F,Frenkel}} = 0.44$ eV), the cost of forming the neutral Li_{int} and V_{Li} is very high, with the most favorable interstitial site being the $1/3$ site with $E_{\text{F,neutral } 1/3} = 1.34$ eV. The formation energies of V_{Li} are even higher with $E_{\text{F,neutral I}} = 3.58$ eV. This suggests that forming the neutral defects is more expensive than forming charged defects (Frenkel pair). We do, however, need to be careful since possible errors in the reference energy, which in this case is lithium metal, would shift the FE of the neutral defects. Another possible explanation for the large difference in FE between the single neutral defects and the Frenkel pair is that the defects gain stability from being close to each other. We investigated this briefly by calculating the state where the vacancy and the interstitial in the Frenkel pair are separated by one lattice unit. This extended Frenkel pair is only slightly less favorable, 0.10 eV, than the previously calculated structure and can therefore

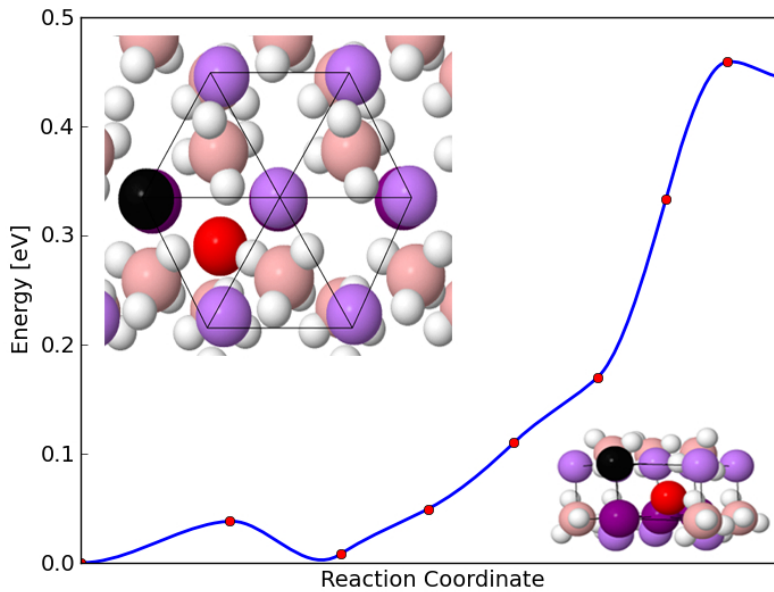


Figure 3.10: The minimum energy path for the formation of a Frenkel pair and the corresponding atomic structure. The created Li^+ interstitial, seated in a 1/3 site, and vacancy are shown as red and black spheres respectively. The transition barrier for creating the defect pair is 0.46 eV. The non-defect atoms are displayed as follows; Li: pale purple, I: dark purple, B: pink and H: white.

not explain the large energy difference.

For Li_{int}^+ the 1/3 site is energetically the most favorable, while the 3/3 and the 2/3 sites are almost equal in energy being 0.14 eV and 0.15 eV, respectively, less favorable than the 1/3 site. The 1/3* site is the least favorable, 0.18 eV less favorable than the 1/3 site. For the neutral Li_{int} defects the relative stability between the sites is similar, with the main difference being that the 2/3 site is 0.26 eV less stable than the 1/3 site. For the neutral vacancies the I^- site is 0.10 eV more favorable than the BH_4^- site. This is reversed for the charged vacancy where the BH_4^- site becomes more favorable, but the energy difference is small, 0.05 eV.

3.3.4 Diffusion of Lithium Defects in the $\text{Li}(\text{BH}_4)_{1-x}\text{I}_x$ Solid Solution.

The next step was to investigate how mobile the different defects are in the $\text{Li}(\text{BH}_4)_{1-x}\text{I}_x$ solid solution. We performed NEB calculations on different possible diffusion mechanisms for Li and Li^+ interstitials and vacancies. All transition state energies, jump lengths and reaction rates are presented in table 3.2.

Li_{int}^+ and/or Li_{int} conduction mechanisms were calculated from a 1/3 site to the four different sites. A Li_{int}^+ jump from a 1/3 site to an identical site, one lattice unit away, has a transition barrier of $E_{1/3-1/3,\text{TS}} = 0.26$ eV. During the jump, a clear shift of a neighboring non-defect Li^+ ion, of about 0.6 Å is visible along the c-axis to make room for the diffusing interstitial. Similarly, a

Table 3.1: Formation and relative energies of neutral Li_{int} and V_{Li} and relative energies of Li_{int}^+ and V_{Li}^- .

Site	$E_{\text{F,Neutral}}$ [eV]	$\Delta E_{\text{Neutral}}$ [eV]	$\Delta E_{\text{Charged}}$ [eV]
Li_{int}			
1/3	1.34	0	0
2/3	1.60	0.26	0.15
3/3	1.50	0.16	0.14
1/3*	-	-	0.18
V_{Li}			
I^-	3.58	0	0.05
BH_4^-	3.68	0.10	0

rotational motion of neighboring BH_4^- ions around the c-axis and in the direction following the moving interstitial is visible. There were difficulties getting the NEB calculation for the same mechanism for the neutral Li_{int} to converge and therefore there are no numbers presented from that calculation. We investigated whether the diffusion between 1/3 sites could take place through an exchange mechanism, where a lattice ion moves from its lattice site to a 1/3 interstitial site while the interstitial ion moves into the lattice site. This exchange mechanism turns out to be significantly more expensive than the single particle jump, with a transition barrier of $E_{\text{exchange,TS}} = 0.44$ eV for Li_{int} . The exchange gives two different jump lengths, 3.00 Å for the non-defect ion moving to the interstitial site and 4.07 Å for the interstitial moving into the lattice site.

An interstitial jump from a 1/3 site to a 2/3 site has a similar barrier as the jump between 1/3 sites with $E_{1/3-2/3,\text{TS}} = 0.28$ eV for Li_{int}^+ and only 0.02 eV higher for Li_{int} . Since the 2/3 site is less stable than the 1/3 site for both Li_{int}^+ and Li_{int} , the transition barrier for going from 2/3 to 1/3 site is lower, with $E_{2/3-1/3,\text{TS}} = 0.14$ eV for Li_{int}^+ and 0.04 eV for Li_{int} .

The 1/3* site lies in between the 1/3 and the 2/3 sites and since the transition barrier for going from the 1/3 site to the 1/3* site is only $E_{1/3-1/3*,\text{TS}} = 0.20$ eV, there is a possibility that at low temperature the interstitials will equilibrate in the shallow 1/3* site. If the interstitial is then to continue from the 1/3* site to the 2/3 site it has to overcome a second transition barrier of $E_{1/3*-2/3,\text{TS}} = 0.09$ eV. It is however more likely that the interstitial will move back to the 1/3 site since the 1/3* site's stability towards the 1/3 site is very low ($E_{1/3*-1/3,\text{TS}} = 0.02$ eV). Figure 3.11 shows the calculated minimum energy path for a Li_{int}^+ moving to the 1/3* site and then continuing to the 2/3 site.

A jump from a 1/3 site to a 3/3 site is different from the previously addressed jumps since it is a jump between crystal planes, while the others are jumps in the same hexagonal plane. Going from the 1/3 site to the 3/3 site gives $E_{1/3-3/3,\text{TS}} = 0.32$ eV for Li_{int}^+ and 0.34 eV for Li_{int} , while for the opposite direction we get $E_{3/3-1/3,\text{TS}} = 0.18$ eV in both cases.

V_{Li} and V_{Li}^- diffusion calculations were performed for a jump between two I^- sites as well as a jump between an I^- site and a BH_4^- site. The transition

Table 3.2: Calculated transition barriers, jump lengths and rates for different diffusion mechanisms in the $\text{Li}(\text{BH}_4)_{0.75}\text{I}_{0.25}$ system. All mechanisms are single particle jumps except for the exchange mechanism. Different transition barriers depending on the direction of the jumps are caused by relative energy differences between different sites.

Defect	Mechanism	Transition Barrier [eV]	Jump length [\AA]	Rate 300 K [s^{-1}]	Rate 380 K [s^{-1}]
Li_{int}	1/3 to 2/3	0.30/0.04	4.88	2e+08	2e+09
	1/3 to 3/3	0.34/0.18	4.36	5e+07	7e+08
	Exch. 1/3	0.44	3.00/4.07	9e+05	3e+07
Li_{int}^+	1/3 to 1/3	0.26	4.32	1e+09	8e+09
	1/3 to 2/3	0.28/0.14	4.31	5e+08	4e+09
	1/3 to 3/3	0.32/0.18	3.85	1e+08	1e+09
	1/3 to 1/3*	0.20/0.02	2.34	7e+09	4e+10
	1/3* to 2/3	0.09/0.15	3.30	8e+12	9.e+12
V_{Li}	I^- to I^-	0.26	4.30	1e+09	8e+09
	I^- to BH_4^-	0.33/0.22	4.57	7e+07	1e+09
V_{Li}^-	I^- to I^-	0.23	4.27	3e+09	2e+10
	I^- to BH_4^-	0.33/0.28	4.27	7e+07	1e+09

barrier between the I^- sites comes out as $E_{\text{I-I,TS}} = 0.23$ eV for V_{Li}^- and 0.26 eV for V_{Li} , while the barriers for the second mechanism are $E_{\text{I-BH}_4,\text{TS}} = 0.33$ eV for both cases and $E_{\text{BH}_4-\text{I,TS}} = 0.28$ eV and 0.22 eV for V_{Li}^- and V_{Li} respectively. The calculated minimum energy path for the V_{Li}^- diffusion between two I^- sites is shown in figure 3.12.

The difference of transition barriers between the charge neutral and charged calculations is very small and does not change the overall picture we have of the conduction mechanisms for the defects. The presented rates are calculated from HTST as it is presented in equation 2.19.

3.3.5 Comparison to QENS

The results from the DFT calculations fit very nicely with the quasi-elastic neutron scattering (QENS) measurements at 380 K (presented in paper B). The QENS data suggests diffusion mechanisms with jump lengths of around one lattice unit length and the rate of the measured diffusion without applying a potential is $k_{380\text{K},0\text{V}}^{\text{QENS}} = 8.3 \times 10^9 \text{ s}^{-1}$. This agrees well with the calculated rates for interstitial in-plane diffusion. It does also not exclude the vacancy diffusion, or the cross plane interstitial diffusion and most likely the measured value is a combination if them all.

The measurements at 300 K tell a quite different story. Although they give

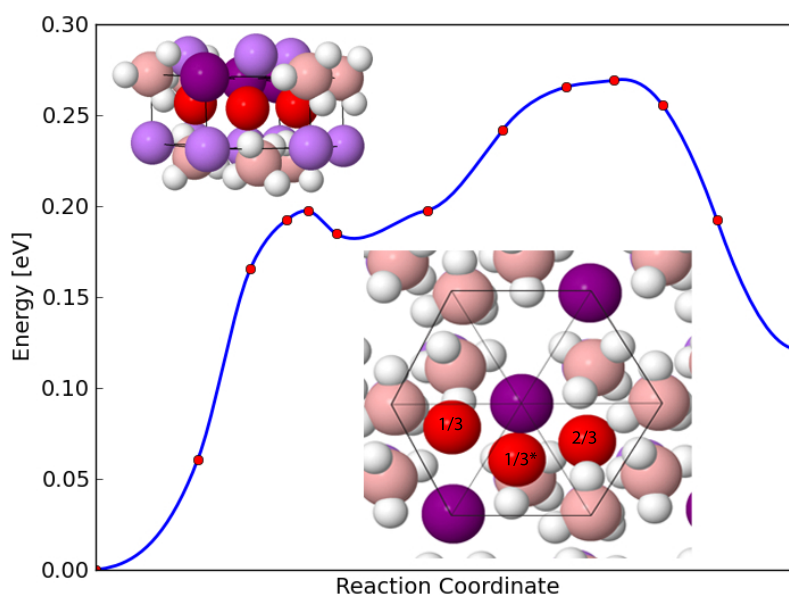


Figure 3.11: The minimum energy path for a Li_{int}^+ jump from a $1/3$ to a $2/3$ site, passing through a $1/3^*$ site. The atomic positions of the interstitial in the three different sites are shown from left to right in the same order as the sites occur along the path. The $1/3^*$ site opens up the possibility for interstitials with a lower kinetic energy. Non-defect atoms; Li: pale purple, I: dark purple, B: pink and H: white.

a high uncertainty, since the quality of the data is not as good as was hoped for, they show diffusion events with short jump lengths $\sim 2 \text{ \AA}$. The only mechanisms we see from the calculations with such short jump lengths are the mechanisms going through the $1/3^*$ site. The $1/3^*$ site has, however, a very low stability and therefore the reaction rate for leaving the site is much higher ($k_{1/3^*-1/3,300\text{K}}^{\text{HTST}} = 1.1 \times 10^{13} \text{ s}^{-1}$) than what is seen from the QENS.

The lower temperature mechanisms need therefore to be investigated further before definite conclusions can be made. We need better experimental data to get more accurate jump lengths and rates, and DFT calculations should be made to search for other short jump length mechanisms. There is also a possibility that the DFT calculations underestimate the stability of sites as the $1/3^*$, since the calculations are done at 0 K and there is no inclusion of entropy when the stability is evaluated.

Measurements under applied bias show a doubling in the Li^+ motion at 380 K and even though the data at 300 K could not be fitted they still show indications of increased motion in the system.

3.4 Screening for New Solid Electrolytes

Inspired by the work in section 3.2 and the previous success of computational screening for borohydride stability [7] we wanted to screen for possible new electrolyte materials.

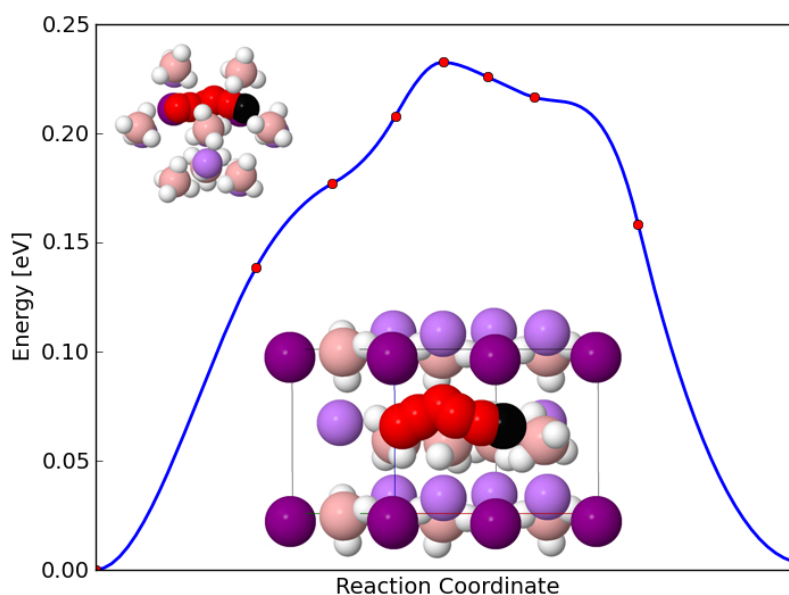


Figure 3.12: The minimum energy path for a V_{Li}^- hopping from a I^- to another I^- site. The inserted figures show the Li^+ that moves into the vacancy as a red atom, from the initial lattice site and few images along the path. The black atom shows the empty lithium site in the initial structure. Non-defect atoms are displayed as follows; Li: pale purple, I: dark purple, B: pink and H: white.

3.4.1 Computational Parameters

In this section the calculations were performed using VASP [80] and with largely the same parameters as in the $LiBH_4$ - LiI section. For all structures both the atomic configuration as well as the volume of the cell were relaxed.

3.4.2 Mixed Alkali Borohydrides

As has been presented in section 3.1.1, then the HT structure of $LiBH_4$ can be stabilized by anion substitution [58]. This sparked our interest in investigating whether it is also possible to stabilize the same high conducting structure by cation substitution.

In figure 3.13 the relative energy of the HT ($P6_3mc$) and the LT ($Pnma$) structures of $LiBH_4$ and the ground state structure of Na-, K- and $CsBH_4$ ($Fm-3m$) [85] are displayed. The relative energy is calculated relative to the most stable structure for each material and all energies are per formula unit ($M_{A0.5}M_{B0.5}BH_4$). The figure shows how the stability of the HT structure is increased relative to the LT structure and even the $Fm-3m$ structure as we move to larger alkali metals. This observation lead us to investigating the stability of alkali borohydride alloys. For all the alkali borohydrides calculations we used 6 different model structures. Beside the three structures previously presented, we used an octahedral structure with $Pnma$ symmetry that we will refer to as $oPnma$. This structure is observed for $NaBH_4$ at high pressures [85]. The fifth

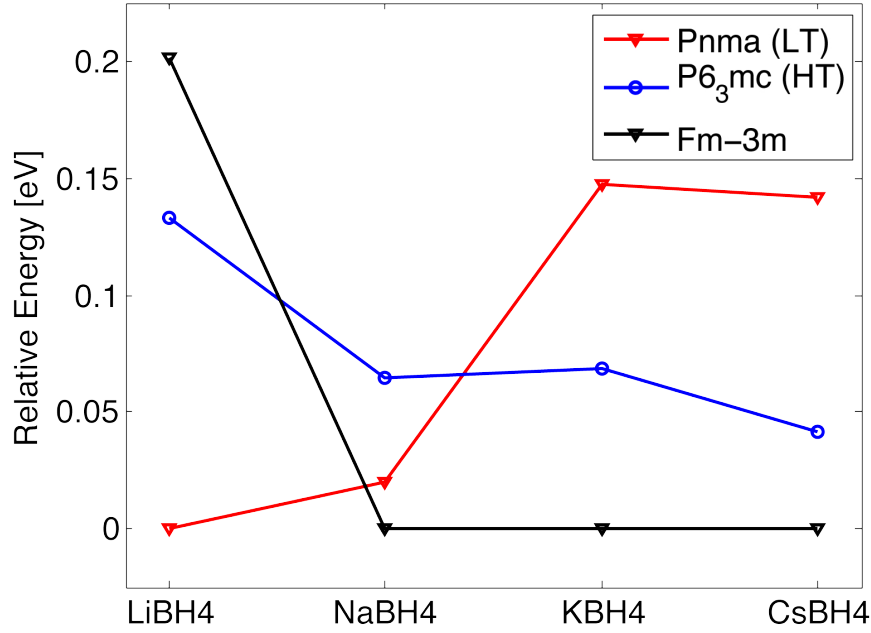


Figure 3.13: Shows the relative energy of LiBH₄'s LT (*Pnma*) and HT (*P6₃mc*) structures, as well as the ground state structure of Na, K and Cs borohydride (*Fm-3m*). The stability of LiBH₄'s HT structure is increased compared to the LT structure with increasing size of alkali metals. Furthermore the stability of the HT structure is increased compared to the ground state of each alkali borohydride with the size of the metal.

structure is a high pressure structure of LiBH₄ (*Ama₂*) [86] and the sixth is a simple model tetrahedral structure, that has been previously used in a screening study for borohydride [7].

In the following results we will focus on the first three structures unless one of the others shows an interesting behavior. This is done to make the presented figures more readable for the parameters we are interested in. Firstly we look at the alloy stability

$$\Delta E_{\text{alloy}}(\text{M}_{\text{A}0.5}\text{M}_{\text{B}0.5}\text{BH}_4) = E_{\text{M}_{\text{A}0.5}\text{M}_{\text{B}0.5}\text{BH}_4} - \frac{1}{2}(E_{\text{M}_{\text{A}}\text{BH}_4} + E_{\text{M}_{\text{B}}\text{BH}_4}) \quad (3.2)$$

and secondly how the relative stability of the HT structure changes with regard to the predicted ground state structure of the alloy. Neither of those are going to exactly predict the stability of either the alloy or the HT structure, but will be used as initial guides for what systems might be interesting to study further.

In figures 3.14-3.16 the relative energies for LiBH₄ and either Na-, K- or CsBH₄ are displayed, as well as the relative energies for an alloy of the two. The calculations indicate that the alloys of LiBH₄ and one of the larger alkali borohydride are not stable. The alloy stability of the LiNa(BH₄)₂ alloy is, though, close to being zero ($\Delta E_{\text{alloy}}(\text{Li}_{0.5}\text{Na}_{0.5}\text{BH}_4) = 0.02$ eV). The alloy stability decreases with the size of the larger alkali metal in the alloy, making it less likely that a stable alloy can be formed. The large gain in relative stability of the HT structure compared to the two ground state structures that we saw for the pure Na-, K-

and CsBH_4 does not seem to translate over to the alloys. For the $\text{Li}_{0.5}\text{K}_{0.5}(\text{BH}_4)$ and $\text{Li}_{0.5}\text{Cs}_{0.5}(\text{BH}_4)$ the stability of the HT structure is decreased compared to the LT structure but for $\text{Li}_{0.5}\text{Na}_{0.5}(\text{BH}_4)$ it stays approximately the same.

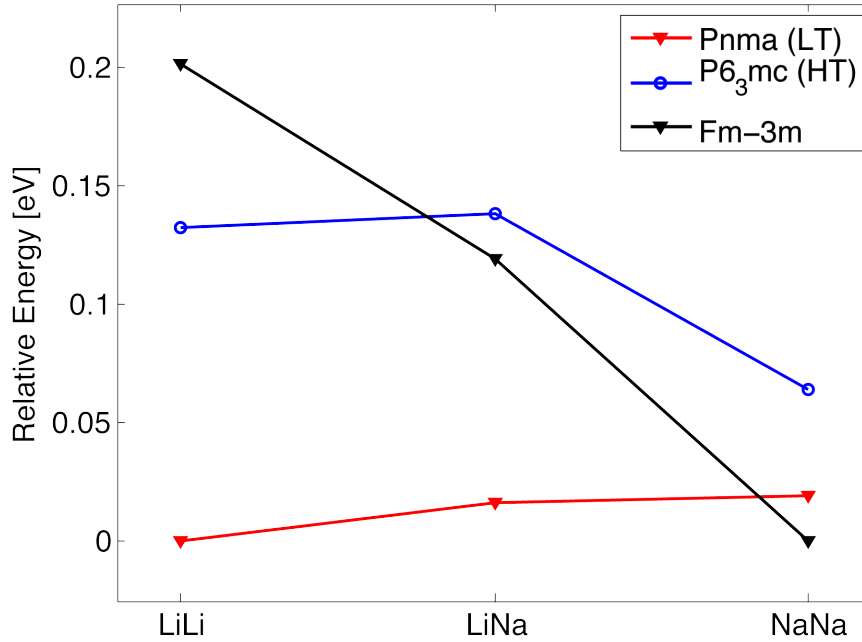


Figure 3.14: Shows the relative energy of LiBH_4 's LT (*Pnma*) and HT (*P6₃mc*) structures as well as the ground state structure of Na, K and Cs borohydride (*Fm-3m*) for LiBH_4 , NaBH_4 and an alloy of the two. The alloy stability for $\text{Li}_{0.5}\text{Na}_{0.5}\text{BH}_4$ is close to zero and the stability of the HT structure relative to the LT structure is similar for the $\text{Li}_{0.5}\text{Na}_{0.5}\text{BH}_4$ alloy as it for LiBH_4 .

In figure 3.17 a similar calculation is performed to see if a stable alloy of NaBH_4 and KBH_4 can be formed. The alloy stability of the $\text{Na}_{0.5}\text{K}_{0.5}\text{BH}_4$ is even worse than what we saw for the lithium alloys with $\Delta E_{\text{alloy}}(\text{Li}_{0.5}\text{Na}_{0.5}\text{BH}_4) = 0.08$ eV. Here the relative stability of the HT phase is increased substantially, but the increase in relative stability comes from the destabilization of the ground state structure and not the stabilization of the HT structure as can be seen from the figure.

The calculations do not give much hope that a stable alloy can be formed with a mixture of alkali borohydrides, or that such an alloy would stabilize the HT structure from LiBH_4 . The descriptors we use for the screening are, however, not exact and we should expect an uncertainty in the calculated numbers compared to the real stability. After performing the calculations we therefore wanted to try synthesizing a $\text{Li}_{0.5}\text{Na}_{0.5}\text{BH}_4$ alloy, since it was the one closest to being stable from the calculations and the relative stability of the HT is not destabilized from LiBH_4 .

In figure 3.18 results from impedance spectroscopy measurements on pure LiBH_4 , pure NaBH_4 and a 50/50 mixture of the two is displayed. Sample preparation and measurements were performed by Daði P. Sveinbjörnsson [87]. The 50/50 mixture sample was prepared by ball milling LiBH_4 and NaBH_4 together in even molar ratios for two hours. The figure shows the poor conductivity

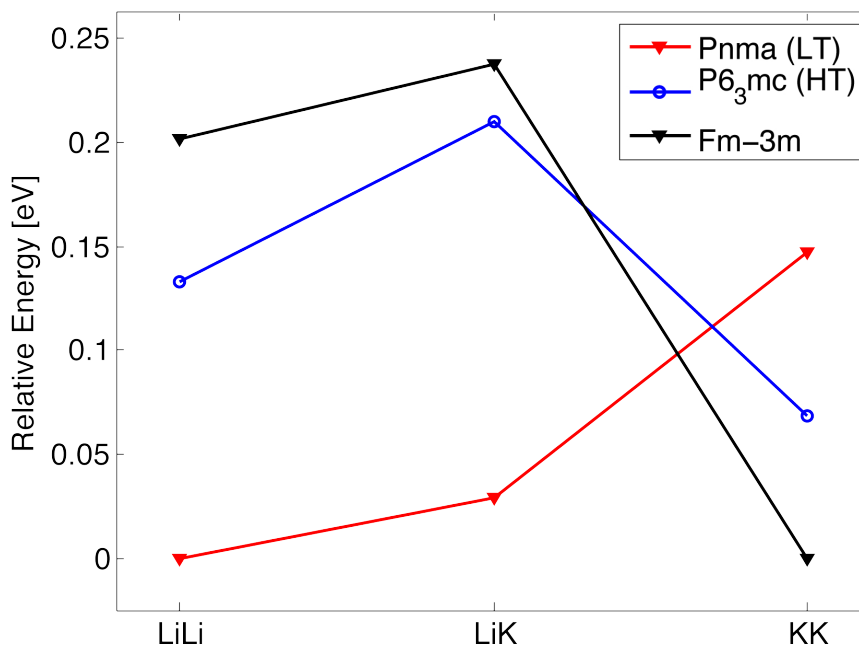


Figure 3.15: Shows the relative energy of LiBH_4 's LT ($Pnma$) and HT ($P6_3mc$) structures as well as the ground state structure of Na, K and Cs borohydride ($Fm-3m$) for LiBH_4 , KBH_4 and an alloy of the two. The alloy stability for $\text{Li}_{0.5}\text{K}_{0.5}\text{BH}_4$ is unfavorable by 0.3 eV and the stability of the HT structure relative to the LT structure is decreased by about 0.5 eV for the $\text{Li}_{0.5}\text{K}_{0.5}\text{BH}_4$ alloy compared to LiBH_4 .

for NaBH_4 and LiBH_4 before ball milling. After ball milling the conductivity is highly increased for both materials, an effect that is explained by the introduction of defects and smaller particle sizes after the milling, this is discussed further in Paper A. This effect is, however, not stable and disappears over time or after heat treatment. The 50/50 LiBH_4 and NaBH_4 sample shows similar conductivity as the ball milled LiBH_4 . Powder X-ray diffraction shows that the HT structure is not present at room temperature in the mixture and there is no evidence of a new structure. The results therefore do not indicate a formation of a $\text{Li}_{0.5}\text{Na}_{0.5}\text{BH}_4$ alloy and the high conductivity is most likely an effect from the ball milling on the LiBH_4 in the sample [87]. Unfortunately there is no further data to confirm the claim that the high conductivity will be reduced after heating. One further unanswered question is why there is not a clear phase transition to the HT phase for the mixed sample as is the case for pure LiBH_4 .

3.4.3 Transition Metal Substitution

Even though the stability of the HT structures is increased with the metal size for the pure alkali borohydrides, there is no stabilization gained by substituting Li with the larger alkali metals. In fact the opposite is true, that is, as the size of the alloying metal increases, the stability is decreased. This is true both for the alloy and for the relative stability of the HT structure towards the LT structure. The most straight forward explanation for this is that the large size difference between the Li atoms and the other alkali metals makes matching difficult and

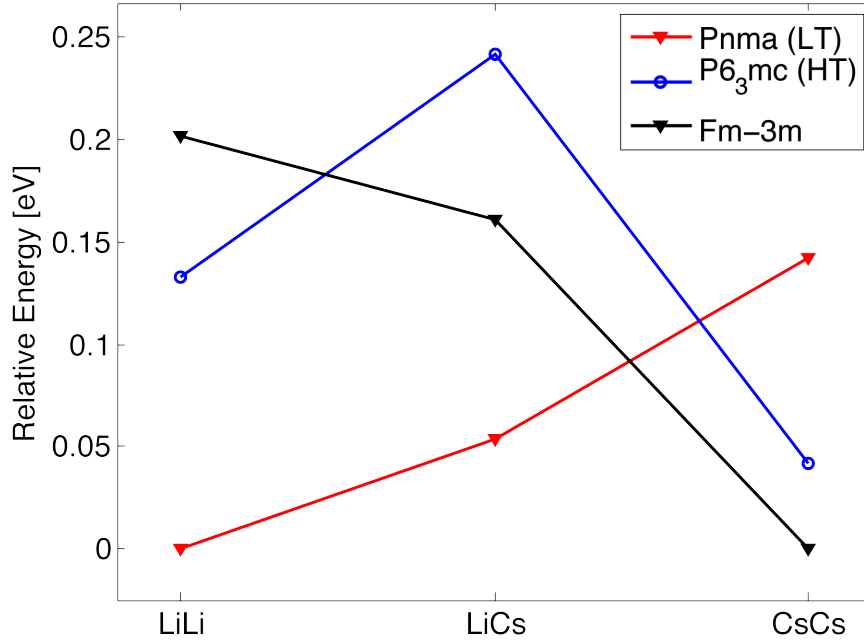


Figure 3.16: Shows the relative energy of LiBH_4 's LT ($Pnma$) and HT ($P6_3mc$) structures as well as the ground state structure of Na, K and Cs borohydride ($Fm-3m$) for LiBH_4 , CsBH_4 and an alloy of the two. The alloy stability for $\text{Li}_{0.5}\text{Cs}_{0.5}\text{BH}_4$ is unfavorable by 0.5 eV and the stability of the HT structure relative to the LT structure is decreased by about 0.6 eV for the $\text{Li}_{0.5}\text{Cs}_{0.5}\text{BH}_4$ alloy compared to LiBH_4 .

causes strain in the system.

Table 3.3: Atomic [88] and ionic [89] radii for alkali and transition metals used in the screening.

Element	Li	Na	K	Ni	Cu	Pd	Ag	Cs
Atomic radius [pm]	145	180	220	135	135	140	160	260
Ionic (+1) radius [pm]	90	116	152	-	91	73	123	181

Trying to bypass this, we decided to look at substitution of Li with few transition metals that have a more similar atomic (and ionic) size to lithium, than the large alkali metals. The transition metals we looked at are Ni, Cu, Pd and Ag. The atomic and ionic radii of the different alkali and transition metals discussed in this section can be seen in table 3.3. In figure 3.19 the relative energies of the examined structures are displayed for LiBH_4 and for alloys where half of the Li atoms have been substituted with the previously mentioned transition metals. For all the materials the LT structure is predicted as the ground state structure, except for $\text{Li}_{0.5}\text{Pd}_{0.5}\text{BH}_4$ where the $oPnma$ is predicted to be most favorable. The relative stability of the HT structure towards the predicted ground state structure of each system is almost a constant for LiBH_4 , $\text{Li}_{0.5}\text{Ni}_{0.5}\text{BH}_4$ and $\text{Li}_{0.5}\text{Cu}_{0.5}\text{BH}_4$. For $\text{Li}_{0.5}\text{Pd}_{0.5}\text{BH}_4$ the relative stability is decreased compared to the $oPnma$ structure, but at the same time this is the

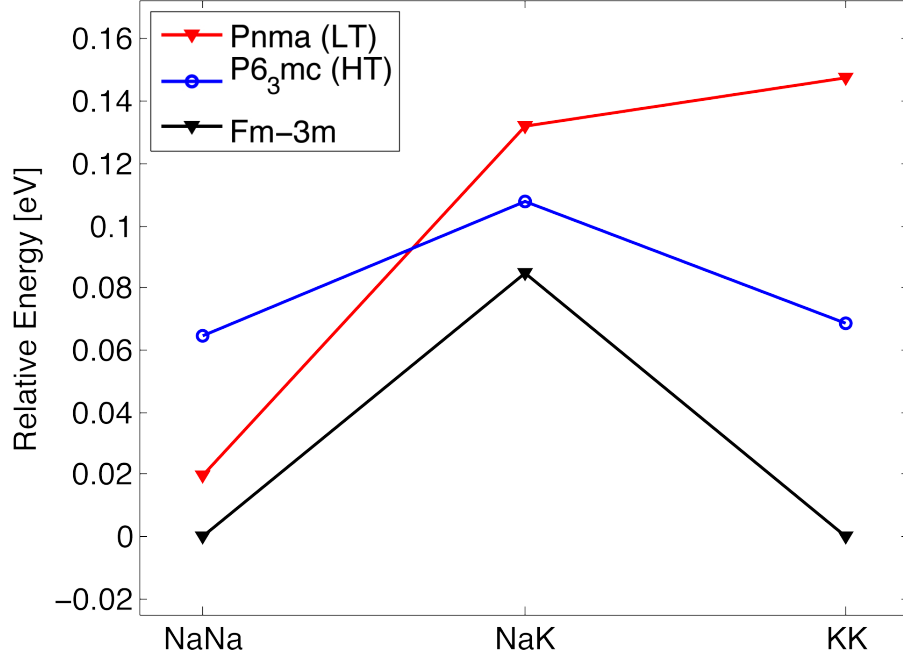


Figure 3.17: Shows the relative energy of LiBH_4 's LT ($Pnma$) and HT ($P6_3mc$) structures as well as the ground state structure of Na, K and Cs borohydride ($Fm-3m$) for NaBH_4 , KBH_4 and an alloy of the two. The alloy stability for $\text{Na}_{0.5}\text{K}_{0.5}\text{BH}_4$ is unfavorable by 0.8 eV, but the stability of the HT structure relative to the LT structure and the $Fm-3m$ structure is increased by about 0.7 eV and 0.4 eV respectively for the $\text{Na}_{0.5}\text{K}_{0.5}\text{BH}_4$ alloy compared to NaBH_4 .

only material where the HT structure is more stable than the LT structure. $\text{Li}_{0.5}\text{Ag}_{0.5}\text{BH}_4$ is the only composition that shows an increase in stability of the HT structure compared to the lowest energy structure. In figure 3.20 we try to estimate the stability of a possible $\text{Li}_{0.5}\text{Ag}_{0.5}\text{BH}_4$, by the same procedure as before. Similarly to the mixed alkali borohydrides, the $\text{Li}_{0.5}\text{Ag}_{0.5}\text{BH}_4$ alloy comes out unstable from the calculations compared to LiBH_4 and AgBH_4 . It should, however, be noted that AgBH_4 has not been synthesized, as far as we know. The fact that we don't know if AgBH_4 is stable as a compound makes it a weak reference point.

3.4.4 LiBH_4 - LiBF_4

Lithium tetrafluoroborate, LiBF_4 , has been used as a salt in liquid electrolytes, mainly because of its high thermal stability [90]. The ground state structure of LiBF_4 has been reported as a trigonal $P3_121$. In figure 3.21 we look at the possibility of substituting BF_4 into LiBH_4 . The figure shows that the HT structure is stabilized compared to the LT structure with the introduction of BF_4 in the material, however for this material, as for many others in this section, the alloy stability is unfavorable with $\Delta E_{\text{alloy}}(\text{Li}(\text{BH}_4)_{0.5}(\text{BF}_4)_{0.5}) = 0.06$ eV.

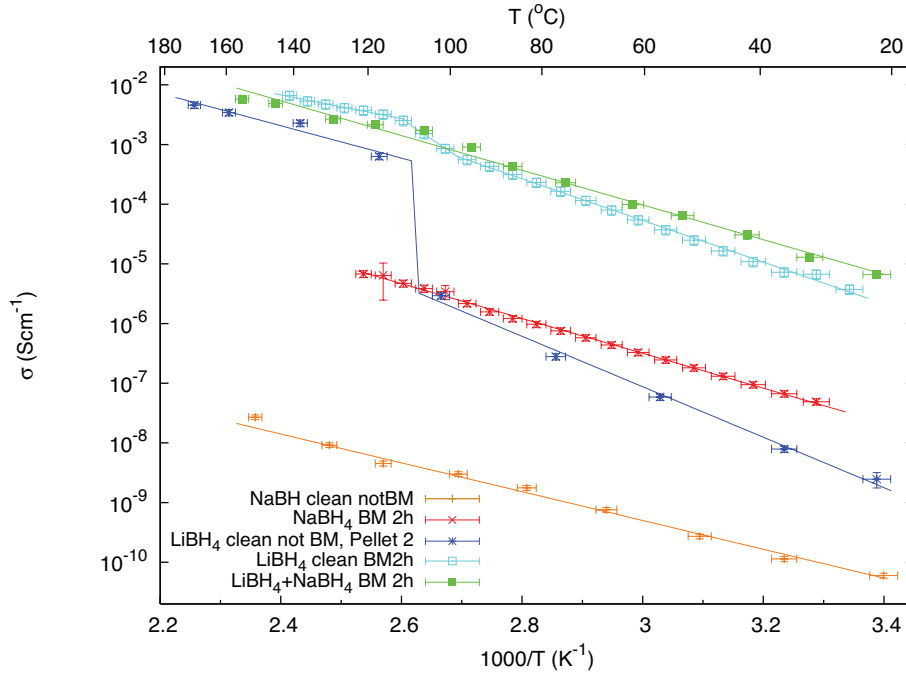


Figure 3.18: The Results of impedance measurements on pure LiBH_4 , pure NaBH_4 and a 50/50 mixture of the two. Measurements of the pure materials include both ball milled samples and non-ball milled samples. NaBH_4 has very poor conductivity compared to LiBH_4 . The ball milled LiBH_4 sample and the mixed one have very similar conductivities, suggesting that the same conducting species might be responsible in both cases. [87]

3.4.5 $\text{LiBH}_4\text{-LiI-LiNH}_2$

As was discussed in the introduction, new high conducting materials with different structures from the HT LiBH_4 structure have recently been reported [78, 79]. These materials can be viewed as a composition of LiBH_4 , LiI and LiNH_2 ; examples include $\text{Li}_2(\text{BH}_4)(\text{NH}_2)$, $\text{Li}_4(\text{BH}_4)(\text{NH}_2)_3$ and $\text{Li}_3(\text{NH}_2)_2\text{I}$. So far, the presented materials all only contain two of the three "base-materials", but it is an interesting question if new materials can be made from a combination of all three. Figure 3.22 shows a schematic ternary phase diagram that underlines the large number of possible compositions.

As a first step in investigating this ternary phase we did calculations starting from the known structure of $\text{Li}_3(\text{NH}_2)_2\text{I}$ (see figure 3.23). Step by step we substituted BH_4^- into the NH_2^- sites of the structure, making a path of $\text{Li}_3(\text{NH}_2)_{2(1-x)}(\text{BH}_4)_x\text{I}$ compositions, shown with a red line in the phase diagram. Figure 3.24 shows the alloy stability of the different compositions calculated. The alloy energy now is calculated from the three different base materials,

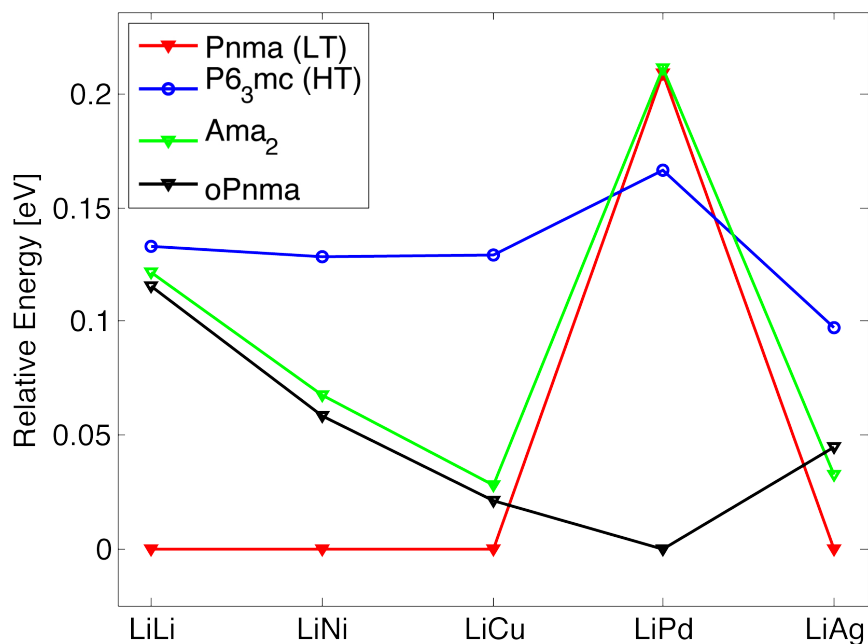


Figure 3.19: Shows the relative energy of LiBH₄'s LT (*Pnma*) and HT (*P6₃mc*) structures as well as the *Ama₂* and *oPnma* structures for LiBH₄ with and without transition metal substitution. The stability of the HT structure relative to the predicted ground state structure is not increased except for Li_{0.5}Ag_{0.5}BH₄.

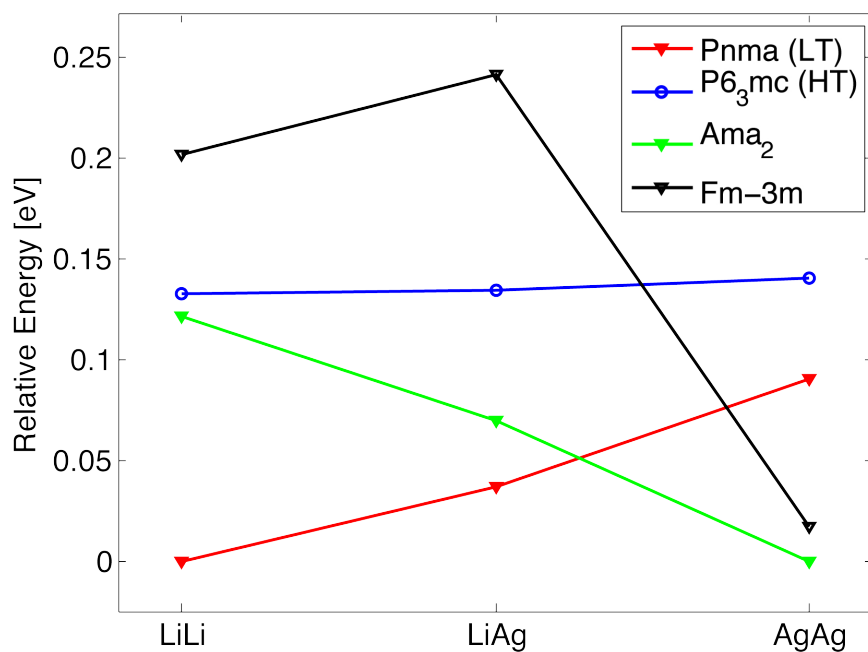


Figure 3.20: Shows the relative energy of LiBH₄'s LT (*Pnma*) and HT (*P6₃mc*) structures as well as the *Ama₂* and *Fm-3m* structures for LiBH₄, AgBH₄ and an alloy of the two. The alloy's stability is unfavorable by about 0.3 eV. For AgBH₄ we see the *Ama₂* structure predicted as the lowest energy structure for the first time.

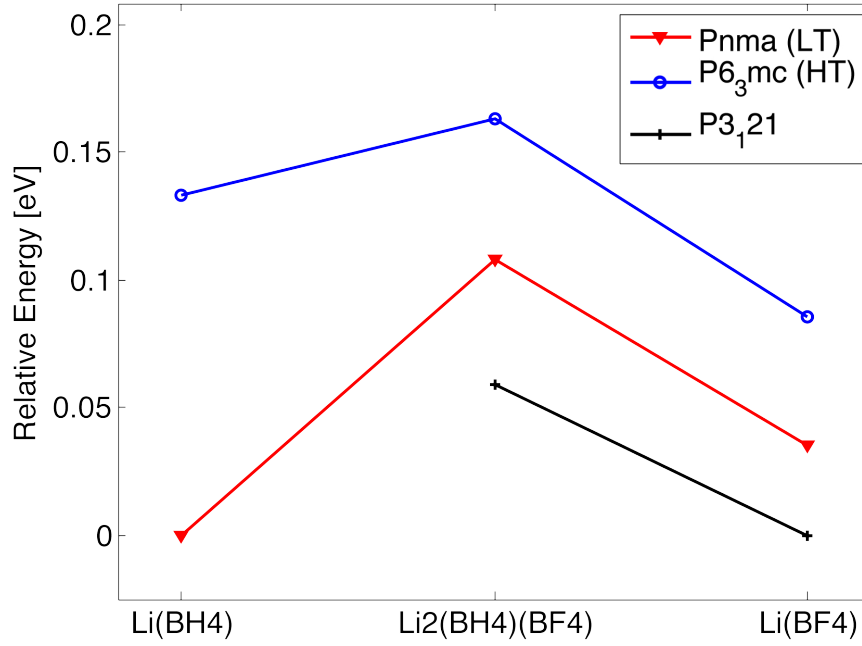


Figure 3.21: Shows the relative energy of LiBH₄'s LT (*Pnma*) and HT (*P6₃mc*) structures as well as the ground state energy structure for LiBF₄, *P3₁21*. The HT structure is stabilized relative to the LT structure with the increasing BF₄⁻ content in the material, but the alloy's stability is unfavorable by about 0.6 eV.

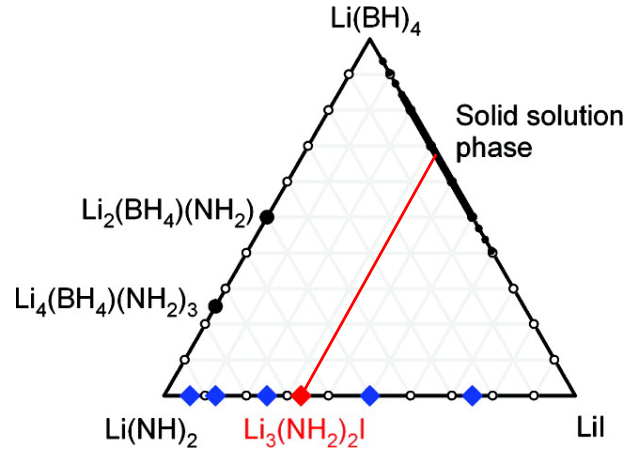


Figure 3.22: A schematic ternary phase diagram for the LiBH₄-LiI-LiNH₂ system. The diagram is originally from Matsuo et al. [79], but the red line representing the Li₃(NH₂)_(2-x)(BH₄)_xI system is added by the author.

$$\Delta E_{\text{alloy}}(\text{Li}_3(\text{NH}_2)_{(2-x)}(\text{BH}_4)_x\text{I}) = \frac{1}{3}(E_{\text{Li}_3(\text{NH}_2)_{(2-x)}(\text{BH}_4)_x\text{I}} - ((2-x)E_{\text{LiNH}_2} + xE_{\text{LiBH}_4} + E_{\text{LiI}})). \quad (3.3)$$

The first thing we note is that ΔE_{alloy} is not 0 for our starting point, Li₃(NH₂)₂I. This does not have to be surprising since, similarly as for the HT structure in

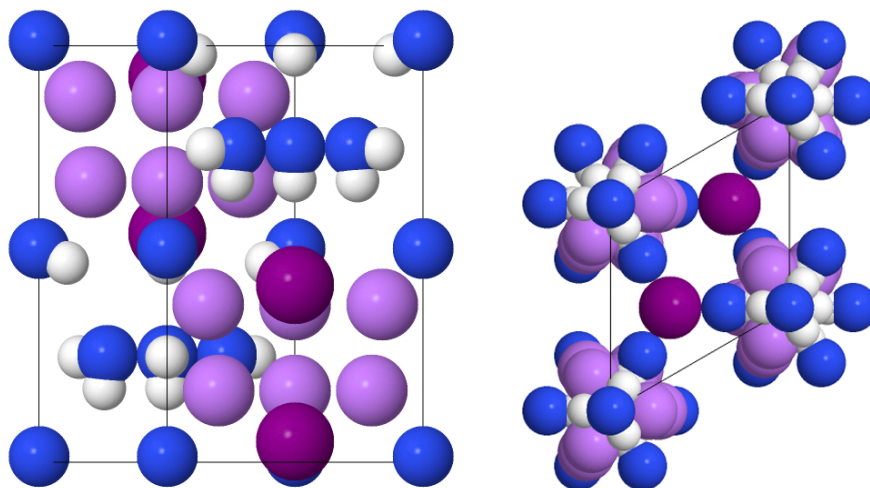


Figure 3.23: The crystal structure of $\text{Li}_3(\text{NH}_2)_2\text{I}$ as it is presented by Matsuo et al. [79]. Li: pale purple, I: dark purple, N: blue and H white.

LiBH_4 , the structure might become stable at finite temperature. Therefore, as before we look at how the stability changes with the substitution of BH_4 into the system.

Up to $x = 1.2$ we get values for ΔE_{alloy} that are similar to what we have for $\text{Li}_3(\text{NH}_2)_2\text{I}$, but at higher values of x the structure rapidly becomes less stable. As can be seen from figure 3.24, we present several values for $x = 1$, that is when we have even ratios of the different anions. The reason for this is that during the initial calculations there was a large change in the structure during relaxation for the $\text{Li}_3\text{NH}_2\text{BH}_4\text{I}$ composition. Trying to get a glimpse, into what kind of a structure the system was relaxing towards, we allowed the shape of the supercell to change during the structural relaxation. This gave a large increase in the alloy stability. As should be expected because of the complexity of the PES surface, the system relaxes to a low symmetry structure that is most probably only a local minimum. This is, however, an indication that a stable structure might be found for $\text{Li}_3\text{NH}_2\text{BH}_4\text{I}$, even though we get little information about what kind of structure that might be.

3.5 Solid Electrolytes Conclusions

In this chapter we have discussed the super ionic conducting HT phase of LiBH_4 and how it can be stabilized with halide substitution into the anion sites of the structure.

Comparison of DFT calculations with measured phase transition temperatures from DSC, shows that the ground state energy difference between the HT and LT phases can be used to predict the stabilization of the HT structure with increased concentration of I^- in the system.

Possible mechanisms for ionic conduction in the HT phase of the $\text{LiBH}_4\text{:LiI}$ solid solution were investigated. The calculations show that the high ionic conductivity is originated from frequently formed defects and their high mobility

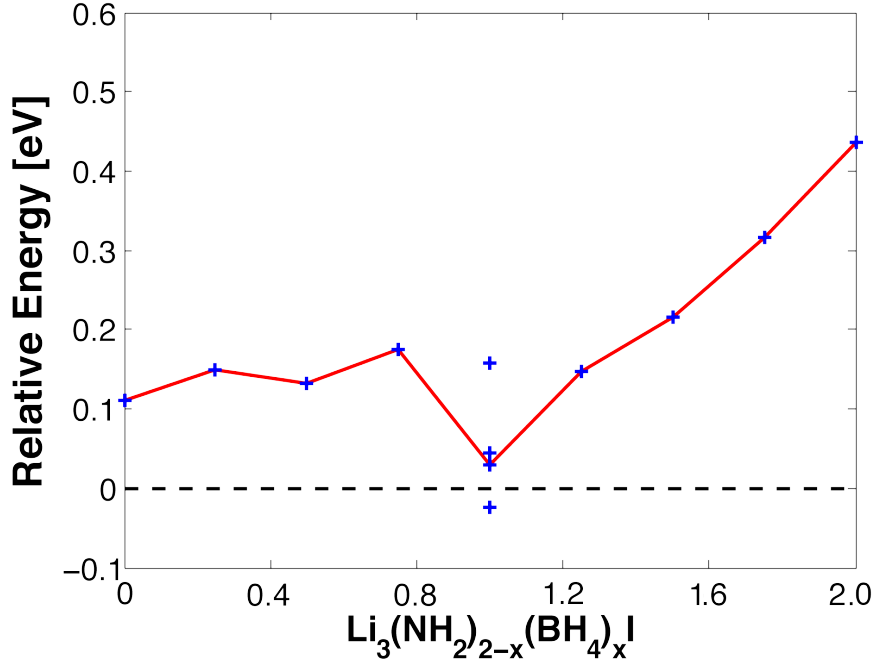


Figure 3.24: Shows the alloy stability of $\text{Li}_3(\text{NH}_2)_{2-x}(\text{BH}_4)_x\text{I}$ calculated from $\text{Li}_3(\text{NH}_2)_2\text{I}$'s high conducting structure. At $x = 1$, a large stabilization is observed by allowing the structure of the supercell to relax, indicating a possible stable composition.

in the structure. Good agreement is seen between DFT theory calculations and QENS measurements at 380 K, where both show jump events of one lattice unit length. At 300 K the QENS results indicate shorter jump lengths ($\sim 2 \text{ \AA}$) and a possible short jump length mechanism is presented from the DFT calculations, through a $1/3^*$ site. The stability of the $1/3^*$ site is, however, very low in the calculations and further investigations have to be done to confirm and explain the QENS results at 300 K.

A screening study for new solid electrolytes was presented. In the study the relative stability of LiBH_4 's HT structure and/or the alloy stability, were used to investigate possible room temperature superionic conductors. Most of the studied materials were shown unstable in the calculations, however, indications of a stable composition was observed in $\text{Li}_3(\text{BH}_4)(\text{NH}_2)\text{I}$ and further measurements have to be done to rule out high conductivity in a $\text{LiBH}_4\text{:NaBH}_4$ powder mixture.

4.1 Introduction

The Li-ion battery is the most widespread battery technology in modern mobile electronic devices [1, 2]. From its introduction in 1991 [91, 92, 93] it has cleared the way for the wave of handheld music players, mobile phones, laptop computers and a number of other applications. The demand for increased energy density is, however, constantly growing and even though there is still room for improvements for the Li-ion technology, there are fundamental limitations to how high energy densities can be reached in the frame of the Li-ion technology. When it comes to more energy consuming applications like electric vehicles (EV), where the competition comes from highly energy dense fossil or synthetic fuels, the demand for higher energy densities becomes even more prominent.

This demand for has sparked great research interest in metal-air batteries in recent years. Of all the metal-air batteries, Li-air is the one with the highest theoretical energy density. If a commercial Li-air battery can be developed it is predicted that it could have up to an order of magnitude higher energy density than modern Li-ion batteries [1]. A Li-O₂ battery with an aprotic solvent was first shown to be rechargeable in 1996 by Abraham et al., where Li₂O₂ was formed at the cathode during discharge [94]. The massive interest in Li-air as a future high energy density battery technology has resulted in a plethora of publications and significant new insight into the fundamental mechanisms and challenges of aprotic Li-O₂ batteries has been gained in recent time.

4.1.1 The Li-O₂ Battery

There are at least four different Li-air architectures being investigated [3]. That is aprotic [94, 1], aqueous, mixed architecture with aqueous and aprotic electrolytes immersing the cathode and anode respectively and finally an all solid state battery [3]. However, typically when people talk about Li-air batteries they are referring to an aprotic Li-O₂ battery (O₂ since the battery is fed pure oxygen at the cathode, but not air). The battery is then composed of a lithium metal anode, an electrolyte made out of an aprotic solution of a lithium salt

and a porous cathode made out of a light material, e.g. porous carbon [3]. The cathode material should have a large surface area to increase reactivity and it should act as an electronic conductor to the nucleation sites in the cathode as well. During discharge, Li^+ ions flow from the anode through the electrolyte and to the cathode where they react with oxygen, forming predominantly Li_2O_2 [1].

4.1.2 Challenges to Overcome

Although Li-air is a promising technology there are number of fundamental challenges that need to be overcome if it is supposed to become a practical application. These include:

- Large difference in discharge and charge potentials, causing low energy efficiency in the battery.
- Limited Li_2O_2 growth at the cathode, which again limits the energy density of the battery.
- Low power densities.

In this chapter we will investigate and discuss the origin of the high overpotentials and the limited growth and possible solutions.

4.1.3 Chapter Outline

The outline of the work presented on Li-air is as follows:

- **Reaction Mechanisms on Li_2O_2 Surfaces.** Presents a screening study on discharge and charge mechanisms at stepped reconstructed Li_2O_2 ($1\bar{1}00$) surface. The difference between 4 and 6 step mechanisms is investigated and discussed.
- **O_2 Reaction Barriers.** Presents a study on possible free energy barriers for O_2 desorption from a Li_2O_2 ($1\bar{1}00$) surface.
- **The Role of Li Vacancies in Li_2O_2 Electronic Transport.** Discusses the role of V_{Li} on electronic conduction in Li_2O_2 and presents calculations on the mobility of the bulk vacancies.
- **Selective Sulfur Poisoning.** Summarizes a study presented in Paper D on the binding of S and SO_2 on reactive ($1\bar{1}00$) and (0001) Li_2O_2 surface sites. The possibility of controlling Li_2O_2 growth with selective poisoning is discussed.

4.2 Reaction Mechanisms on Li_2O_2 Surfaces

To understand the different problems facing the Li-air technology it is a key thing to understand the mechanisms governing growth and decomposition of Li_2O_2 .

Initial research on Li-air cells showed large asymmetry in the overpotential between discharge and charge (e.g. figure 4.1) [1, 94, 3]. The large difference in the discharge and charge potentials cause the round trip efficiency to be low, about 60-70%. Some success in lowering the asymmetry was achieved with the use of MnO_2 [1], Au [95] and Pt [96] catalysts.

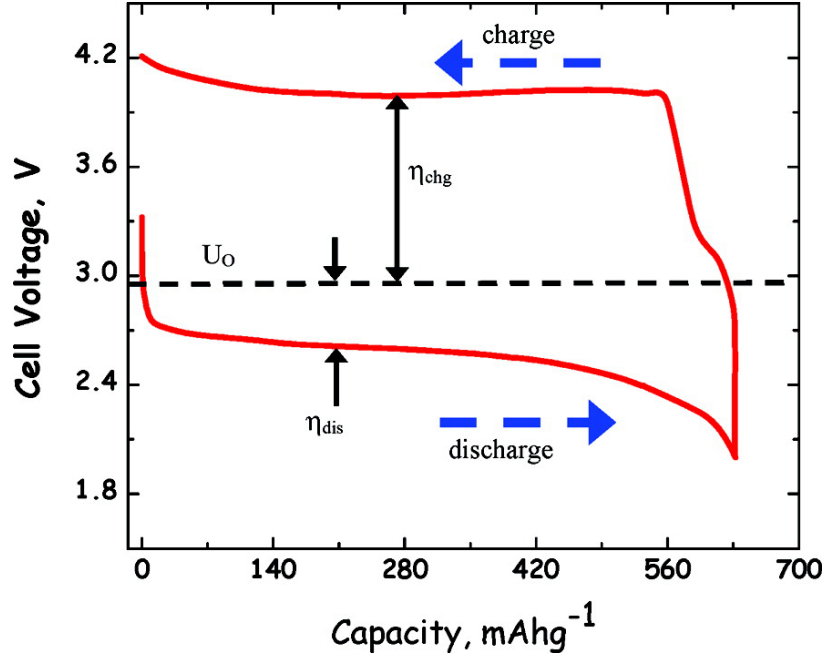


Figure 4.1: Discharge-charge cycle for an aprotic Li-O_2 cell. The cycle shows a large asymmetry between the overpotential for discharge and charge. The large difference between discharge and charge potentials leads to low round trip efficiency ($2.6 \text{ V} / 4 \text{ V} = 65\%$) [3].

The growth of Li_2O_2 at a step on a reconstructed $(1\bar{1}00)$ Li_2O_2 surface (see figure 4.2) has been studied by Hummelshøj et al. [97]. The reconstructed $(1\bar{1}00)$ surface was picked since it was found to be most stable from a range of different surfaces they investigated. The growth is considered at a step since under-coordinated sites generally act as nucleation sites for crystal growth. From their study Hummelshøj et al. proposed a 4 electron discharge mechanism, in which two LiO_2^* species form before reacting twice with $(\text{Li}^+ + \text{e}^-)$ to form $2\text{Li}_2\text{O}_2$. By assuming that the reversed mechanism applies for charging, the model showed an asymmetry in the overpotentials for discharge and charge, with $\eta_{\text{dis}} = 0.43 \text{ V}$ and $\eta_{\text{chg}} = 0.60 \text{ V}$.

Peng et al. have studied reaction species on a Li-air cathode using Raman spectroscopy [98], reporting a fundamentally different reaction mechanism for charge and discharge, i.e. formation of intermediate LiO_2^* on discharge and a one step dissociation of Li_2O_2 to $2(\text{Li}^+ + \text{e}^-)$ and O_2 on charge.

In this section we will present a screening study on the same model system as Hummelshøj et al. used in their study, to search for mechanisms that will open up at lower overpotentials than the one they presented. We will also discuss the possibility of 6 step mechanisms, where the O_2 reacts in a non electrochemical way and how they affect discharge and charge.

4.2.1 Computational Parameters

All calculations presented here are performed using GPAW [20, 21] and ASE [81]. The RPBE functional is used to approximate the electronic exchange and correlation [17]. For the atomic structural energy minimization the calculation is continued until all forces are below 0.03 eV/Å. Our supercells consist of a 56-64 atoms slab (see figure 4.2) with an approximately 18 Å long vacuum layer. The supercell is sampled with a (4,4,1) Monkhorst-pack k-point mesh and the distance between grid points is 0.15 Å.

Since it is well known that DFT does not describe the triplet ground state of O₂ accurately, we use a water reference for the ground state energy of O₂,

$$E(\text{O}_2) = 2E_{\text{DFT}}(\text{H}_2\text{O}) - 2E_{\text{DFT}}(\text{H}_2) - 2\Delta E_{\text{exp}}(\text{H}_2\text{O}). \quad (4.1)$$

Here $E_{\text{DFT}}(\text{H}_2\text{O})$ and $E_{\text{DFT}}(\text{H}_2)$ are the calculated energy values for H₂O and H₂ respectively, but they are better described with DFT than O₂. $\Delta E_{\text{exp}}(\text{H}_2\text{O})$ is the experimental formation energy for H₂O corrected for zero-point energies [37]. Although this might seem like an odd way to attack the problem, this method has previously been shown to give good results [37].

The entropy for the solid phases, Li₂O₂ and Li metal, is negligible and is not considered when free energy changes are estimated. The entropy of O₂ in gas phase is however considerable ($-T\Delta S(\text{O}_2) = -0.63$ eV at STP) and is used when the free energy of O₂ is calculated.

We define the potential to be zero, $U = 0$, when the free energy difference between (Li⁺ + e⁻) and bulk Li is zero. The free energy of electrons at the cathode will then be shifted by an applied potential, by $-neU$ as is described in section 2.4.1.

4.2.2 Screening Setup

The screening is constrained to only the first row of atoms at the step (see figure 4.2). This is done so that when a full cycle has been removed or added (2 f.u.) we are left with a system that is fundamentally the same as the one we started from. By this we prevent that energy differences from changing the surface from the initial to the final state are playing a role in the overall reaction mechanisms. At the first row we have 8 atoms that make up 6 reaction species since the O₂ molecules are never dissociated when they react with the surface. We label the Li at the step (from the left to the right in figure 4.2) as lithium in valley Li_{valley}, lithium in middle to the left Li_{m.left}, lithium on ridge Li_{ridge} and lithium in middle to the right Li_{m.right}. The oxygen molecules are also labeled from the left to the right as oxygen in valley O_{2valley} and oxygen on ridge O_{2ridge}. As previously mentioned, we looked at two different types of reaction mechanisms, 4 step mechanisms, in which there are only electrochemical steps and 6 step mechanisms, in which there are 4 electrochemical steps and 2 thermodynamic steps. For the 4 step mechanisms each step consists of a reaction of a Li⁺ or a LiO₂⁺ ion with the Li₂O₂ surface that supplies electrons. For the 6 step mechanisms each step consists either of a Li⁺ ion or an O₂ molecule reaction with the Li₂O₂ surface. At each reaction step there is a choice of reaction from several different sites, leaving us with hundreds of different possible

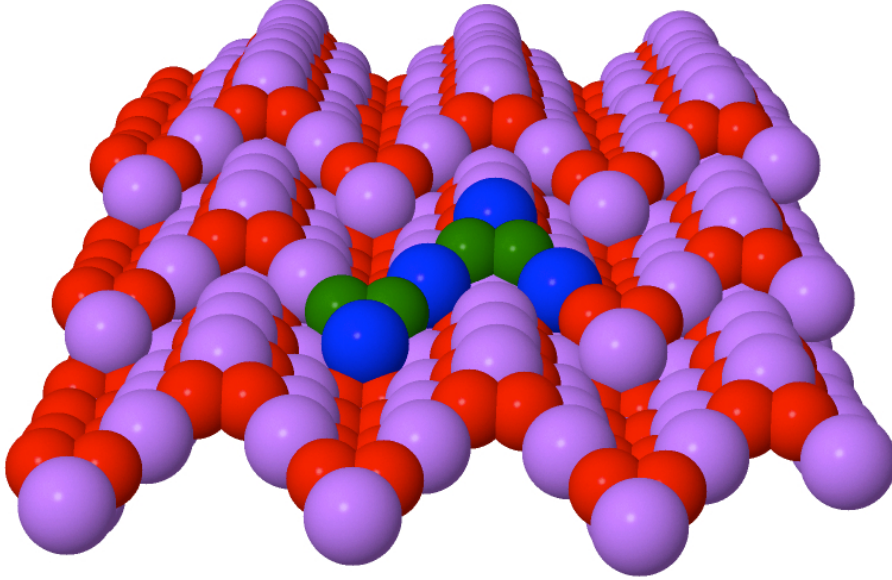


Figure 4.2: $3 \times 3 \times 1$ repetition of the calculation supercell of a Li_2O_2 stepped $(1\bar{1}00)$ surface. The blue and green atoms show Li and O atoms respectively that make up the first row at the step in a single supercell. The Li atoms are labeled from the left to the right as: Li in valley $\text{Li}_{\text{valley}}$, Li in middle to the left $\text{Li}_{\text{m.left}}$, Li on ridge Li_{ridge} and Li in middle to the right $\text{Li}_{\text{m.right}}$. The O_2 molecules are also labeled from the left to the right as O_2 in valley $\text{O}_{2\text{valley}}$ and O_2 on ridge $\text{O}_{2\text{ridge}}$.

mechanisms. The different reaction steps are much fewer, or 64, because they reoccur between different mechanisms. We are therefore able to investigate all possible mechanisms for the reactions by doing calculation on the 64 different steps.

4.2.3 4 Step Mechanisms

From the calculation we get a heat of formation for Li_2O_2 of $\Delta H = -6.09$ eV and free energy of formation of $\Delta G = -5.46$ eV, which is slightly lower than the experimental values $\Delta H_{\text{exp}} = -6.56$ eV and $\Delta G_{\text{exp}} = -5.91$ eV [99]. This gives us an equilibrium potential $U_0 = -\Delta G/2e = 2.73$ V compared to the experimental value $U_{0,\text{exp}} = 2.96$ V.

For discharge it is the lowest free energy step, $\Delta G_{i,\text{min}}$, along the reaction mechanism that will first become uphill with applied potential and therefore it defines the discharge potential and the overpotential during discharge, $U_{\text{discharge}} = \min[-\Delta G_i/e]$ and $\eta_{\text{discharge}} = U_0 - U_{\text{discharge}}$. In the same way it is the largest free energy step that will open up at the highest potential in the reverse direction for charge, giving $U_{\text{charge}} = \max[-\Delta G_i/e]$ and $\eta_{\text{charge}} = U_0 - U_{\text{charge}}$.

In figure 4.3 three different mechanisms are presented, that we will refer to as the low current mechanism and the high current mechanism for discharge and charge respectively. The low current mechanism is the mechanism that opens up at the lowest overpotential out of all the calculated mechanisms, both for discharge and charge. In the low current mechanism during discharge the 4

reaction steps are i) formation of LiO_2^* with the lithium and the oxygen sitting in the respective valley sites, ii) formation of a second LiO_2^* with the lithium sitting at a middle site and the oxygen at the ridge site, iii) the second lithium middle site is occupied and iv) the lithium ridge site is occupied. For charge the same reaction steps apply but in the reverse order.

The discharge is downhill up to an effective potential of $U_{\text{discharge}} = 2.66$ V giving an overpotential of only $\eta_{\text{discharge}} = 0.07$ V. The mechanism opens up for charge already at $U_{\text{charge}} = 2.81$ V giving almost no asymmetry in the overpotential since $\eta_{\text{charge}} = 0.08$ V. According to this, both discharge and charge can open up at low overpotentials, but with only one out of all possible reaction mechanisms open the current is going to be low. To increase the current the system needs to move to higher overpotentials, opening up different reaction mechanisms one after another.

When the reaction species come towards the surface they have different probabilities of binding to different surface sites, depending on the stability of the sites. The high current mechanisms are chosen in such a way that for each step the most favorable reaction is chosen (most probable reaction). There are number of other mechanisms that the system is similarly likely to go through, but the presented mechanisms give a good image of how the overpotential is likely to change with increased current. Coincidentally, the reaction species react in the same order for the two high current mechanisms as for the low current mechanism. For the discharge high current mechanism the effective potential has been lowered to $U_{\text{discharge}} = 2.27$ V, increasing the overpotential to $\eta_{\text{discharge}} = 0.46$ V. For the high current charge mechanism the potential has changed even more from the low current mechanism with the effective potential at $U_{\text{charge}} = 3.48$ V and a $\eta_{\text{charge}} = 0.75$ V overpotential.

The overpotential is raised from the low to the high current mechanisms, especially for charging, but this is quite intuitive. The easiest first steps during charging is the removal of Li^+ sitting in the most unstable sites, when they are gone the system is left with the expensive removal of LiO_2^* for step 3 and 4 that leads to a raised overpotential.

4.2.4 6 Step Mechanisms

Continuing from the last section, let us consider the case where two Li^+ have been removed from the model structure during charging. We are now left with two LiO_2^* that are both expensive to remove in a single step. In this section we will consider what happens if, instead of removing LiO_2^* in the following steps, the mechanism would continue with a removal of Li^+ . In figure 4.6 a free energy diagram of a six step mechanism for charging is displayed. The O_2 steps are not electrochemical and do therefore not change with applied potential. By removing the O_2 from the electrochemical process the equilibrium potential is lowered from $U_0 = 2.73$ V to $U_{0,\text{Li-only}} = 2.58$ V. This means that even though the overpotential for charging in the displayed 6 step mechanism is higher than for the low current 4 step mechanism, $\eta_{6\text{st,charge}} = 0.30$ V, then the lowering of the equilibrium potential causes the effective potential for charging to be similar to that of the low current 4 step mechanism and significantly lower than for the high current mechanism, $U_{\text{charge}} = 2.88$ V. Since all the electrochemical reaction

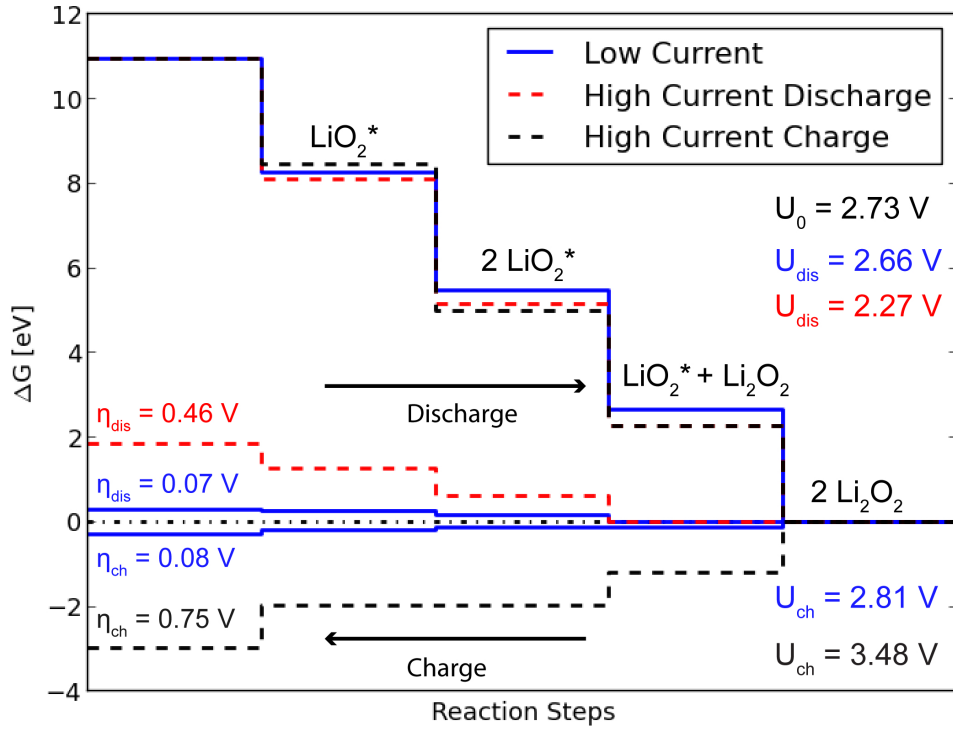


Figure 4.3: Free energy diagram for discharge and charge at a stepped Li_2O_2 ($1\bar{1}00$) surface. Our calculations show that both charge and discharge can open up at low overpotentials < 0.10 eV. For increased current more reaction mechanisms can open up at higher overpotentials.

species are the same in the 6 step mechanism then there are also much smaller variations in the overpotential between different mechanisms. This means that a large number of mechanisms can be opened up, without raising the overpotential much.

When all four Li^+ ions have been removed we are left with a destabilized O_2^* surface species. The destabilization from removing the Li^+ is significant enough that the binding energy of the two O_2^* species is only $\Delta E_{\text{binding}}(\text{O}_2) = 0.37$ and 0.26 eV. The weak binding shows that O_2^* species will be released frequently from the surface at room temperature during charging.

While the 6 step mechanisms are favorable for charging, they are not so favorable for discharge since the lowering of the equilibrium potential will decrease the effective potential from the 4 step mechanisms, which would mean less energy output from the reaction.

4.2.5 Recent Findings

Publications by by Radin et al. [100, 101], Lau et al. [102] and Mo et al. [103] have shown that a number of other facets have similar surface energies and will likely be exposed, including (0001), ($1\bar{1}00$) and ($11\bar{2}0$). Recent work by Hummelshøj et al. [104] has shown that these terminations will depend on potential and can be different under charge and discharge conditions. They

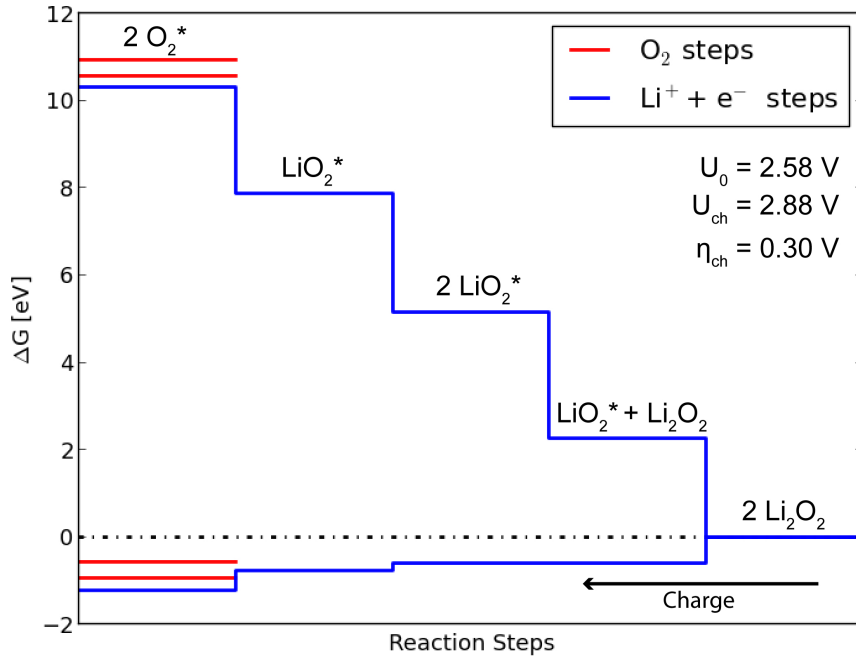


Figure 4.4: A free energy diagram for discharge and charge at a stepped Li_2O_2 $1\bar{1}00$ surface. Our calculations show that both charge and discharge can open up at overpotentials as low as 0.25 eV. For increased current more reaction mechanisms can open up at higher overpotentials.

also show that low overpotential reaction mechanisms are available on kinks and steps on $(1\bar{1}00)$ and (0001) surfaces and these sites will control the growth of Li_2O_2 at lower current densities.

Recent reports from McCloskey et al. suggest that the high overpotential during charging is originated from lithium carbonate species that form when the electrolyte reacts at the cathode during discharge [105]. Furthermore, Xu et al. [106] show that by using a dimethyl sulfoxide (DMSO) based electrolyte it is possible to lower the charging potential, in agreement with our findings.

4.3 O_2 Reaction Barriers

In the previous discussions we have assumed that reaction barriers are negligible. This approximation has been successfully applied in a number of previous studies on electrochemical processes [37, 38, 39, 40]. In this section we will investigate if this assumption holds for the thermodynamical desorption of O_2 from the Li_2O_2 surface. This will be done by calculating the minimum free energy mechanism for O_2 leaving the surface and traveling up into the vacuum layer. The free energy is then estimated along the minimum energy mechanism to estimate the transition barrier for O_2 desorption.

As mentioned previously, then the free energy for gas phase O_2 is calculated

by adding the entropy contribution $-T\Delta S = -0.63$ eV (at $T = 298$ K) to the calculated energy. The main components of the entropy are the translational and rotational parts, $-T\Delta S_{\text{translation}} = -0.47$ eV and $-T\Delta S_{\text{rotation}} = -0.14$ eV. Along the minimum free energy mechanism the O₂ molecule gains rotational and translational freedom as the interaction with the surface fades. It is not obvious how this affects the entropy of the molecule or the change in free energy along the mechanism.

To get a better understanding of the translational and rotational freedom of an O₂ molecule close to the Li₂O₂ surface we did a series of single point calculations, where the molecule is rotated at, or shifted from a placement of 1.6 Å elevation above the ridge step site. The results are displayed in figure 4.5. In the first frame the energy profile for a rotation of O₂ in the surface plane is displayed. The rotation is somewhat hindered in this direction with small rotational barriers of about ~ 70 meV. In the second the frame energy profile for rotation perpendicular to the plane is displayed. In this direction the molecule rotates freely as the rotational barriers of 1 – 2 meV are much smaller than the thermal energy at room temperature. In the third frame the energy profile for a translation of the molecule parallel to the surface ridge is displayed. In the figure, the positive direction is displacement away from the surface step. As is expected, the O₂ is still affected by the attractive force from the surface and a molecule that does not have enough kinetic energy away from the surface would adsorb back to it. In the fourth frame the energy profile for translation perpendicular to the surface ridge is displayed. The energy profile forms a minimum at 0 displacement, since the O₂ is positioned above the surface ridge and when it is displaced in either direction the distance to the surface is increased. The energy does, however, not rise very high the for calculated range of displacements and the O₂ is likely to start moving around in the surface plane, even though the movement is somewhat damped.

In figure 4.6 we display a minimum free energy path for O₂ desorption. The entropy of the O₂ molecule along the path is assumed to increase in inverse proportion to the interaction with the surface. The free energy for image i along the mechanism is calculated as

$$\Delta G_i = \Delta E_i - T\Delta S \frac{\Delta E_i}{\Delta E_{\text{final}}}. \quad (4.2)$$

where ΔE_i is the energy difference between the state of image i and the initial state and ΔE_{final} is the energy difference between the final and initial states. The presented path is for O₂ sitting in a ridge site after three Li⁺ have been removed (Li_{m.left}, Li_{m.right} and Li_{ridge}). The reason we pick this particular desorption mechanism is that this is the lowest energy desorption of all possible O₂ desorption mechanisms in our model system. The low binding energy of the O₂ makes it more likely that reaction barriers are visible along the path and not buried in the free energy difference between the initial and final state. We have performed the same calculation from a number of different sites and for O₂ molecules that have not been destabilized before the desorption, and the result is always the same. As can be seen from the minimum free energy path, there is no visible transition barrier along the path, supporting our previous approximation of not considering thermal barriers in the reaction mechanisms. However,

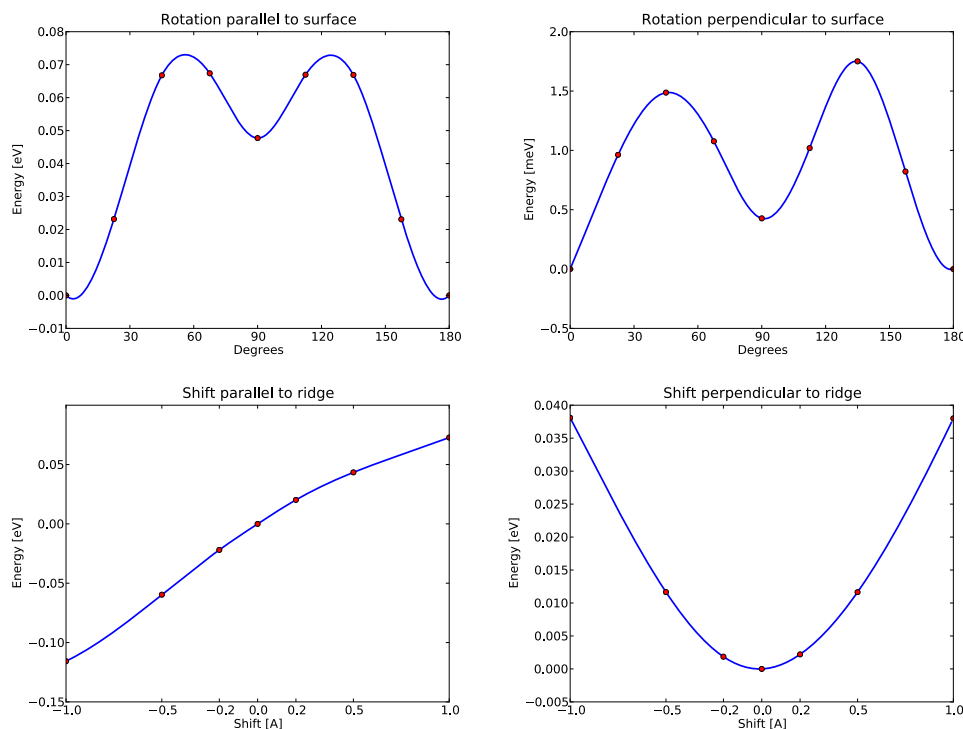


Figure 4.5: Translational and rotational freedom of O_2 at 1.6 Å elevation above its ridge site on the Li_2O_2 surface. Upper left: half circle rotation of O_2 in the plane parallel to the surface. Upper right: half circle rotation of O_2 in the plane perpendicular to the surface. Lower left: shift of O_2 parallel to the surface ridge, with the positive direction away from the ridge. Lower right: shift of O_2 perpendicular to the surface ridge.

we need to be aware that the evaluation of the free energy is speculative and we can not exclude some kind of a transition barrier for the real free energy minimum path. We are confident that if such a transition barrier exists then it will be small in comparison to the surface binding energy of the O_2 . The path seems to converge to a gas phase limit rather fast; already at the third point (2.5 Å above the surface) the free energy is close to the free energy of the final state (9 Å above the surface).

4.4 The role of Li Vacancies in Li_2O_2 Electronic Transport

In Paper C the electronic conduction of Li_2O_2 is studied. For the paper I did calculations on V_{Li} diffusion in bulk Li_2O_2 , those results will be summarized in this section and discussed.

A significant limitation for high capacity and power density batteries is the insulating nature of the Li_2O_2 deposits. With a band gap of 4.9 eV obtained from G_0W_0 calculations [97], the Li_2O_2 will ultimately limit the electronic conduction from the electrode to the active site [107, 108, 109]. It has been documented that electronic conduction through Li_2O_2 becomes limiting for the electrochemical discharge already after a 5 nm film is deposited (depending on the current

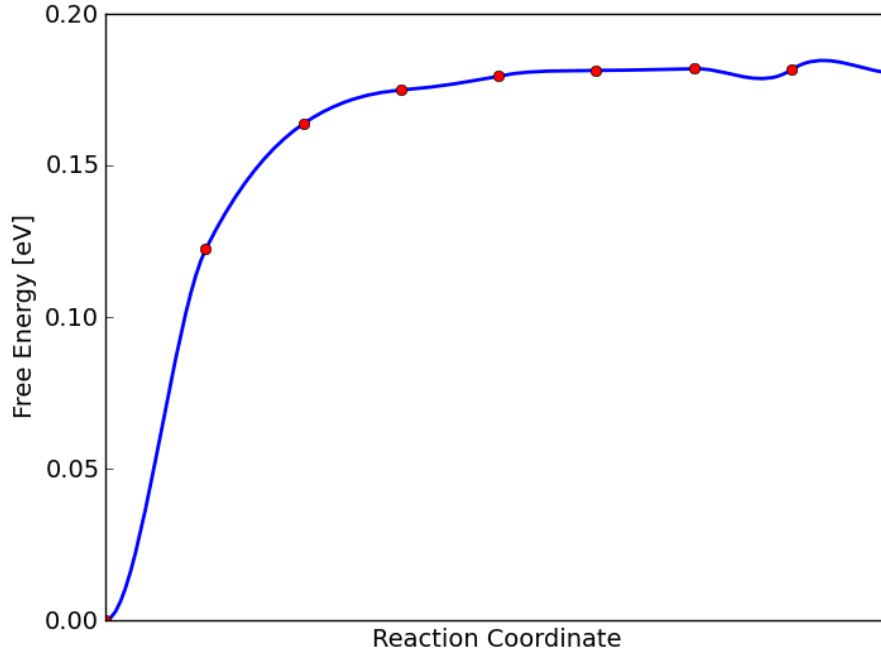


Figure 4.6: A minimum free energy path for removal of O_2 from a stepped Li_2O_2 surface. The free energy change for the O_2 going into gas phase is introduced gradually along the path. The free energy path shows no indications of any transition barrier for O_2 desorption of the Li_2O_2 surface.

density) [108].

The presence of lithium vacancies, V_{Li} , in bulk Li_2O_2 has been shown by Hummelsøj et al. to create holes in the valence band, indicating a possible band like conduction channel.

In the calculations performed for Paper C we find the formation energy of bulk V_{Li} to be $E_{\text{form}, V_{\text{Li}}} = 3.09$ eV in a $\text{Li}_{32}\text{O}_{32}$ supercell. We expect that the dominant part of vacancy formation during discharge and charging will be at the Li_2O_2 surface, where the formation energy of V_{Li} is somewhat cheaper as was discussed in section 4.2 (LiO_2^* is effectively a surface V_{Li}). At the high potentials during charging, $U_{\text{ch}} > 3.09$ V, there will be a driving force to create V_{Li} in the bulk as well as on the surface.

In figure 4.7 a NEB minimum energy path for V_{Li} diffusion in bulk Li_2O_2 is presented. The results show a relatively low transition state at $E_{\text{TS}, V_{\text{Li}}} = 0.36$ eV. The jump rate is calculated from HTST as it is described in equation 2.19, giving a prefactor $\nu = 3.4 \times 10^{12} \text{ s}^{-1}$ and a rate of $k^{\text{HTST}} = 3.6 \times 10^6 \text{ s}^{-1}$ at room temperature. This shows that V_{Li} have significant mobility in bulk Li_2O_2 .

Recent HSE hybrid functional calculations, presented by Ong et al. [110] suggest that the created hole will localize at the vacancy, which will prevent band like conduction. In the absence of V_{Li} , polaronic holes are shown to have low transition barriers for diffusion [110, 109]. In the presence of V_{Li} the polaronic holes will, however, be trapped at the vacancy and vacancy diffusion is likely to

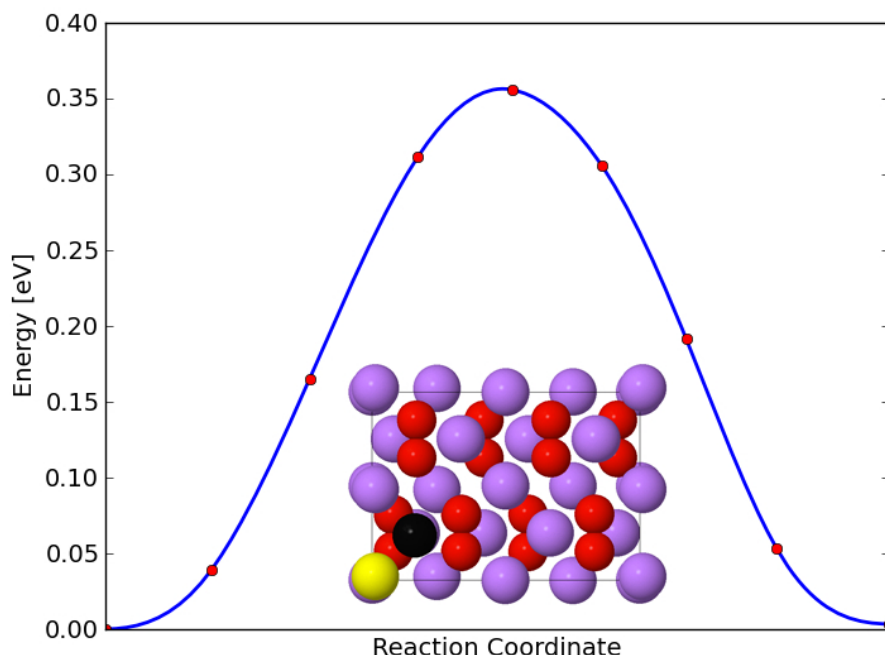


Figure 4.7: The minimum energy path for V_{Li} diffusion in bulk Li_2O_2 . The atomic structure for the initial state of the calculation is displayed, with V_{Li} : black, diffusing Li: yellow, other Li: purple and O: red.

govern the charge transport [110].

4.5 Selective Sulfur Poisoning

In Paper D the possibility of controlling Li_2O_2 growth with selective poisoning of S and SO_2 is discussed. In this section the results that are presented in the paper will only be briefly discussed. It is therefore recommended that Paper D is read before reading this section.

In Paper D we look at the binding of S and SO_2 at reactive sites on the $(1\bar{1}00)$ and (0001) surfaces. While S is seen to bind more favorably to a step/kink site at the (0001) surface, then SO_2 bind preferably to the $(1\bar{1}00)$ surface step. SO_2 forms a more stable surface species than S and in a oxygen rich environment, as is the case in the oxygen electrode, SO_2 is likely to be a more relevant adsorbate.

It is interesting to note that since SO_2 binds on top of the step edge rather than in front of it, then it is not blocking the nucleation sites at the step. It is, however, the effective transfer of SO_2 to a less stable (by 1.5 eV) terrace site, during growth, that makes reactions at the step less favorable than before.

One unanswered question from this initial study for the poisoning is how the SO_2 will affect the charging process. Another one is how mobile the SO_2 are on the surface, will they move along with the growth of the step or stay put in the

less stable terrace site.

4.6 Summary

In this chapter it has been shown that both electrochemical growth and decomposition of Li_2O_2 can take place at low overpotentials. It has also been shown how the lowering of the effective potential makes 6 step mechanisms favorable for charge.

The minimum energy path for thermal desorption of O_2 from a Li_2O_2 surface has been calculated with the conclusion that transition barriers are not likely to be significant in comparison with the surface binding energy of the molecule.

It has been discussed how the formation of V_{Li} creates holes in the valence band of Li_2O_2 that localize at vacancies. The mobility of the V_{Li} in bulk Li_2O_2 can be the basis for some charge transfer, although the mobility of the polaronic holes is significantly higher in the absence of V_{Li} .

Finally discussions were made on the preferential binding of SO_2 to $(1\bar{1}00)$ surface step sites and how the presence of SO_2 makes growth at the step less favorable, according to the calculations. The initial results give good indication for using SO_2 to control growth of Li_2O_2 and further investigations are on their way.

Bibliography

- [1] T. Ogasawara, A. Débart, M. Holzapfel, P. Novák, and P. G. Bruce. Rechargeable Li_2O_2 electrode for lithium batteries. *J. Am. Chem. Soc.*, 128(4):1390–1393, February 2006.
- [2] M. S. Whittingham. Lithium batteries and cathode materials. *Chem. Rev.*, 104(10):4271–301, October 2004.
- [3] G. Girishkumar, B. McCloskey, A. C. Luntz, S. Swanson, and W. Wilcke. Lithium-Air Battery: Promise and Challenges. *The Journal of Physical Chemistry Letters*, 1(14):2193–2203, July 2010.
- [4] J. S. Hummelshøj, T. Vegge, and J. K. Nørskov. Computational investigation and design of coordination compounds for hydrogen storage. *Technical University of Denmark*, (February), 2009.
- [5] J. Voss, J. S. Hummelshøj, Z. Lodziana, and T. Vegge. Structural stability and decomposition of $\text{Mg}(\text{BH}_4)_2$ isomorphs-an ab initio free energy study. *Journal of physics.: Condensed Matter*, 21(1):012203, January 2009.
- [6] T. Vegge, J. G. Howalt, S. Lysgaard, J. S. G. Mýrdal, N. Bork, and J. S. Hummelshøj. Computational design of catalysts, electrolytes and materials for energy storage. In Prof. Stephen Suib, editor, *New and future developments in catalysis: Batteries, hydrogen storage and fuel cells*, chapter Computatio. Elsevier, 2013.
- [7] et al. Hummelshøj, J. S. Density functional theory based screening of ternary alkali-transition metal borohydrides: a computational material design project. *The Journal of chemical physics*, 131(1):014101, July 2009.
- [8] M. Born and R. Oppenheimer. Zur Quantentheorie der Molekeln. *Annalen der Physik*, 389:457–484, 1927.
- [9] P. Hohenberg and W. Kohn. Inhomogeneous Electron Gas. *Phys. Rev.*, 136(3B):864, 1964.
- [10] W Kohn and L.J. Sham. Self-consistent equations including exchange and correlation effects. *Phys. Rev.*, 140(4A):A1133, 1965.

- [11] W. Kohn. Nobel Lecture: Electronic structure of matter-wave functions and density functionals. *Reviews of Modern Physics*, 71(5):1253–1266, October 1999.
- [12] D. M. Ceperley and B. J. Alder. Ground state of the electron gas by a stochastic method. *Physical Review Letters*, 45(7), 1980.
- [13] K. Kobayashi, N. Kurita, H. Kumahora, and K. Tago. Bond-energy calculations of Cu_2 , Ag_2 , and CuAg with the generalized gradient approximation. *Physical Review A*, 43(11):5810–5813, 1991.
- [14] K. Kobayashi, N. Kurita, H. Kumahora, K. Tago, and K. Ozawa. Nonlocal-density-functional bond-energy calculations of cage-shaped carbon fullerenes: C_{32} and C_{60} . *Physical Review B*, 45(23):690–693, 1992.
- [15] J. P. Perdew, J. A. Chevary, and S. H. Vosko. Atoms, molecules, solids, and surfaces: Applications of the generalized gradient approximation for exchange and correlation. *Physical Review B*, 46(11), 1992.
- [16] J. P. Perdew, K. Burke, and M. Ernzerhof. Generalized Gradient Approximation Made Simple. *Physical review letters*, 77(18):3865–3868, October 1996.
- [17] B. Hammer, L. B. Hansen, and J. K. Nørskov. Improved adsorption energetics within density-functional theory using revised Perdew-Burke-Ernzerhof functionals. *Phys. Rev. B*, 59(11):7413–7421, 1999.
- [18] P. J. Stephens and F. J. Devlin. Ab Initio Calculation of Vibrational Absorption and Circular Dichroism Spectra Using Density Functional Force Fields. *The Journal of . . .*, 98(45):11623–11627, 1994.
- [19] J. Heyd, G. E. Scuseria, and M. Ernzerhof. Hybrid functionals based on a screened Coulomb potential. *The Journal of Chemical Physics*, 118(18):8207, 2003.
- [20] J. J. Mortensen, L. B. Hansen, and K. W. Jacobsen. Real-space grid implementation of the projector augmented wave method. *Phys. Rev. B*, 71:035109, 2005.
- [21] J. Enkovaara, C. Rostgaard, J. J. Mortensen, J. Chen, M. Dulak, L. Ferrighi, J. Gavnholt, C. Glinsvad, V. Haikola, H. A. Hansen, H. H. Kristofersen, M. Kuisma, A. H. Larsen, L. Lehtovaara, M. Ljungberg, O. Lopez-Acevedo, P. G. Moses, J. Ojanen, T. Olsen, V. Petzold, N. A. Romero, J. Stausholm-Møller, M. Strange, G. A. Tritsarlis, M. Vanin, M. Walter, B. Hammer, H. Hakkinen, G. K. H. Madsen, R. M. Nieminen, J. K. Nørskov, M. Puska, T. T. Rantala, J. Schiøtz, K. S. Thygesen, and K. W. Jacobsen. Electronic structure calculations with GPAW : a real-space implementation of the projector augmented-wave method. *J. Phys.: Condens. Matter*, 253202(22):253202, 2010.
- [22] P. E. Blöchl. Projector augmented-wave method. *Phys. Rev.*, 50(24):17953, 1994.

- [23] P. E. Blöchl, C. J. Först, and J. Schimpl. Projector augmented wave method : ab initio molecular dynamics with full wave functions. *Bull. Mater. Sci.*, 26(1):33–41, 2003.
- [24] D. A. McQuarrie. *Quantum chemistry*. University Science Books, 1983.
- [25] H. C. Andersen. Rattle: A Velocity Molecular Version of the Shake Algorithm for Molecular Dynamics Calculations for Dynamics Calculations. *Journal of Computational Physics*, pages 24–34, 1983.
- [26] A. Voter. Hyperdynamics: Accelerated Molecular Dynamics of Infrequent Events. *Physical Review Letters*, 78(20):3908–3911, May 1997.
- [27] J. P. Ryckaert, G. Ciccotti, and H. J. C. Berendsen. Numerical integration of the cartesian equations of motion of a system with constraints: molecular dynamics of n-alkanes. *Journal of Computational Physics*, 23:327–341, 1977.
- [28] E. Pollak and P. Talkner. Reaction rate theory: what it was, where is it today, and where is it going? *Chaos (Woodbury, N.Y.)*, 15(2):26116, June 2005.
- [29] G. H. Vineyard. Frequency factors and isotope effects in solid state rate processes. *Journal of Physics and Chemistry of Solids*, 3:121–127, 1957.
- [30] J. H. Van’t Hoff. *Etudes de dynamique chimique*. 1884.
- [31] S. A. Arrhenius. . *Zeitschrift fur Physik Chemie*, 4:226–248, 1889.
- [32] H. Jonsson, G. Mills, and K. W. Jacobsen. *Classical and Quantum Dynamics in Condensed Phase Systems*. 1998.
- [33] G. Henkelman and H. Jónsson. Improved Tangent Estimate in the NEB method for Finding Minimum Energy Paths and Saddle Points. *The Journal of Chemical Physics*, 2000.
- [34] G. Henkelman, B. P. Uberuaga, and H. Jónsson. A climbing image nudged elastic band method for finding saddle points and minimum energy paths. *The Journal of Chemical Physics*, 113(22):9901, 2000.
- [35] G. Henkelman and H. Jónsson. A dimer method for finding saddle points on high dimensional potential surfaces using only first derivatives. *Journal of Chemical Physics*, 111(15), 1999.
- [36] C. J. Cramer. *Essentials of Computational Chemistry*. Wiley, second edition, 2004.
- [37] J. K. Nørskov, J. Rossmeisl, A. Logadottir, L. Lindqvist, J. R. Kitchin, T. Bligaard, and H. Jonsson. Origin of the overpotential for oxygen reduction at a fuel-cell cathode. *J. Phys. Chem. B*, 108:17886–17892, 2004.

- [38] I. C. Man, H.-Y. Su, F. Calle-Vallejo, H. A. Hansen, J. I. Martínez, N. G. Inoglu, J. Kitchin, T. F. Jaramillo, J. K. Nørskov, and J. Rossmeisl. Universality in Oxygen Evolution Electrocatalysis on Oxide Surfaces. *ChemCatChem*, 3(7):1159–1165, July 2011.
- [39] J. Greeley, I. E. L. Stephens, A. S. Bondarenko, T. P. Johansson, H. A. Hansen, T. F. Jaramillo, J. Rossmeisl, I. Chorkendorff, and J. K. Nørskov. Alloys of platinum and early transition metals as oxygen reduction electrocatalysts. *Nature chemistry*, 1(7):552–6, October 2009.
- [40] J. Greeley, T. F. Jaramillo, J. Bonde, I. Chorkendorff, and J. K. Nørskov. Computational high-throughput screening of electrocatalytic materials for hydrogen evolution. *Nature materials*, 5(11):909–13, November 2006.
- [41] J. B. Goodenough. Rechargeable batteries: challenges old and new. *Journal of Solid State Electrochemistry*, 16(6):2019–2029, May 2012.
- [42] S. J. Harris, A. Timmons, D. R. Baker, and C. Monroe. Direct in situ measurements of Li transport in Li-ion battery negative electrodes. *Chemical Physics Letters*, 485(4-6):265–274, January 2010.
- [43] R. Bhattacharyya, B. Key, H. Chen, A. S. Best, A. F. Hollenkamp, and C. P. Grey. In situ NMR observation of the formation of metallic lithium microstructures in lithium batteries. *Nature materials*, 9(6):504–10, June 2010.
- [44] Y. Inaguma, C. Liqun, and M. Itoh. High Ionic Conductivity in Lithium Lanthanum Titanate. *Solid State ...*, 86(10):689–693, 1993.
- [45] Y. Harada, T. Ishigaki, H. Kawai, and J. Kuwano. Lithium ion conductivity of polycrystalline perovskite $\text{La}_{0.672-x}\text{Li}_{3x}\text{TiO}_3$ with ordered and disordered arrangements of the A-site ions. *Solid State Ionics*, 108:407–413, 1998.
- [46] V. Thangadurai, A. K. Shukla, and J. Gopalakrishnan. New lithium-ion conductors based on the NASICON structure. *Journal of Materials Chemistry*, 9(3):739–741, 1999.
- [47] M. Sato, T. Suzuki, K. Yoshida, K. Uematsu, K. Toda, and Z. Ye. Synthesis and properties of lithium ion conductors $\text{Li}_{(3-2x)}(\text{Sc}_{(1-x)}\text{Zr}_x)_2(\text{PO}_4)_3$. *J. Alloys Comp.*, 250:510–514, 1997.
- [48] H. Y-P. Hong. Crystal Structure and Ionic Conductivity of $\text{Li}_4\text{Zn}(\text{GeO}_4)_4$ and other new Li^+ superionic conductors. *Mat. Res. Bull.*, 13:117–124, 1978.
- [49] R. Kanno and M. Murayama. Lithium Ionic Conductor Thio-LISICON: The $\text{Li}_2\text{S}-\text{GeS}_2-\text{P}_2\text{S}_5$ System. *Journal of The Electrochemical Society*, 148(7):A742, 2001.
- [50] V. Thangadurai. Novel Fast Lithium Ion Conduction in Garnet-Type $\text{Li}_5\text{La}_3\text{M}_2\text{O}_{12}$. *Journal of the American ...*, 40:437–440, 2003.

- [51] N. Kamaya, K. Homma, Y. Yamakawa, M. Hirayama, R. Kanno, M. Yone-mura, T. Kamiyama, Y. Kato, S. Hama, K. Kawamoto, and A. Mitsui. A lithium superionic conductor. *Nature materials*, 10(9):682–6, September 2011.
- [52] A. Züttel, A. Borgschulte, and S. Orimo. Tetrahydroborates as new hydrogen storage materials. *Scripta Materialia*, 56(10):823–828, May 2007.
- [53] S. Orimo, Y. Nakamori, J. R. Eliseo, A. Züttel, and C. M. Jensen. Complex hydrides for hydrogen storage. *Chemical reviews*, 107(10):4111–32, October 2007.
- [54] M. Matsuo, Y. Nakamori, S. Orimo, H. Maekawa, and H. Takamura. Lithium superionic conduction in lithium borohydride accompanied by structural transition. *Applied Physics Letters*, 91(22):224103, 2007.
- [55] V. Epp and M. Wilkening. Fast Li diffusion in crystalline LiBH_4 due to reduced dimensionality: Frequency-dependent NMR spectroscopy. *Physical Review B*, 82(2):020301, July 2010.
- [56] M. Matsuo and S. Orimo. Lithium Fast Ionic Conduction in Complex Hydrides: Review and Prospects. *Advanced Energy Materials*, 1:161–172, 2011.
- [57] K. Takahashi, K. Hattori, and T. Yamazaki. All-solid-state lithium battery with LiBH_4 solid electrolyte. *Journal of Power . . .*, 226:61–64, 2012.
- [58] H. Maekawa and M. Matsuo. Halide-stabilized LiBH_4 , a room-temperature lithium fast-ion conductor. *Journal of the . . .*, 131(3):894–895, January 2009.
- [59] H. Oguchi, M. Matsuo, J. S. Hummelshøj, T. Vegge, J. K. Nørskov, T. Sato, Y. Miura, H. Takamura, H. Maekawa, and S. Orimo. Experimental and computational studies on structural transitions in the LiBH_4 -LiI pseudobinary system. *Applied Physics Letters*, 94(14):141912, 2009.
- [60] R. Miyazaki, T. Karahashi, N. Kumatani, and Y. Noda. Room temperature lithium fast-ion conduction and phase relationship of LiI stabilized LiBH_4 . *Solid State Ionics*, 192(1):143–147, June 2011.
- [61] C. Pistorius. Melting and polymorphism of lithium tetrahydroborate to 45 kbar. *Z. Phys. Chem.*, 88:253–263, 1974.
- [62] K.N. Semenenko, A.P. Chavgun, and V.N. Surov. No Title. *Russ. J. Inorg. Chem*, 16:271, 1971.
- [63] J-Ph. Soulie, G. Renaudin, R. Cerny, and K. Yvon. Lithium borohydride LiBH_4 :I. Crystal structure. *Journal of alloys and compounds*, 346:200–205, 2002.
- [64] Z. Lodziana and T. Vegge. Structural Stability of Complex Hydrides: LiBH_4 Revisited. *Physical Review Letters*, 93(14):145501, September 2004.

- [65] Z. Lodziana and T. Vegge. Lodziana and Vegge Reply:. *Physical Review Letters*, 97(11):119602, September 2006.
- [66] M. R. Hartman, J. J. Rush, T. J. Udovic, R. C. Jr. Bowman, and S. J. Hwang. Structure and vibrational dynamics of isotopically labeled lithium borohydride using neutron diffraction and spectroscopy. *J. Solid State Chem.*, 180:1298–1305, 2007.
- [67] Y. Filinchuk and D. Chernyshov. Looking at hydrogen atoms with X-rays: comprehensive synchrotron diffraction study of LiBH_4 . *Acta Cryst. A.*, 63:240, 2007.
- [68] Y. Filinchuk, D. Chernyshov, and R. Cerny. The lightest borohydride probed by synchrotron diffraction: experiment calls for a new theoretical revision. *J. Phys. Chem. C.*, 112:10579–10584, 2008.
- [69] Y. Filinchuk, D. Chernyshov, and V. Dmitriev. Light metal borohydrides: crystal structures and beyond. *Zeitschrift für Kristallographie*, 223(10):649–659, October 2008.
- [70] T. Ikeshoji, E. Tsuchida, T. Morishita, K. Ikeda, M. Matsuo, Y. Kawazoe, and S. Orimo. Fast-ionic conductivity of Li^+ in LiBH_4 . *Physical Review B*, 83(14):1–5, April 2011.
- [71] P. Aeberhard, S. Williams, D. Evans, K. Refson, and W. David. Ab initio Nonequilibrium Molecular Dynamics in the Solid Superionic Conductor LiBH_4 . *Physical Review Letters*, 108(9):1–5, February 2012.
- [72] J. B. Yang, X. J. Wang, Q. Cai, W. B. Yelon, and W. J. James. Crystal and electronic structures of the complex hydride $\text{Li}_4\text{BN}_3\text{H}_{10}$. *Journal of Applied Physics*, 102(3):033507, 2007.
- [73] Y. E. Filinchuk and K. Yvon. On the Composition and Crystal Structure of the New Quaternary Hydride Phase $\text{Li}_4\text{BN}_3\text{H}_{10}$. *Inorganic ...*, 45(4):1433–1435, 2006.
- [74] G. P. Meisner, M. L. Scullin, M. P. Balogh, F. E. Pinkerton, and M. S. Meyer. Hydrogen release from mixtures of lithium borohydride and lithium amide: a phase diagram study. *The journal of physical chemistry. B*, 110(9):4186–92, March 2006.
- [75] P. A. Chater, W. I. F. David, S. R. Johnson, P. P. Edwards, and P. A. Anderson. Synthesis and crystal structure of $\text{Li}_4\text{BH}_4(\text{NH}_2)_3$. *Chemical communications (Cambridge, England)*, 4(23):2439–41, June 2006.
- [76] H. Wu, W. Zhou, and T. J. Udovic. Structures and Crystal Chemistry of Li_2BNH_6 and $\text{Li}_4\text{BN}_3\text{H}_{10}$. *Chemistry of ...*, (9):1245–1247, 2008.
- [77] T. Noritake, M. Aoki, S. Towata, a. Ninomiya, Y. Nakamori, and S. Orimo. Crystal structure analysis of novel complex hydrides formed by the combination of LiBH_4 and LiNH_2 . *Applied Physics A*, 83(2):277–279, February 2006.

- [78] M. Matsuo, A. Remhof, P. Martelli, R. Caputo, M. Ernst, Y. Miura, T. Sato, H. Oguchi, H. Maekawa, H. Takamura, A. Borgschulte, A. Züttel, and S. Orimo. Complex hydrides with $(\text{BH}_4)^-$ and $(\text{NH}_2)^-$ anions as new lithium fast-ion conductors. *Journal of the American Chemical Society*, 131(45):16389–91, November 2009.
- [79] M. Matsuo, T. Sato, Y. Miura, H. Oguchi, Y. Zhou, H. Maekawa, H. Takamura, and S. Orimo. Synthesis and Lithium Fast-Ion Conductivity of a New Complex Hydride $\text{Li}_3(\text{NH}_2)_2\text{I}$ with Double-Layered Structure. *Chemistry of Materials*, 22(9):2702–2704, May 2010.
- [80] G. Kresse and J. Furthmüller. Efficient iterative schemes for ab initio total-energy calculations using a plane-wave basis set. *Physical review. B, Condensed matter*, 54(16):11169–11186, October 1996.
- [81] S. R. Bahn and K. W. Jacobsen. An object-oriented scripting interface to a legacy electronic structure code. *Comput. Sci. Eng.*, 4:56–66, 2002.
- [82] A. El Kharbachi, I. Nuta, F. Hodaj, and M. Baricco. Above room temperature heat capacity and phase transition of lithium tetrahydroborate. *Thermochimica Acta*, 520(1-2):75–79, June 2011.
- [83] V.E. Gorbunov, K.S. Gavrichiev, V.L. Zalukaev, G.A. Sharpataya, and M.S.I. Baku. *N. Zh. Neorg. Khim.*, 29:2333–2337, 1984.
- [84] P. C. Aeberhard. *Computational Modelling of Structure and Dynamics in Lightweight Hydrides*. PhD thesis, 2012.
- [85] S. C. Abrahams and J. Kalnajs. The Lattice Constants of the Alkali Borohydrides and the Low Temperature Phase of Sodium Borohydride. *The Journal of Chemical Physics*, 22(3):434, 1954.
- [86] Y. Filinchuk, D. Chernyshov, A. Nevidomskyy, and V. Dmitriev. High-pressure polymorphism as a step towards destabilization of LiBH_4 . *Angewandte Chemie (International ed. in English)*, 47(3):529–32, January 2008.
- [87] Dadi Sveinbjörnsson. *Metal Borohydrides for Hydrogen Storage and Solid Electrolytes*. PhD thesis, Technical University of Denmark, 2010.
- [88] J. C. Slater. Atomic Radii in Crystals. *The Journal of Chemical Physics*, 41(10):3199, 1964.
- [89] R. D. Shannon. Revised effective ionic radii and systematic studies of interatomic distances in halides and chalcogenides. *Acta Crystallographica Section A: Crystal Physics, . . .*, 32:751, 1976.
- [90] S. Zhang, K. Xu, and T. Jow. Low-temperature performance of Li-ion cells with a LiBF_4 -based electrolyte. *Journal of Solid State Electrochemistry*, 7:147–151, 2003.
- [91] T. Nagaura. No Title. *Prog. Batteries Solar Cells*, 10:209, 1991.

- [92] K. Mizushima, P.C. Jones, P.J. Wiseman, and J.B. Goodenough. Li_xCoO_2 ($0 < x < 1$): A new cathode material for batteries of high energy density. *Mat. Res. Bull.*, 15:783–789, 1980.
- [93] M. M. Thackeray and W. I. F. David. Lithium insertion into manganese spinels. *Materials Research ...*, 18:461–472, 1983.
- [94] K. M. Abraham and Z. Jiang. A Polymer Electrolyte-Based Rechargeable lithium/Oxygen Battery. *J. Electrochem. Soc.*, 143(1):1–5, 1996.
- [95] T. Kuboki, T. Okuyama, T. Ohsaki, and N. Takami. Lithium-air batteries using hydrophobic room temperature ionic liquid electrolyte. *Journal of Power Sources*, 146(1-2):766–769, August 2005.
- [96] Y.-C. Lu, Z. Xu, H. A. Gasteiger, S. Chen, K. Hamad-Schifferli, and Y. Shao-Horn. Platinum-gold nanoparticles: a highly active bifunctional electrocatalyst for rechargeable lithium-air batteries. *Journal of the American Chemical Society*, 132(35):12170–1, September 2010.
- [97] J. S. Hummelshøj, J. Blomqvist, S. Datta, T. Vegge, J. Rossmeisl, K. S. Thygesen, A. C. Luntz, K. W. Jacobsen, and J. K. Nørskov. Communications: Elementary oxygen electrode reactions in the aprotic Li-air battery. *The J. of Chem. Phys.*, 132(7):071101, February 2010.
- [98] Z. Peng, S. A. Freunberger, L. J. Hardwick, Y. Chen, V. Giordani, F. Bardé, P. Novák, D. Graham, J.-M. Tarascon, and P. G. Bruce. Oxygen reactions in a non-aqueous Li^+ electrolyte. *Angew. Chem. Int. Ed.*, 50:6351–6355, July 2011.
- [99] M. W. Chase. NIST-JANAF Thermochemical Tables. *J. Phys. Chem. Ref. Data*, Monograph:1–1951, 1998.
- [100] M. D. Radin, J. F. Rodriguez, F. Tian, and D. J. Siegel. Lithium peroxide surfaces are metallic, while lithium oxide surfaces are not. *J. Am. Chem. Soc.*, 134(2):1093–103, January 2011.
- [101] M. D. Radin, F. Tian, and D. J. Siegel. Electronic structure of Li_2O_2 {0001} surfaces. *J. Mat. Sci.*, 47(21):7564–7570, May 2012.
- [102] K. C. Lau, L. A. Curtiss, and J. Greeley. Density Functional Investigation of the Thermodynamic Stability of Lithium Oxide Bulk Crystalline Structures as a Function of Oxygen Pressure. *J. Phys. Chem. C*, 115(47):23625–23633, December 2011.
- [103] Y. Mo, S. P. Ong, and G. Ceder. First-principles study of the oxygen evolution reaction of lithium peroxide in the lithium-air battery. *Phys. Rev. B*, 84:205446, 2011.
- [104] J. S. Hummelshøj, A. C. Luntz, and J. K. Nørskov. Theoretical evidence for low kinetic overpotentials in Li- O_2 electrochemistry. *J. Chem. Phys.* (submitted).

- [105] B. D. McCloskey, A. Speidel, R. Scheffler, D. C. Miller, V. Viswanathan, J. S. Hummelshøj, J. K. Nørskov, and A. C. Luntz. Twin Problems of Interfacial Carbonate Formation in Nonaqueous. *The Journal of Physical Chemistry Letters*, 3:997–1001, 2012.
- [106] D Xu, Z. Wang, J. Xu, L. Zhang, and X. Zhang. Novel DMSO-based electrolyte for high performance rechargeable Li-O₂ batteries. *Chemical communications*, 48(55):6948–50, July 2012.
- [107] J. Chen, J. S. Hummelshøj, K. S. Thygesen, J. S. G. Mýrdal, J. K. Nørskov, and T. Vegge. The role of transition metal interfaces on the electronic transport in lithium-air batteries. *Catalysis Today*, 165(1):2–9, May 2011.
- [108] V. Viswanathan, K. S. Thygesen, J. S. Hummelshøj, J. K. Nørskov, G. Girishkumar, B. D. McCloskey, and A. C. Luntz. Electrical conductivity in Li₂O₂ and its role in determining capacity limitations in non-aqueous Li-O₂ batteries. *J. Chem. Phys.*, 135(21):214704, December 2011.
- [109] J. M. Garcia-Lastra, J.S.G. Myrdal, K. S. Thygesen, and T. Vegge. DFT+U study of polaronic conduction in Li₂O₂ and Li₂CO₃: Implications for Li-air batteries. *J. Phys. Chem. C (submitted)*.
- [110] S. Ong, Y. Mo, and G. Ceder. Low hole polaron migration barrier in lithium peroxide. *Phys. Rev. B*, 85(8):081105, February 2012.

Papers

The effect of heat treatment on the lithium ion conduction of the $\text{LiBH}_4\text{-LiI}$ solid solution

Dadi Sveinbjörnsson¹, Jón Steinar Gardarsson Mýrdal¹, Didier Blanchard¹, Janet Jonna Bentzen¹, Takumi Hirata², Mogens Bjerg Mogensen¹, Poul Norby¹, Shin-ichi Orimo², Tejs Vegge¹.

¹Department of Energy Conversion and Storage, Technical University of Denmark, DK-4000 Roskilde, Denmark.

²Institute for Materials Research, Tohoku University, Sendai 980-8577, Japan.

The $\text{LiBH}_4\text{-LiI}$ solid solution is a good Li ion conductor and a promising crystalline electrolyte for all-solid-state lithium batteries. The focus of the present work is on the effect of heat treatment on the Li^+ conduction. Solid solutions with a LiI content of 6.25% - 50% were synthesized by high energy ball milling and annealed at 140°C. Powder x-ray diffraction and scanning electron microscopy were used for characterizing the samples and for comparing their crystallite sizes and the density of defects before and after the annealing. The Li^+ conductivity was measured using impedance spectroscopy, resulting in conductivities exceeding 10^{-4} S/cm at 30°C and 10^{-2} S/cm at 140°C. It was found that the creation of defect-rich microstructures by ball milling increased the specific conductivities of these compounds significantly. The phase transition temperatures between the orthorhombic and hexagonal structures of LiBH_4 were measured using differential scanning calorimetry. The measured transition temperatures range from 100°C to -70°C and show a linear decrease of 70°C for every 10% of LiI addition up to a LiI content of 25%. The relative stability of the two structures and their entropy behavior was calculated using density functional theory.

I. INTRODUCTION

Lithium battery research is growing ever more important as the need for more efficient and more sustainable methods for energy storage continues to grow rapidly. This is in particular true for the energy and transportation sectors. Today, the primary application of lithium batteries is in the portable electronics sector. But when it comes to applications in systems on a larger scale, existing battery technologies fall short on price, energy density, safety and charge-discharge cycle lifetime. Commercial Li-ion batteries use flammable organic liquid or gel electrolytes. This causes safety issues, which only grow worse as the demands on the energy density of the systems increase^{1,2}. Furthermore, the usage of liquid or gel electrolytes can result in diminished cell capacity and limited charge-discharge cycle life due to dendrite formation at the electrode-electrolyte interface³.

Replacing the currently used liquid and gel electrolytes with solid-state electrolytes would enhance the safety and extend the cycle life of the batteries. However, designing a suitable solid electrolyte material with sufficient chemical and electrochemical stability, as well as offering a

sufficiently high lithium ion conduction and negligible electronic conduction, remains a challenge⁴.

Various types of crystalline solid-state Li^+ conducting materials are known¹. Among these are Li_3N ⁵, perovskite type oxides such as lithium lanthanum titanate (LLTO)⁶⁻⁸, NASICON type structures^{9,10}, LISICON type structures¹¹ and $\text{Li}_{10}\text{GeP}_2\text{S}_{12}$ ¹². There are, however, some problems with the usage of many of these materials as solid electrolytes in lithium batteries. The decomposition voltage of Li_3N is too low for practical use. LLTO and NASICON are not stable in contact with elemental lithium and reducible Ti^{4+} ions make the electronic conductivity of LLTO too high¹³. The Li^+ conductivity of LISICON is rather low, and in some cases decreases with time¹⁴.

Lithium borohydride, LiBH_4 , is lightweight (0.666 g/cm³) and has been investigated extensively as a possible hydrogen storage material¹⁵⁻²⁰. In recent years, lithium borohydride has also gained increased attention as a potential crystalline solid electrolyte material for lithium batteries²¹⁻²³. At room temperature it has a poorly Li^+ conducting orthorhombic crystal structure (Pnma, approximately 10^{-8} S/cm at 30°C), but around 110°C it undergoes a

reversible structural transition to a highly Li^+ conducting hexagonal structure ($\text{P6}_3\text{mc}$, approximately 10^{-3} S/cm at 120°C)^{21,24}. In the following, the two polymorphs will be referred to as the LT phase (orthorhombic) and HT phase (hexagonal), respectively.

The HT phase of LiBH_4 can be stabilized at room temperature by adding lithium halides (LiI , LiBr and LiCl), the LiI addition giving the best Li conduction results²⁵. It should be noted that $\beta\text{-LiI}$, the low-temperature modification of LiI below 0°C , has a $\text{P6}_3\text{mc}$ structure²⁶ and is thus isostructural with the HT phase of LiBH_4 . The $\text{LiBH}_4\text{-LiI}$ system forms a solid solution²⁷, and studies on its structure and properties have recently been published^{28,29}.

The present work focuses on the dependence of the lithium conduction on the LiI content and the microstructure of the $\text{LiBH}_4\text{-LiI}$ solid solution. The results are based both on experimental work and on density functional theory calculations.

II. COMPUTATIONAL

Calculations were performed using density functional theory as it is implemented in the Vienna *Ab-initio* Simulation Package (VASP)³⁰ with a plane wave basis set. For the non-valence electrons of boron atoms the PBE exchange and correlation functional³¹ and the projector augmented wave method (PAW)^{32,33} were used. All lithium electrons were included in the calculation. The energy cut-off was set to 350 eV and a $4\times 4\times 4$ Monkhorst-pack k-point mesh was used. The preparation of atomic structures and the setup of computational parameters was performed using the Atomic Simulation Environment (ASE)³⁴.

The ground state energy for the $(1-x)\text{LiBH}_4+x\text{LiI}$ system was calculated for seven different values of x , that is $x = \{0, 1/16, 1/8, 3/16, 1/4, 1/2, 1\}$, in both the LT (Pnma) and HT ($\text{P6}_3\text{mc}$) crystal structures of LiBH_4 . For structural optimization all forces were relaxed down to < 0.01 eV/Å.

III. EXPERIMENTAL

A. Synthesis

LiBH_4 powder (purity 95%) and LiI beads (purity 99%) were purchased from Alfa Aesar Co. The $(1-x)\text{LiBH}_4+x\text{LiI}$ samples were synthesized by planetary ball milling under Ar atmosphere. Pure LiBH_4 was also ball-milled for comparison. In each milling, a stainless steel vial with an inner volume of 250 ml was rotated at 650 rpm for 2 hours using a Fritsch

Pulverisette P6. A total of 2 g of precursor powder were inserted into the vial for each milling. 25 tungsten carbide balls were used and the sample to ball mass ratio was 1/100. No contamination from the milling vial or the balls was found in the diffraction patterns of the milled samples.

For the sample used in the impedance spectroscopy temperature cycling measurement (see figure 7) the procedure was the same as described above, except that a total of 0.5 g of precursor powder were rotated in a 45 ml vial on a Fritsch Pulverisette P7. Here the sample to ball mass ratio was 1/180.

B. Powder x-ray diffraction

After ball milling, the samples were characterized using a Cu K_α Bruker D8 diffractometer with a Bragg-Brentano geometry and a LynxEye detector, operating at 40 kV and 40 mA. All XRD measurements were performed at room temperature and under Ar atmosphere using an airtight polyethylene sample holder from Bruker Co. The exposure time was 3 s/step with a step size of 0.02° . The measurements were performed using a variable slit size. After the measurement, the data intensity was corrected for the variable slit size and the $\text{K}_\alpha 2$ signal was subtracted.

A fraction of each sample was annealed in a furnace at 140°C for 70 hours. XRD measurements were subsequently performed on the annealed powder in order to detect, by comparison with the non-annealed powder, the anticipated sintering effect of the heat treatment.

The diffraction peak positions were found using the GSAS refinement software. The full width at half maximum (FWHM) of the diffraction peaks was calculated using the peak fitting software FITYK³⁵. The contributions to the FWHM from the crystallite size and from the crystallographic defects were separated by fitting the size and strain parameters in

$$B(\theta) = \sqrt{\left(\frac{k\lambda}{D \cos \theta}\right)^2 + (4\eta \tan \theta)^2} + B_0^2 \quad (1)$$

to the measured FWHM values in each diffractogram. This expression for the peak broadening is a combination of the Scherrer equation for size broadening³⁶ and the Stokes and Wilson expression for strain broadening³⁷, where D is the average crystallite size and η is the strain. The shape factor k was assumed to be 0.9 and the instrumental broadening B_0 was 0.01.

C. Scanning electron microscopy

The microstructure was characterized using a JEOL 840 scanning electron microscope (SEM) with an acceleration voltage of 10 kV. The samples were transferred under vacuum from the glove box to the microscope using a portable vacuum transference system.

D. Impedance spectroscopy

The conductivity of the samples was determined by AC impedance spectroscopy using a PARSTAT 2273 potentiostat. The ball-milled powder was pressed into pellets with a diameter of 13 mm and a thickness of approx. 2.5 mm. Lithium foil was placed onto both faces of the pellets as electrodes. The powder and the lithium foil were pressed simultaneously at 1 ton/cm². The porosity of the pellets was estimated to be around 0.5. All preparation and measurements were carried out under Ar atmosphere. The frequency range of the impedance measurements was set from 100 mHz to 1 MHz. The samples were heated up from 30°C to 140°C in steps of 5°C or 10°C and then cooled back down to 30°C using the same step size. The samples were equilibrated at a constant temperature for at least 40 minutes prior to each measurement.

For the measurement of the conductivity of the 1/2LiBH₄+1/2LiI sample during five heating and cooling cycles (see fig. 7), a Hioki 3532-80 potentiostat was used and the pellet dimensions were 8 mm in diameter and 0.9 mm in thickness.

E. Differential scanning calorimetry

The phase transition temperatures of the (1-x)LiBH₄+xLiI samples were determined by differential scanning calorimetry (DSC), using a Netzsch DSC 200 F3 calorimeter. For each measurement, 10 mg of sample were sealed in an aluminum crucible under Ar atmosphere. The samples were heated from room temperature to 140°C at 2 °C/min, then kept at 140°C for 30 minutes and thereafter cooled to -170°C at 2 °C/min. A liquid nitrogen cryostat was used to control the temperature.

IV. RESULTS AND DISCUSSION

A. Density functional theory

Figure 1 shows the calculated energy difference between the P₆₃mc (HT) and Pnma (LT) structures

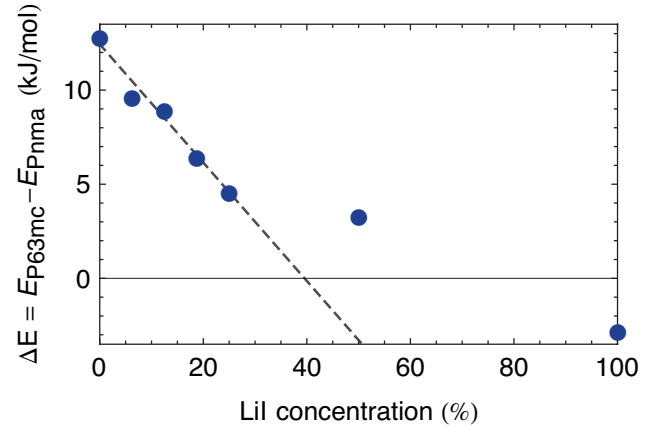


Figure 1 The ground state energy difference between the P₆₃mc (HT) and Pnma (LT) structures of LiBH₄ as a function of the content of LiI that has been substituted into the system. The stabilization of the HT structure relative to the LT structure is approximately linear up to a LiI content of 25%. The dotted line shows a linear fit of the datapoints for LiI contents from 0% to 25% to emphasize this.

as a function of iodine content in the (1-x)LiBH₄+xLiI system. Up to a LiI content of 25%, there is a close to linear stabilization with increasing iodine content, about 33 kJ/mol I. There seems to be little addition in stability by going from 25% iodine content to 50%, but for pure LiI the HT structure has become more stable than the LT structure. This increased stability of the HT structure versus the LT structure is, however, a poor indicator of the real HT stability for pure LiI because the LT structure of LiBH₄ is not the ground state structure of LiI. We do, nonetheless, believe that for smaller iodine contents the ground state energy calculations give a good estimate of the real stabilization in the (1-x)LiBH₄+xLiI system since we expect them to have a similar entropy behavior as a function of temperature. This claim is supported further in section IV.E by comparing the calculation results with the results of DSC measurements.

B. X-ray diffraction

The diffraction patterns of both the annealed and the non-annealed (1-x)LiBH₄+xLiI samples are shown in figure 2. A diffraction pattern of non-annealed LiBH₄ that has been ball milled for 2 hours is also shown for comparison. The pure ball-milled LiBH₄ has the LT structure, while the sample with 6.25% LiI is a blend of the LT and HT structures. For all samples with LiI content equal to or greater than 12.5%, only the HT phase is detected.

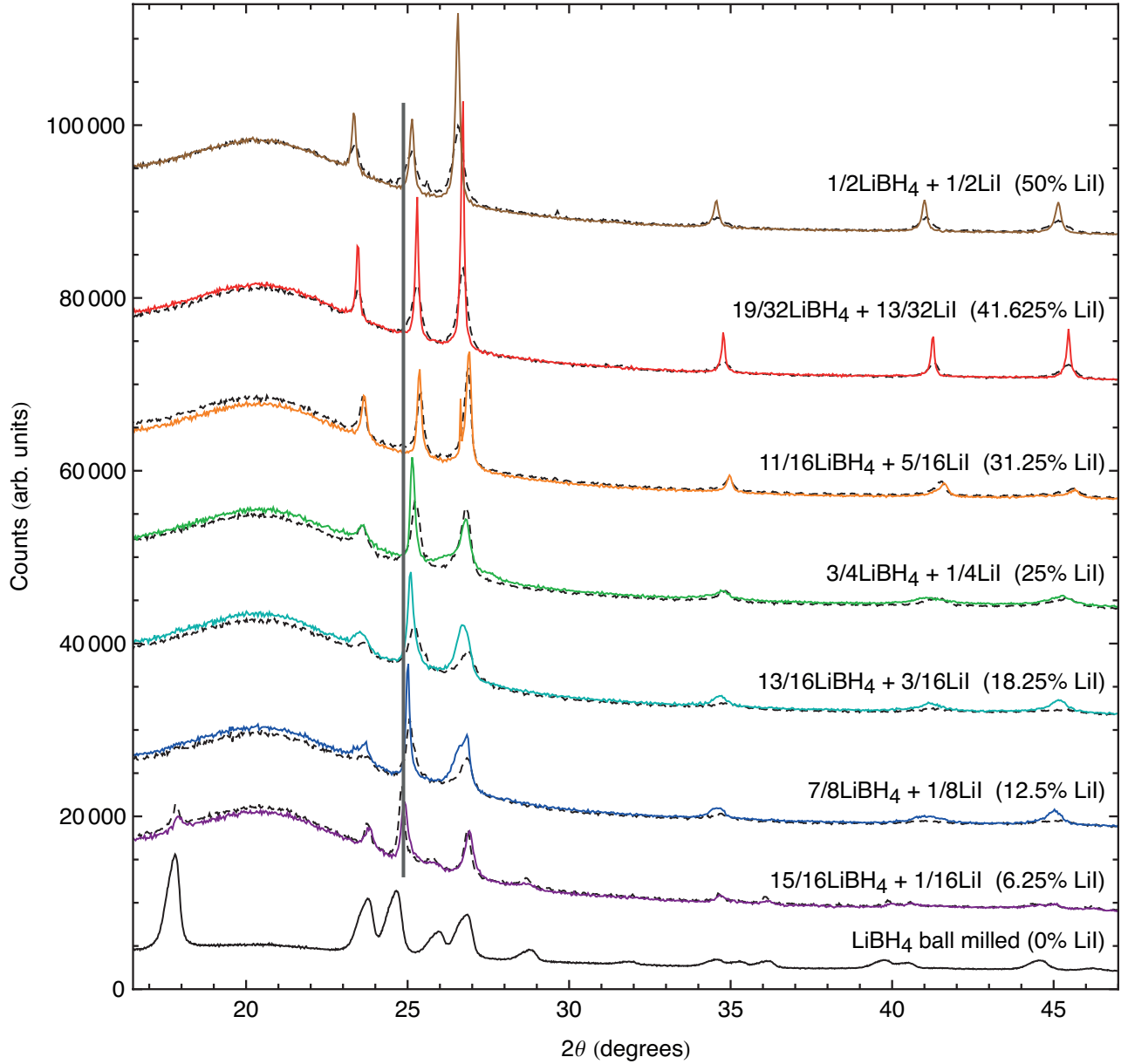


Figure 2 (color online) XRD patterns of $(1-x)\text{LiBH}_4 + x\text{LiI}$ solid solutions. The black, dashed lines show diffraction patterns of non-annealed samples, the colored, whole lines show diffraction patterns of samples which have been annealed at 140°C for 70 hours. The black, whole line shows the diffraction pattern of pure ball milled, non-annealed LiBH_4 for comparison. The vertical line at around 25° is drawn to emphasize the shift of the (002) reflection with LiI content. All measurements were performed at room temperature. The broad bump at the lowest angles is due to the polyethylene sample holder. The intensity of the diffraction pattern of the pure LiBH_4 has been scaled down by $1/3$ in order to better fit the intensities of the remaining patterns in the figure. The molar percentage of LiI is shown in parenthesis after the sample name for easier comparison with other figures in this work.

The positions of the reflections from the crystallographic planes (hk0), parallel to the hexagonal plan, are only slightly shifted to higher values when the LiI content is increased, reflecting a small expansion of the a axis with increased LiI content. The c axis, perpendicular to the hexagonal plan, is found to shrink with increasing LiI content up to 30% and then to expand with increasing LiI content between 30% and 50% (see figure 2, in

which a line is drawn to emphasize the shift of the (002) reflection).

The evolution of the lattice parameter c is plotted as a function of the LiI content in figure 3a. The non-monotonic evolution of the c -axis is unexpected and the contraction of c with increasing LiI content below a LiI content of 30% differs from what has previously been reported by Miyazaki et al.²⁸. For a LiI content above 30% the c -axis expands as

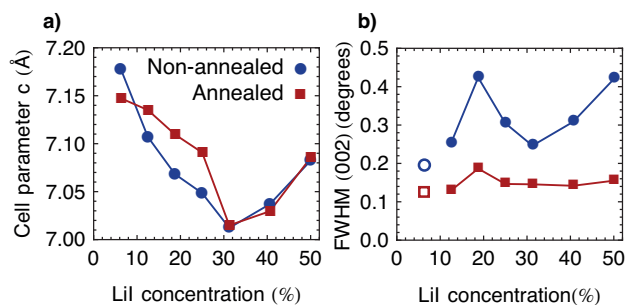


Figure 3 (color online) **a)** The evolution of the unit cell parameter c in $(1-x)\text{LiBH}_4+x\text{LiI}$ with LiI content. **b)** The full width at half maximum of the (002) reflection of the $(1-x)\text{LiBH}_4+x\text{LiI}$ diffraction patterns as a function of LiI content. The FWHM of the samples with 6.25% LiI content are shown with empty dots; their values are not reliable because of overlapping diffraction peaks from the LT and HT structures of LiBH_4 .

expected when compared with the unit cell parameters of the hexagonal phases of pure LiBH_4 and pure LiI respectively and is in agreement with the values reported by Miyazaki et al.²⁸ and Rude et al.²⁹.

One possible explanation for this behavior is the presence of solid solutions containing different amounts of iodine and different lattice constants that merge into one upon heating as reported by Rude et al.²⁹. Another possibility is the existence of some intermediate phases as described by Oguchi et al.²⁷. These effects could be the origin of the very asymmetric peak shapes and large peak broadening visible in figure 2 for low LiI content. Such broadening at low LiI content is also visible in the diffraction patterns of ref. 25 and 26.

Sintering and/or annealing effects are observed for the annealed LiBH_4 -LiI solid solutions in the form of narrower peaks for the annealed samples than for the non-annealed ones. However, the peculiar behavior of the c axis is still present in the annealed samples. As an example of the peak sharpening, the evolution of the full-width at half-maximum (FWHM) of the (002) reflection with LiI content is shown in figure 3b. The FWHM of the non-annealed powder varies with the LiI content and has a minimum at around 30% LiI content. This is also the LiI content for which the cell parameter c (see fig. 3a) is closest to the value reported for the cell parameters of pure LiBH_4 ²⁴. After the annealing, the FWHM values are almost independent of the LiI content.

The broadening contribution from the strain and the crystallite sizes was analyzed using equation 1. This analysis was performed on the FWHM of four to six peaks depending on the diffraction patterns.

Due to the limited quality of the data, no absolute values for D and η are reported herein. Their relative contribution and evolution will, however, be commented on in connection with the LiI content and the effect of the annealing.

It was found that before the annealing, the broadening due to the strain is dominant over the size effect up to a LiI content of 25%. Knowing that the FWHM values are larger for low LiI content, the density of defects is greater for samples with low LiI content than for those with high LiI content. After annealing, the strain values are smaller and almost independent of the LiI content. Furthermore, the crystallite sizes of the annealed powders are found to be around three times greater than those of the non-annealed powders for samples with LiI contents larger than 25%. Overall, the FWHM are found to be lowered by the heat treatment.

It should be noted that the difference in strain before and after the annealing is found to be smallest for the sample with 30% LiI content, which is the LiI content at which the minima in the cell parameter c and the FWHM before annealing are observed (see fig. 3). It should also be noted that the sample with 6.25% LiI content contains two coexisting structures with overlapping diffraction peaks at the position of the (002) reflection of the HT phase. Therefore the measured FWHM values are probably not accurate for this sample and have been left out for this analysis.

C. Scanning electron microscopy

Figure 4 shows SEM images of $1/2\text{LiBH}_4+1/2\text{LiI}$ powder. The sample in figure 4a was ball milled (as described in section III.A) but did not receive any heat treatment. The sample in figure 4b was ball milled and annealed in a furnace at 140°C for 70 hours. A comparison of the two images shows that sintering does occur during the heat treatment, as the average size of the particles and the agglomerates in the powder are larger after the annealing than before it. This supports the results on the FWHM of the x-ray diffraction data shown in figure 2 and 3b.

D. Conductivity

The impedance spectroscopy measurements resulted in a Nyquist plot showing a single arc. It is thus not possible to separate the contributions from the bulk and the grain boundary conductivities using only impedance spectroscopy^{38,39}. No contribution from the Li electrodes was observed. The Nyquist plots were all fitted using an (RQ) equivalent circuit

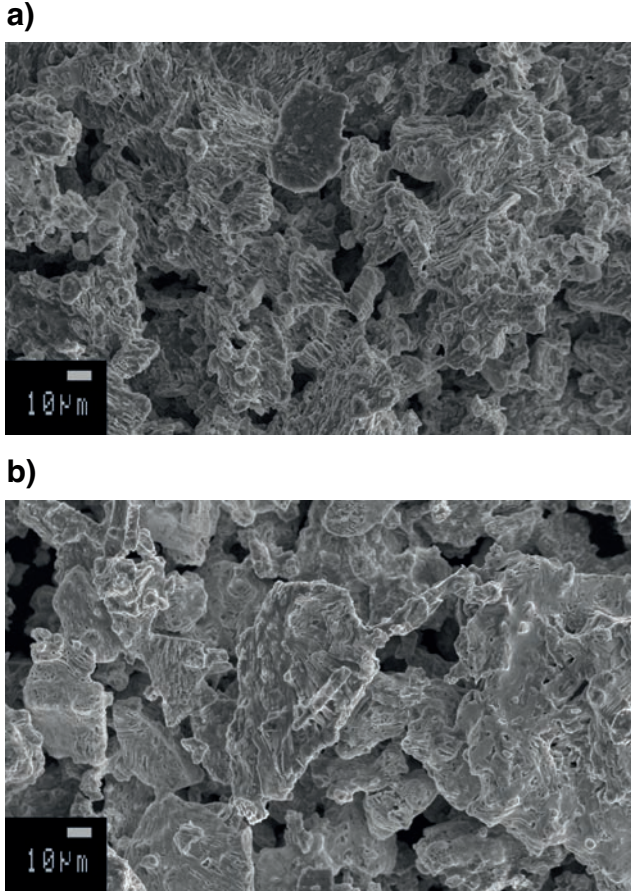


Figure 4 Scanning electron microscope images of $1/2\text{LiBH}_4+1/2\text{LiI}$. The scale in the lower left corner of the images shows the length of $10\ \mu\text{m}$. **a)** After ball milling but before annealing. **b)** After ball milling and annealing. It is clear that the average particle and agglomerate sizes are larger in the annealed sample than in the non-annealed sample.

model, i.e. a resistor and a constant phase element (CPE) in parallel. Examples of Nyquist plots can be found in the supplementary information to this work. The conductivity of the samples is given by

$$\sigma = \frac{d}{AR} \quad (2)$$

where R is the resistance obtained from the fit, d is the thickness of the sample and A its area.

Figure 5 shows an Arrhenius plot of the Li^+ conductivities measured for the different samples during heating and cooling (Nyquist plots and additional Arrhenius plots can be found in the supplementary information to this work). The pellets consisted of the as-milled powders and the measurements were performed while first heating the pellets from room temperature to 140°C and then cooling them back down to room temperature. The $(1-x)\text{LiBH}_4+x\text{LiI}$ solid solutions show very high ionic conductivity, with the sample with 40% LiI

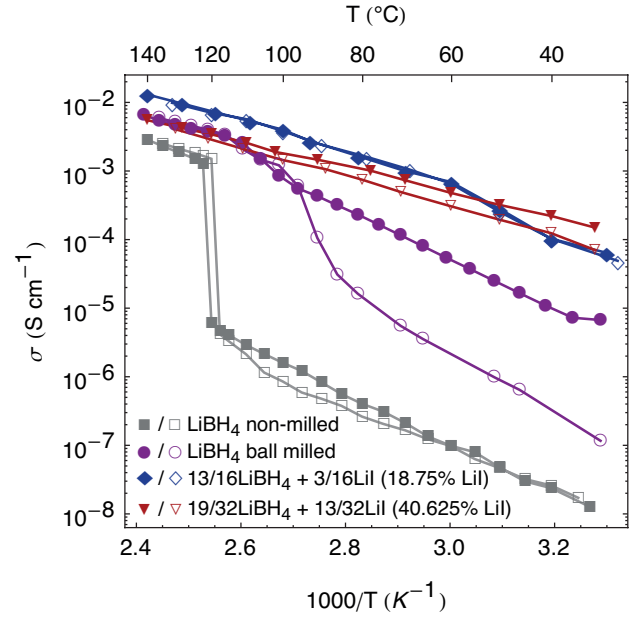


Figure 5 (color online) The Li^+ conductivities of pure LiBH_4 , both ball milled and non-milled, and of two mixing ratios of $(1-x)\text{LiBH}_4+x\text{LiI}$, obtained from impedance spectroscopy. For each sample, the filled symbols denote heating runs and the empty symbols denote cooling runs.

content exceeding $10^{-4}\ \text{S/cm}$ at 30°C and the 18.75% LiI containing sample exceeding $10^{-2}\ \text{S/cm}$ at 140°C .

Generally, the slopes of the Arrhenius plots vary with both LiI content and temperature. There is a general trend that the steepness of the plots decreases with increasing LiI content. This indicates that the activation energy of the Li^+ conduction decreases with increasing LiI content. Furthermore, as a result of the decreasing slopes with increasing LiI content, the samples with a low LiI content generally have a higher Li^+ conductivity at the highest measured temperatures than the samples with high LiI content.

Ball milling and heat treatment of the samples are also important for their conductivity. The as-received (non-milled) LiBH_4 is in its poorly conducting LT phase. At around 120°C , the sample changes to the HT phase and the conductivity increases by more than two orders of magnitude, as expected²¹. This trend in the conductivity is fully reversible upon cooling, with a very small hysteresis. The ball milled LiBH_4 is also in the poorly conducting LT phase (see figure 2). However, defects arising during the ball milling may open up new Li^+ conduction pathways. This causes an increase in conductivity by almost three orders of magnitude close to room temperature, compared to the non-milled LiBH_4 . When the ball-milled LiBH_4 is heated up above the phase transition temperature it takes on the HT structure, presumably mending some of the defects caused by the ball

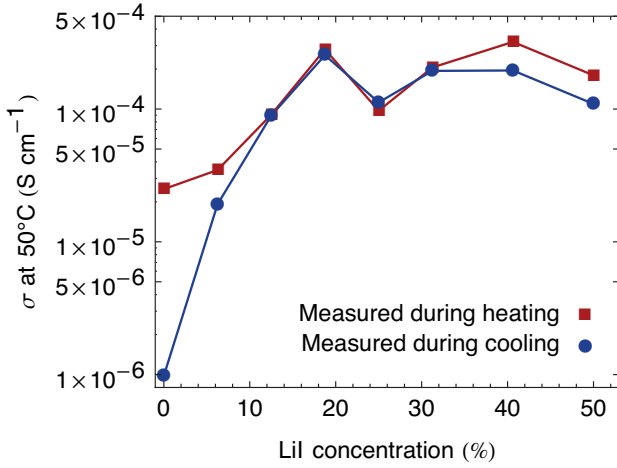


Figure 6 (color online) The Li^+ conductivity of the $(1-x)\text{LiBH}_4+x\text{LiI}$ samples at 50°C as a function of LiI content for non-annealed (red rectangles) and annealed (blue circles) samples. The datapoints for pure LiBH_4 (0% LiI content) in this figure are from a measurement on ball-milled LiBH_4 .

milling. The return to the LT phase when cooling the sample down should mend the defects even further. Some of the conduction pathways present during the heating run are then closed as illustrated by the large fall of the conductivity between the heating and the cooling runs. After the thermal treatment, the sample is not, however, defect-free and the conductivity of the ball milled sample is still higher than that of the as-received LiBH_4 .

The conductivity values at 50°C are shown as a function of the LiI content in figure 6. This temperature is chosen because it represents an approximate temperature at which a lithium battery could be operated. The conductivity values at 50°C are equal or higher during the heating runs than during the cooling runs. The difference in the conductivity between the heating and the cooling measurements is smallest for samples with LiI content between 18% and 30%. This result is in good harmony with the result shown in figure 3b, namely that the particle size and/or density of defects in the non-annealed samples is closest to those in the annealed samples for solid solutions with moderate LiI content.

Together, the XRD and conductivity results indicate that the microstructure of the samples is important for their conductivity, and that freshly ball-milled samples with defect-rich microstructure yield higher conductivity values than those in which the defects have been mended by annealing. This is also emphasized by the fact that the measured conductivity does not follow the evolution of the lattice parameter c (see figure 3a), which has a minimum at a LiI content of 30%. If the left part of

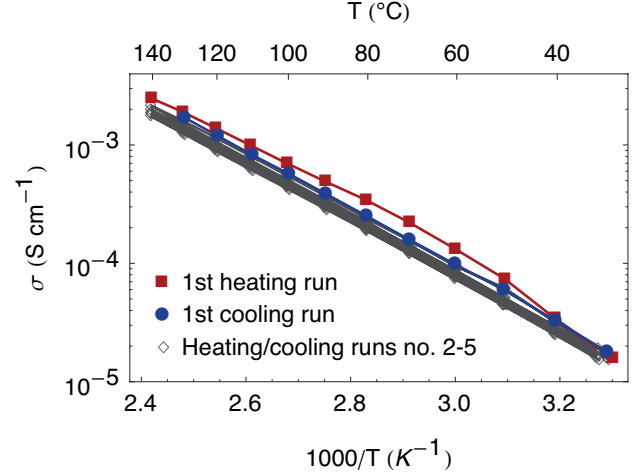


Figure 7 (color online) The conductivity of $1/2\text{LiBH}_4+1/2\text{LiI}$ obtained by impedance spectroscopy during five heating/cooling cycles. The red rectangles and blue circles show the results of the first heating and cooling runs respectively. The diamonds show the results of the four subsequent heating and cooling cycles.

figure 3a is omitted (as it most probably does not reflect the trend of a single phase) one would expect an increase in conductivity in connection with the lattice expansion in the c direction. This is, however, not found to be the case here and strongly suggests that a part of the Li^+ conduction might occur along the defects, e.g. grain boundaries or dislocations. The exact Li^+ conduction mechanism in the $(1-x)\text{LiBH}_4+x\text{LiI}$ solid solution is, however, currently under investigation.

Figure 7 shows the conductivity of the sample with 50% LiI content measured during five consecutive heating and cooling cycles. As shown for the sample with 50% LiI content in figure 6, the conductivity during the cooling is lower than that during the heating. However, during the next four temperature cycles, the conductivity performance is very stable and reproducible, confirming the good thermal stability of the HT phase of the solid solution. As explained in section III, this sample was prepared and measured using different ball milling conditions and a different impedance spectroscopy experimental setup than the other samples used in this work. Because the density of defects and particle size are important parameters for the conductivity of the samples, it was to be expected that the conductivity values from this measurement could differ from those presented in figures 5 and 6. This explains why the conductivity of the sample in figure 7 is higher at 50°C than shown for the sample with 50% LiI content in figure 6. This also gives an indication of how reproducible the conductivity results are between different laboratory equipment.

E. Differential scanning calorimetry

Figure 8 shows the results of the DSC measurements. Some of the DSC spectra show two maxima of different intensity, most probably due to microstructural inhomogeneity in the samples. In these cases, the phase transition temperature is taken to be that at which the greater maximum is located.

In figure 9, the phase transition temperature between the HT and the LT phase of the $\text{LiBH}_4\text{-LiI}$ system is shown as a function of LiI content. For the measured LiI content there is a clear linear dependency, with the transition temperature decreasing by approximately 70°C for every 10% of LiI addition. For all measured mixtures with a LiI content equal to or above 12.5%, the transition temperature lies below room temperature.

In figure 10, the calculated energy differences $\Delta E(x)$ between the HT and LT phases (shown in fig. 1) are plotted against the transition temperatures measured using DSC. Here x denotes the LiI content of the samples. At each phase transition temperature the Gibbs free energy difference between the two phases is zero. Since contributions from the zero point energy difference and the volume change between the two phases are small, we set $\Delta H(x) \approx \Delta E(x)$, where $\Delta H(x)$ is the enthalpy change for a given ratio of iodine x . Therefore we can write

$$\Delta E(x) = T\Delta S(x). \quad (3)$$

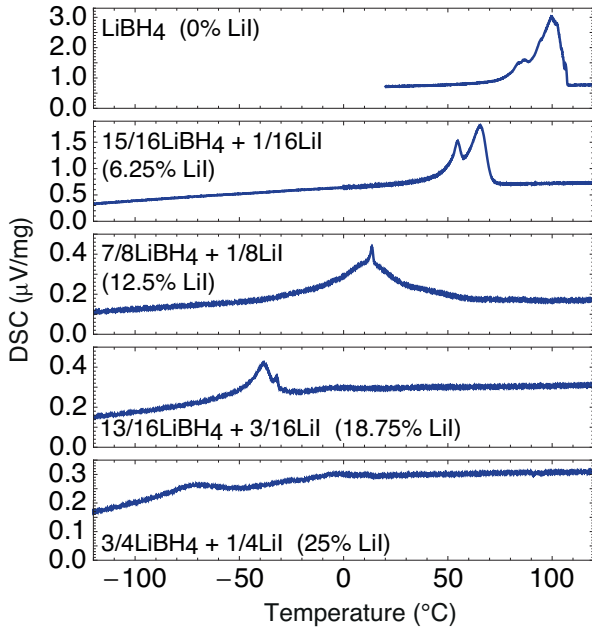


Figure 8 DSC results for different mixing ratios of $(1-x)\text{LiBH}_4+x\text{LiI}$, obtained during cooling.

As a result, the slopes of the lines in figure 10 represent the entropy difference $\Delta S(x)$ between the two phases.

For the iodine free system, we get an entropy difference between the two phases of $\Delta S(0) = 34.7 \text{ J/molK}$. If the addition of iodine was purely an enthalpy effect, $\Delta S(x)$ should remain constant for the different contents of iodine and all data points should fall on the dashed line in figure 10. It is apparent that the entropic difference $\Delta S(x)$ is reduced with addition of iodine by roughly 0.5 J/molK per

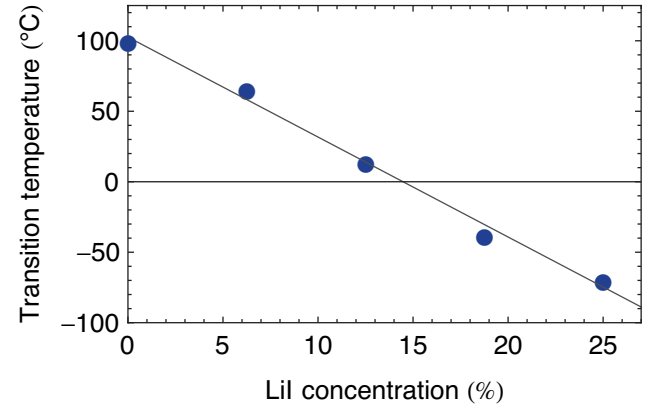


Figure 9 The phase transition temperatures between the hexagonal HT phase and the orthorhombic LT phase in the $(1-x)\text{LiBH}_4+x\text{LiI}$ solid solution as a function of LiI content. For all measured mixtures with $x \geq 1/8$, the transition temperature lies below room temperature.

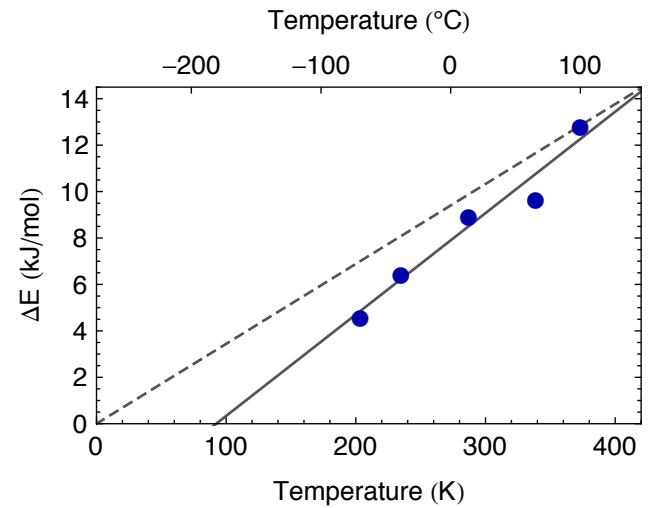


Figure 10 The calculated ground state energy difference between the HT and the LT structures, $\Delta E(x)$, for different iodine contents x as a function of the measured phase transition temperature. The slopes of the lines in the figure represent the entropy change $\Delta S(x)$ between the two phases. The dashed line shows the limit of $\Delta S(x) = 0$.

percentage point of increased iodine content in the system, but it is not possible to quantify how much should be attributed to the changes in the LT or HT respectively, resulting from e.g. changes in directional bonding or configurational entropy.

The calculated value of $\Delta E(0) = 12.8 \text{ kJ/molK}$ is also significantly higher than the published enthalpy values from Kharbachi et al.⁴⁰ ($\Delta H_{\text{Kharbachi}} = 5.1 \text{ kJ/molK}$) and Gorbunov et al.⁴¹ ($\Delta H_{\text{Gorbunov}} = 6.2 \text{ kJ/molK}$). This overestimate of the ground state energy difference also leads to an overestimate of the entropy difference between the two phases. Our calculated value is $\Delta S(0) = 34.4 \text{ J/molK}$ compared to the published values from Pistorius et al.⁴² ($\Delta S_{\text{Pistorius}} = 16.5 \text{ J/molK}$) and from Kharbachi et al.⁴⁰ ($\Delta S_{\text{Kharbachi}} = 13.1 \text{ J/molK}$). Assuming that $\Delta E(x)$ is similarly overestimated, $\Delta S(x)$ should probably be scaled down by a factor of 2.0-2.5 and have a value close to 0.2 J/molK . Although $\Delta S(x)$ varies with iodine content, the governing factor comes from the change in the ground state energy difference $\Delta E(x)$, which can be used as a predictor for the change in stability between the two phases.

V. SUMMARY AND OUTLOOK

The LiI content and the phase transition temperature between the HT and the LT phase are linearly dependent up to at least 25% LiI content as measured using DSC. A decrease in the transition temperature by 70°C for every 10% of LiI addition was found. DFT calculations also show that there is a close to linear stabilization of the HT structure with LiI addition up to a LiI content of 25%. For all samples with a LiI content equal to or greater than 12.5%, the phase transition temperature lies below room temperature and after ball milling the samples only contain the HT phase as observed using XRD.

The $(1-x)\text{LiBH}_4+x\text{LiI}$ solid solutions show a high Li^+ conductivity. At 30°C the conductivity exceeds 10^{-4} S/cm (for the sample with 40% LiI content) and at 140°C it exceeds 10^{-2} S/cm (for the sample with 18.75% LiI content) as measured using impedance spectroscopy. Which mixing ratio of $(1-x)\text{LiBH}_4+x\text{LiI}$ yields optimal conductivity depends greatly on which temperature range is in question. The conductivity is equal or higher during heating than during cooling, with the least difference between heating and cooling results for a LiI content between 18% and 30%.

Non-annealed samples with a low LiI content have apparent densities of defects greater than those with a high LiI content, as revealed by analyzing the FWHM of the reflections in the XRD data. This

could be an artifact due to the presence of inhomogeneities and/or intermediate phases with similar but different cell parameters. After annealing, the density of defects appear to be almost the same for all samples, but the crystallite sizes grow with increasing LiI content. This could explain why samples with low LiI content tend to have a higher conductivity at high temperature than the samples with low LiI content, emphasizing the importance of the grain boundaries for the conduction mechanism.

The least change between the non-annealed and annealed samples is observed for a LiI content of around 30%. By combining information obtained from XRD and from impedance spectroscopy, it is found that samples with defect-rich microstructure, most probably dislocations and/or grain boundary defects, yield higher conductivity values than those in which the defects have been mended by heat treatment and where only intrinsic point defects might exist. This shows that microstructure and heat treatment are important for the conductivity of the samples. Finally, it is found that the expansion of the lattice parameter c is not a predominant parameter for increased conductivity.

The Li^+ conductivity must be high if the $(1-x)\text{LiBH}_4+x\text{LiI}$ solid solution should be used as an electrolyte in a working battery cell. However, the performance of the electrolyte must also remain stable during the lifetime of the battery. In this work, a LiI content around 30% yields the optimal combined room temperature performance in terms of microstructural stability under heat treatment and in terms of high Li^+ conductivity. Impedance spectroscopy measurements during five temperature cycles show that the conductivity of the material is stable and reproducible. Working battery cells using this system as an electrolyte are, however, still to be tested and characterized, and the exact Li^+ conduction mechanism must still be determined.

ACKNOWLEDGEMENTS

The authors would like to acknowledge support from the Copenhagen Graduate School for Nano Science and Technology, COST Action MP1103 “Nanostructured materials for solid-state hydrogen storage”, the Danish Center for Scientific Computing (DCSC), the Center of Atomic-Scale Materials Design (CAMD) and the Energy Research Fund of Landsvirkjun, Iceland.

REFERENCES

- ¹ P. Knauth, Solid State Ionics **180**, 911–916 (2009).

- ² J.B. Goodenough and Y. Kim, *Chem. Mater.* **22**, 587–603 (2010).
- ³ J.-M. Tarascon and M. Armand, *Nature* **414**, 359–67 (2001).
- ⁴ J.-M. Tarascon, *Phil. Trans. R. Soc. A* **368**, 3227–41 (2010).
- ⁵ A. Rabenau, *Solid State Ionics* **6**, 277–293 (1982).
- ⁶ A.G. Belous, G.N. Novitskaya, S.V. Polyanetskaya, and Y.I. Gornikov, *Izv. Akad. Nauk SSSR* **23**, 470–472 (1987).
- ⁷ Y. Inaguma, C. Liqun, M. Itoh, T. Nakamura, T. Uchida, H. Ikuta, and M. Wakihara, *Solid State Commun.* **86**, 689–693 (1993).
- ⁸ O. Bohnke, *Solid State Ionics* **179**, 9–15 (2008).
- ⁹ H. Aono, E. Sugimoto, Y. Sadaoka, N. Imanaka, and G. Adachi, *Solid State Ionics* **47**, 257–264 (1991).
- ¹⁰ K. Arbi, J.M. Rojo, and J. Sanz, *J. Eur. Ceram. Soc.* **27**, 4215–4218 (2007).
- ¹¹ P.G. Bruce and A.R. West, *J. Electrochem. Soc.* **130**, 662–669 (1983).
- ¹² N. Kamaya, K. Homma, Y. Yamakawa, M. Hirayama, R. Kanno, M. Yonemura, T. Kamiyama, Y. Kato, S. Hama, K. Kawamoto, and A. Mitsui, *Nature Materials* **10**, 682–686 (2011).
- ¹³ S. Stramare, V. Thangadurai, and W. Weppner, *Chem. Mater.* **15**, 3974–3990 (2003).
- ¹⁴ A.D. Robertson, A.R. West, and A.G. Ritchie, *Solid State Ionics* **104**, 1–11 (1997).
- ¹⁵ A. Züttel, S. Rentsch, P. Fischer, P. Wenger, P. Sudan, P. Mauron, and C. Emmenegger, *J. Alloys Comp.* **356-357**, 515–520 (2003).
- ¹⁶ Z. Łodziana and T. Vegge, *Phys. Rev. Lett.* **93**, 145501 (2004).
- ¹⁷ J.K. Kang, S.Y. Kim, Y.S. Han, R.P. Muller, and W. a. Goddard, *Appl. Phys. Lett.* **87**, 111904 (2005).
- ¹⁸ Z. Łodziana and T. Vegge, *Phys. Rev. Lett.* **97**, 119602 (2006).
- ¹⁹ L. Mosegaard, B. Møller, J.-E. Jørgensen, U. Bösenberg, M. Dornheim, J.C. Hanson, Y. Cerenius, G. Walker, H.J. Jakobsen, F. Besenbacher, and T.R. Jensen, *J. Alloys Comp.* **446-447**, 301–305 (2007).
- ²⁰ D. Blanchard, Q. Shi, C.B. Boothroyd, and T. Vegge, *J. Phys. Chem. C* **113**, 14059–14066 (2009).
- ²¹ M. Matsuo, Y. Nakamori, S. Orimo, H. Maekawa, and H. Takamura, *Appl. Phys. Lett.* **91**, 224103 (2007).
- ²² V. Epp and M. Wilkening, *Phys. Rev. B* **82**, 020301 (2010).
- ²³ T. Ikeshoji, E. Tsuchida, T. Morishita, K. Ikeda, M. Matsuo, Y. Kawazoe, and S. Orimo, *Phys. Rev. B* **83**, 144301 (2011).
- ²⁴ J.-P. Soulié, G. Renaudin, R. Černý, and Y. K., *J. Alloys Comp.* **346**, 200–205 (2002).
- ²⁵ H. Maekawa, M. Matsuo, H. Takamura, M. Ando, Y. Noda, T. Karahashi, and S. Orimo, *J. Am. Chem. Soc.* **131**, 894–895 (2009).
- ²⁶ D. Fischer, A. Müller, and M. Jansen, *Z. Anorg. Allg. Chem.* **630**, 2697–2700 (2004).
- ²⁷ H. Oguchi, M. Matsuo, J.S. Hummelshøj, T. Vegge, J.K. Nørskov, T. Sato, Y. Miura, H. Takamura, H. Maekawa, and S. Orimo, *Appl.* **94**, 141912 (2009).
- ²⁸ R. Miyazaki, T. Karahashi, N. Kumatani, Y. Noda, M. Ando, H. Takamura, M. Matsuo, S. Orimo, and H. Maekawa, *Solid State Ionics* **192**, 143–147 (2011).
- ²⁹ L.H. Rude, E. Groppo, L.M. Arnbjerg, D.B. Ravnsbæk, R. a. Malmkjær, Y. Filinchuk, M. Baricco, F. Besenbacher, and T.R. Jensen, *J. Alloys Comp.* **509**, 8299–8305 (2011).
- ³⁰ G. Kresse and J. Furthmüller, *Phys. Rev. B* **54**, 11169 (1996).
- ³¹ J.J. Perdew, K. Burke, and M. Ernzerhof, *Phys. Rev. Lett.* **77**, 3865 (1996).
- ³² P.E. Blöchl, *Phys. Rev. B* **50**, 17953 (1994).
- ³³ P.E. Blöchl, C.J. Först, and J. Schimpl, *Bull. Mater. Sci.* **26**, 33 (2003).
- ³⁴ S.R. Bahn and K.W. Jacobsen, *Comp. Sci. Eng.* **56**, 4 (2002).
- ³⁵ M. Wojdyr, *J. Appl. Cryst.* **43**, 1126–1128 (2010).
- ³⁶ A.L. Patterson, *Phys. Rev.* **56**, 978–982 (1939).
- ³⁷ A.R. Stokes and A.J.C. Wilson, *P. Phys. Soc.* **56**, 174–181 (1944).
- ³⁸ N.M. Beekmans and L. Heyne, *Electrochim. Acta* **21**, 303–310 (1976).
- ³⁹ S.M. Haile, D.L. West, and J. Campbell, *J. Mat. Res.* **13**, 1576–1595 (2011).
- ⁴⁰ A. El Kharbachi, I. Nuta, F. Hodaj, and M. Baricco, *Thermochimica Acta* **520**, 75–79 (2011).
- ⁴¹ V.E. Gorbunov, K.S. Gavrichev, V.L. Zalukaev, G.A. Sharpataya, and M.S.I. Baku, *Zh. Neorg. Khim.* **29**, 2333–2337 (1984).
- ⁴² C.W.F.T. Pistorius, *Z. Phys. Chem.* **88**, 253–263 (1974).

Li-ion conduction in the $\text{LiBH}_4\text{:LiI}$ system from Density Functional Theory calculations and Quasi- Elastic Neutron Scattering

*Jón Steinar Garðarsson Myrdal^{1,2}, Didier Blanchard¹, Daði Þorsteinn Sveinbjörnsson¹, Tejs
Vegge^{1, a}.*

¹Department of Energy Conversion and Storage, Technical University of Denmark,
Frederiksborgvej 399 Building 238, DK-4000 Roskilde, Denmark.

²Center for Atomic-scale Materials Design and Department of Physics, Technical University
of Denmark, DK-2800 Lyngby, Denmark

^a Corresponding author. E-mail: teve@dtu.dk

KEYWORDS

Batteries, solid electrolytes, superionic conductivity, density functional theory, quasi-elastic
neutron scattering.

ABSTRACT

The hexagonal high temperature polymorph of LiBH_4 is stabilized by solid solution with LiI to exhibit superionic Li^+ ionic conductivity at room temperature. Herein, the mechanisms for the Li^+ diffusion are for the first time investigated by Density Functional Theory calculations (DFT) coupled with Quasi-elastic Neutron Scattering (QENS) measurements with and without an applied bias potential of 3 V. DFT calculations show that lithium defects such as Frenkel pairs are easily formed at room temperature (formations energies of 0.44 eV) and low energy barriers (0.2 to 0.3 eV) are found between stable defect sites giving rise to high defect mobility. QENS results at 380 K show long range diffusion of Li^+ , with jump lengths of one unit cell and jump rates in agreement with those obtained from DFT. The application of the bias potential increases the diffusion constant by a factor of two. At lower temperatures (300 K), the QENS data reveals jump events of short lengths ($\sim 2 \text{ \AA}$), which could correspond to a jump-recombination process of Li^+ interstitials to an intermediate lattice site, in agreement with DFT calculations.

Introduction

Consumer demands for better reliability, longer lifetime and sustainability is fueling the need for advanced energy storage technologies in a broad range of applications. Today, the battery market is driven by consumer electronics and dominated by Li-ion batteries [1], but since their commercialization in 1991 [2,3] only small improvements have been made [1,4] and new developments are needed to reduce battery prices, improve the reliability, safety and energy/power density. The typical limitations of the lithium-ion batteries are well known: the liquid electrolytes are flammable, the cathodes tend to dissolve, reducing the overall efficiency of the batteries and short circuits between the electrodes might occur due to lithium dendrite formation over cycling. Solid-state electrolytes with sufficient chemical and electrochemical stability could offer better safety and enhanced cycle life, but finding suitable materials with sufficiently high lithium ion conduction and negligible electronic conduction remains a challenge [5].

Lithium borohydride, LiBH_4 , could offer a possible solution and represent a promising class of solid, crystalline materials with superionic Li^+ conduction. At room temperature, LiBH_4 has a slow Li^+ conducting orthorhombic *Pnma* structure (approx. 10^{-8} S/cm at 30°C), but at around 110°C it undergoes a reversible structural transition to a highly Li^+ conducting hexagonal phase [6] (approx. 10^{-3} S/cm at 120°C) generally ascribed to *P6₃mc*. In the following, these polymorphs will be referred to as the LT phase (orthorhombic) and HT phase (hexagonal), respectively. The HT polymorph can be stabilized at room temperature with solid solution of lithium halides (e.g. LiI , LiBr , LiCl) in the borohydride, and the LiI solid solution giving the best conductivities of the Li^+ ions [7,8]. We have recently shown, that an optimal conductivity is reached near the $\text{Li}(\text{BH}_4)_{0.8}\text{I}_{0.2}$ mixture [9].

The mechanisms of the superionic conduction in the HT phase of LiBH_4 have previously been investigated with molecular dynamics by Ikeshoji *et al.* [10] and Aeberhard *et al.* [11] In their publications, they report a double splitting in the Li^+ lattice sites along the c axis and the existence of metastable Li^+ interstitial sites playing large role in the high ionic conductivity.

Here, we report for the first time combined results from density functional calculations (DFT) and quasi-elastic neutron scattering (QENS) measurements [12–14] performed to study the fast Li^+ conduction in the HT polymorph of the $\text{Li}(\text{BH}_4)_{0.75}\text{I}_{0.25}$ system as a function of temperature and applied bias potential.

Computational details

All calculations presented here were prepared and executed using the Atomic Simulation Environment (ASE). [12] Density functional theory calculations (DFT) [13,14] are performed with the real space grid code GPAW [18,19]. GPAW uses the projector-augmented wave method [20] with a frozen core approximation. We used the PBE exchange and correlation functional [21], a $4 \times 4 \times 4$ Monkhorst-Pack k-point mesh and a grid spacing of 0.15 Å. For ground state energy calculations, the atomic positions were relaxed until all atomic forces were < 0.01 eV/Å. The formations of Li^+ interstitials, Li^+_{int} , and vacancies, V_{Li} , have been studied by addition (removal) of Li plus a hole (electron) to the supercell made of $2 \times 2 \times 1$ lattice units (i.e. 8 f.u.), see Figure 1. The supercell was kept neutral by adding a compensating, uniform background charge.

Transition barriers were identified using the nudged elastic band method (NEB) [22,23], a method to find minimum energy paths between two (local) minima. The Climbing Image method [24] was used to find the highest energy point along the ridge, i.e. the transition state. Reaction rates were evaluated using harmonic transitional state theory (HTST) [25]. In the harmonic approximation, the prefactor is given as the ratio between the products of vibrational

frequencies of the initial state and the vibrational frequencies of transition state, TS [22]. This gives us the reaction rate as:

$$k^{HTST} = \frac{\prod_i v_i^{IS}}{\prod_i v_i^{TS}} e^{-\frac{E_{TS}}{k_B T}} \quad (1)$$

The vibrational frequencies of both initial and transition states are calculated using a finite-difference approximation with displacements of 0.01 Å.

The structure of the high temperature polymorph of LiBH₄ remains an open question due to the complex role of dynamical disorder in the system [11,26–28]. The presented calculations were performed on a system of Li(BH₄)_{0.75}I_{0.25}, with an atomic configuration based on the hexagonal LiBH₄ HT structure proposed by Filinchuk *et al.* [28]. Our reference system is composed of 2x2x1 lattice units (8 f.u.), see Figure 1, where every fourth BH₄[−] group has been substituted for I[−] and the cell parameters and atomic configuration relaxed. The relaxed lattice unit lengths are $a = 4.31$ Å, $b = 4.19$ Å and $c = 6.95$ Å. In the case of Frenkel pair formation the super cell was extended to 4x2x1 lattice units.

Experimental

⁷Li¹¹BH₄ (purity > 94%), ⁷Li¹¹BD₄ (purity > 94%) and ⁷LiI (purity > 98%) were purchased from Katchem Ltd. ⁷Li, ¹¹B, and D isotope enriched compounds were used to avoid the high neutron absorption by natural B and Li and the high incoherent cross section of H that would screen the quasi-elastic signal from ⁷Li. The hydrogenated compound is used as a benchmark for the BH₄[−] and H dynamics in order to separate the signal from the dynamics of the proton and other dynamics, e.g. the lithium ion diffusion. The ³⁷Li¹¹BH₄+⁷LiI and ³⁷Li¹¹BD₄+⁷LiI solid solutions were obtained by mechanical milling 2g of the precursors in a stainless steel vial, inner volume 250 ml and rotating speed 650 rpm, for 2 hours. 25 tungsten carbide balls were used giving a powder to ball ratio of 1/100. The crystal structure of the obtained solid solution was

confirmed by X-ray diffraction to be the HT hexagonal phase (space group $P6_3mc$). The transition temperature, from the LT to the HT was determined by differential scanning calorimetry to be of 200 K [9].

The QENS measurements were performed at IN10, the backscattering spectrometer located at the Institut Laue-Langevin, Grenoble, France. 0.5 to 1g of sample were loaded in a specially designed aluminum flat cell of dimensions 30x40x0.5 mm³. The two sides of the cell, separated by a Teflon flange, used as sealing and electrical insulator, were connected to a potentiostat combining *in situ* impedance measurements as well as the application of a potential to the solid electrolyte during the QENS spectra acquisition. The Al container was oriented at 135 degrees with respect to the direct beam. Si(111) monochromator and analyzer crystals were used in a backscattering geometry giving a final neutron wavelength of 6.271 Å and an energy resolution of 1 µeV with an energy transfer range selected between ± 13.5 µeV. The spectra were recorded by seven detectors corresponding to a scattering vector ranging from 0.50 to 1.96 Å⁻¹. The spectra were analyzed by using the curve fitting utility (PAN) included in the DAVE package [29].

Results and Discussions

Density Functional Theory

To study the origin and the mechanisms for the Li⁺ conduction, DFT calculations were performed on lithium interstitials and vacancies in the Li(BH₄)_{0.75}I_{0.25} solid solution. The model structure used in the calculations includes different local environments to mimic the different configurations that can exist in the solid solution. These different local environments include iodine rich areas close to neighboring I⁻ ions, iodine sparse areas in every other crystal plane that does not include any I⁻ ions and areas with moderate iodine concentration between neighboring

BH_4^- and I^- ions, see Figure 1. The relationships between the local iodine concentration and the stability of defect sites and the diffusion barriers between these sites were investigated.

In the HT hexagonal crystal structure, triangular areas exist between all groups of three neighboring Li^+ ions. Each Li^+ ion has an anion neighbor placed directly below it, about 2.5 Å for the pure BH_4^- layers and about 2.9 Å for the layers that include I^- . Together these neighboring an- and cations form a triangular prism. The crystal layers then have a ABAB stacking, which means that centered above (about 0.8 Å) every other triangular prism there is an anion from the next layer (see Figures 1-3).

We performed calculations on Li_{int}^+ interstitials placed inside previously explained triangular prism structures with 4 different local environments (three of which can be seen in Figure 3) and will refer to the calculated sites as 1/3, 2/3, 3/3 and 1/3*, respectively. The labeling refers to the ratio of surrounding BH_4^- ions in the prism grid. The first three sites do not have ions from the neighboring crystal planes positioned directly above or below the site, while the 1/3* site is centered between ions from neighboring layers. In the three “non-sandwiched” sites, the Li_{int}^+ can be found about 0.8-1.1 Å above (depending on the ratio of I^- neighbors) the central position between the three neighboring anions in the hexagonal plane. In the 1/3* site, the Li_{int}^+ is located significantly closer to the two neighboring I^- ions than the in plane BH_4^- ion.

The 1/3 site is energetically most favorable, while the 3/3 and the 2/3 sites are almost equal in energy being 0.14 eV and 0.15 eV, respectively, less favorable than the 1/3 site. The 1/3* site is the least favorable, 0.18 eV less favorable than the 1/3 site.

Calculations were performed on V_{Li}^- vacancies in two different local environments, i.e. with a neighboring I^- ion (an iodine site) and a second site without iodine neighbors (a BH_4^- site). The BH_4^- site is more favorable than the I^- site, but the energy difference is small, 0.05 eV.

A Frenkel pair is created when a lattice Li^+ ion is moved into an interstitial site thereby creating a vacancy and interstitial defect pair. A calculation on a Frenkel pair, where the interstitial is sitting in a 1/3 site, was performed giving a formation energy for the defect pair as $E_{\text{Frenkel}} = 0.44$ eV. Figure 2 shows the minimum energy path from a NEB calculation for the formation of the Frenkel pair, starting from the defect free system. The transition barrier to form the defect is $E_{\text{Frenkel_TS}} = 0.47$ eV meaning that there is a very small threshold for the interstitial to recombine with the vacancy, unless the charged defects become further separated e.g. by an applied bias (see supplementary movie).

We have performed NEB calculations on different possible diffusion mechanisms for individual Li^+ interstitials (Li_{int}^+) and vacancies (V_{Li}) originating from the electrodes; all transition state energies and jump lengths are presented in Table 1.

Li_{int}^+ conduction mechanisms were calculated from a 1/3 site to the four different sites. An interstitial jump from a 1/3 site to an identical 1/3 site, one lattice unit away, has a transition barrier of $E_{1/3-1/3_TS} = 0.26$ eV. During the jump, a clear shift of a neighboring lattice Li^+ ion is visible along the c-axis of about 0.6 Å to make room for the diffusing interstitial. Similarly, a rotational motion of neighboring BH_4^- ions, around the c-axis and in the direction following the moving interstitial is visible. It was also investigated whether the diffusion between 1/3 sites could take place through an exchange mechanism, where a lattice ion moves from its lattice site to a 1/3 interstitial site, while the interstitial ion moves into the lattice site. This exchange mechanism is possible, but significantly more expensive than the single particle jump, with a transition barrier of $E_{\text{exchange_TS}} = 0.44$ eV. The exchange gives two different jump lengths, 3.00 Å for the lattice ion moving to the interstitial site and 4.07 Å for the interstitial ion moving into the lattice site.

An interstitial jump from a 1/3 site to a 2/3 site has a similar barrier as the jump between 1/3 sites with $E_{1/3-2/3_TS} = 0.28$ eV. Since the 2/3 site is less stable than the 1/3 site, the transition barrier for going from 2/3 to 1/3 site is lower with $E_{2/3-1/3_TS} = 0.14$ eV (see Figure 3).

The 1/3* site lies in between the 1/3 and the 2/3 sites and since the transition barrier for going from the 1/3 site to the 1/3* site is only $E_{1/3-1/3^*_TS} = 0.20$ eV, there is a possibility that at lower temperatures the interstitials will equilibrate in the shallow 1/3* site. If the interstitial is then to continue from the 1/3* site to the 2/3 site it has to overcome a second transition barrier of $E_{1/3^*-2/3_TS} = 0.09$ eV. It is however more likely that the interstitial will jump back to the 1/3 site since the 1/3* sites stability towards the 1/3 site is very low ($E_{1/3^*-1/3_TS} = 0.02$ eV).

A jump from a 1/3 site to a 3/3 site is different from the previously addressed jumps since it is a jump between crystal planes, while the others are jumps in the same hexagonal plane. Going from the 1/3 site to the 3/3 site gives $E_{1/3-3/3_TS} = 0.32$ eV while for the opposed direction we get $E_{3/3-1/3_TS} = 0.18$ eV.

V_{Li} vacancy diffusion calculations were performed for a jump between two I^- sites as well as a jump between an I^- site and a BH_4^- site. The transition barrier between the I^- sites is found to be $E_{I-I_TS} = 0.23$ eV, while the barriers for the second mechanism are $E_{I-BH_4_TS} = 0.33$ eV and $E_{BH_4-I} = 0.28$ eV. For both mechanisms the jump lengths are 4.27 Å.

Quasi-elastic neutron scattering

Figure 4 displays the temperature dependence of the normalized elastic intensity, for $3^7Li^{11}BH_4+^7LiI$ and $3^7Li^{11}BD_4+^7LiI$ and the deduced mean square displacement $\langle u^2 \rangle$ for $3^7Li^{11}BH_4+^7LiI$, collected during temperature scans performed from $T = 3$ to 430 K at a heating ramp of 2 K.min⁻¹. For each temperature, the intensity is the summation of the intensities collected on the seven detectors. The plots for the hydrogenated and deuterated samples display

similar trends. The loss of intensity for the hydrogenated sample is of course more important because of the large hydrogen incoherent cross section, but the changes occur at the same temperatures showing that there are no significant shift, detectable with the instrument, in the characteristic times of the observed dynamics because of the isotope exchange. In Figure 4, three different regions can be distinguished with different evolution of $\langle u^2 \rangle$ with T , corresponding to the existence of the two polymorphs (LT structure from 3 K to 180 K, HT structure from 220 to 430 K) and the transition region from ~ 180 to 220K. For the deuterated sample at ~ 350 K, the evolution of the elastic intensity shows deviations when compare to the nearly monotonic decrease of the intensity obtained for the hydrogenated sample in that temperature range, indications of dynamical events not seen in the presence of hydrogen. This first measurement confirmed the two temperature ranges, where the different polymorphs exist, and show the difference between the evolution with temperature of the elastic lines of the hydrogenated and deuterated solid solutions.

QENS spectra were collected at different constant temperatures and were fitted with one or two Lorentzian functions $L(\Gamma, \omega)$, of half width at half maximum (HWHM) Γ , modeling the inelastic signal and a Dirac delta function $\delta(\omega)$, modeling the elastic one. Both functions being convolved with the instrumental resolution function $R(Q, \omega)$ obtained from measurements at 4 K, temperature at which no dynamical motions were observed on the time scale of the instrument. If needed a linear baseline $B(Q)$ was used to model the inelastic background in the quasi-elastic region which originates from processes much faster than those observable within the time scale of the instrument used. Thus the following expression was applied [30]:

$$S_{inc}^{tot}(Q, \omega) = R(Q, \omega) \otimes (A_0(Q)\delta(\omega) + \sum A_i(Q)L(\Gamma_i, \omega)) + B(Q) \quad (2)$$

For the hexagonal $3^7\text{Li}^{11}\text{BH}_4+^7\text{LiI}$, a series of QENS spectra were recorded at constant temperatures, ranging from 4 K to 440 K. At temperatures above ~ 220 K, quasielastic broadenings, emerging from the resolution of the instrument, were observed. One Lorentzian was used to fit the spectra. At 240 and 300 K, for example, with and without the application of a bias potential ($f = 1$ kHz, $U = 3$ V, $I = 0.3$ mA and $f = 1$ kHz, $U = 3$ V, $I = 0.4$ mA, respectively) the widths, Q and potential independent over the measured Q -range, were found to be of ~ 7.44 and ~ 15.0 μeV , respectively. These quasi-elastic lines originate from localized atomic motion [30] and according to previous QENS studies on hexagonal LiBH_4 , correspond to the BH_4^- reorientation mechanisms [31]. A fit of the experimental Elastic Incoherent Structure Factor (A_0 in eq. 1) [30], with the theoretical expression of the “high temperature model”, detailed in [31] confirmed the latter results.

For the hexagonal $3^7\text{Li}^{11}\text{BD}_4+^7\text{LiI}$, QENS spectra were again measured at different constant temperatures from 80 K to 400 K. Below 300 K and above 380 K, no clear quasi-elastic signal were observed. At low temperature (< 300 K) the signal could be of too low intensity or embedded in the elastic line, at high temperature (> 380 K) the signal might be too broad and only present as a flat background. Thus, given the instrumental resolution, the spectra recorded at 300 and 380 K, with and without the application of a potential ($f = 1000$ Hz, $U = 3$ V and $I = 0.4$ mA, and $U = 3$ V and $I = 1$ mA respectively) yielded clear diffusional broadening. Figure 5 presents the spectra, recorded at 300 K with and without the application of the potential. One should note the large effect of the potential, with the large gain in the elastic lines intensities at high Q and shift in the Q -dependence of the line broadening (see Figure 6). No such effect was observed as 380 K. At 300 K, two Lorentzians were used, one having a constant width of 15 μeV for all the detectors to take into account the quasielastic signals from the BD_4^- reorientation. This

line broadening was obtained for the hydrogenated sample at the same temperature and is used assuming, from the elastic temperature scans, that there is no significant differences in the reorientation rates of the hydrogenated and deuterated tetrahedra. At 380 K, a constant flat background was used to take in to account this “fast” motion (compared to the resolution of the instrument) at high temperatures. Henceforth, Q and potential dependent quasielastic broadening were found for the two temperatures. They can be attributed to non-localized dynamics [30] and the HWHM values have been fitted with the Chudley-Elliott model [30] (Figure 6), i.e. the dynamics observed were treated in a first approximation as a random walk diffusive mechanism of a defect in the crystal lattice. In the Chudley-Elliott model the Q -dependence of the HWHM (Γ_D) is given by:

$$\Gamma_D(Q) = \frac{\hbar}{\tau_D} \left(1 - \frac{\sin(QL)}{QL} \right) \quad (3)$$

where L is the effective jump length and τ_D the resident time between two jumps.

At 300 K, when the potential was applied, it is not possible to fit the experimental data satisfactorily with eq. 2. For the broadening obtained when no potential was applied two different fits were performed, one with the two fitting parameters (L and τ_D) set free to vary, yielding a short jump length of $1.7 \pm 0.3 \text{ \AA}$ and one with L fixed to 2.34 \AA , i.e. the value obtained from the DFT calculation for the $1/3$ to $1/3^*$ defect diffusion. As seen in Table 2, the numerical values of τ_D^{-1} and L obtained for the different fits at 300 K ($\tau_D^{-1} \approx 10^9 \text{ s}^{-1}$ and $L \approx 2 \text{ \AA}$) and 380 K ($\tau_D^{-1} \approx 10^{10} \text{ s}^{-1}$ and $L \approx 4 \text{ \AA}$) indicate different mechanisms at the two temperatures. Furthermore, the application of the potential is influencing the observed dynamics (see Table 2).

If the dynamics are diffusion related then the diffusion rates can be calculated from:

$$D = L^2 / (n\tau_D) \quad [30] \quad (4)$$

where $n = 2, 4$ or 6 depending on the dimensionality of the diffusion, respectively $1, 2$ or 3 . The values obtained for D are presented in Table 2. At 300 K , they are lower than those published for the high temperature phase of pure LiBH_4 , at 535 K : 5.82×10^{-6} [11] and $2.28 \times 10^{-6}\text{ cm}^2/\text{s}$ [6] but when translated to 535 K and assuming an Arrhenius temperature dependency, values $>10^{-4}\text{ cm}^2/\text{s}$ are obtained, in agreement with the higher conductivity measured for the solid solution compared to that of the pure compound [9]. At 380 K , the diffusion rates are found to be of the same order of magnitude as the published one even though the temperature is lower. Again this is in agreement with the higher conductivity measured for the solid solution than for the pure compound.

Discussions

The QENS results tell different stories at 300 K and 380 K . At 300 K , the observed diffusion events have shorter jump length than the unit cell. At this temperature, two different Chudley-Elliott least square fits of the quasielastic broadening, obtained when no potential was applied, were performed. One with both parameters free to vary, yielding a jump length of $1.7\text{ Å} \pm 0.3\text{ Å}$ (without an apparent crystallographic equivalent site) and a second with a fixed jump length of 2.34 Å (shortest length obtained by DFT calculation). In both cases diffusion rates of about $1 \times 10^9\text{ s}^{-1}$ were obtained and in good agreement with DFT (Table 1), although the experimental numbers have large uncertainties. Indeed, the experimental data cover only a limited Q range and broadening observed at larger Q values would largely enhance the accuracy of the fitted values for this rather short jump length. With DFT calculations, the only identified mechanisms with short jump lengths (2.34 Å) are the Li^+_{int} jumps between the $1/3$ and $1/3^*$ site, with an energy barrier of 0.20 eV and rates slightly larger than the experimental one: $7.3 \times 10^9\text{ s}^{-1}$. From the shallow $1/3^*$ site, the next available site is then the $2/3$ but at a longer jump distance, 3.3 Å .

Furthermore and as previously discussed, the atom will most probably jump to the $1/3$ site again. Such jumps between two inequivalent sites ($1/3$ and $1/3^*$) would appear in the QENS data as a localized motion and give Q independent quasi-elastic broadenings. It is therefore difficult to pair the experimentally observed short jumps definitely together with those determined from DFT, but due to the short distance, they are expected to originate from such interstitial jumps. Furthermore, it should be noted that the DFT calculations are effectively performed at 0 K and the role of dynamical disorder may be significant at higher temperatures.

The strong effect due to the applied bias potential at 300 K on the observed broadening and intensities of the QENS spectra should also be noted. Due to the limited data available it is unfortunately not possible to quantify this effect, but the application of the potential is expected to increase both the defect concentration and mobility. Under an applied bias, a significant number of additional defects will be created at the electrode interface and the lifetime of the Frenkel pairs will also increase due the charge difference (see below), but further experiments are needed to quantify these effects.

The superionic conductivity in the $\text{Li}(\text{BH}_4)_{(1-x)}\text{I}_x$ must originate from the high mobility of lithium defects in the hexagonal crystal lattice. The DFT calculations show that Frenkel pairs have a low formation energy (0.44 eV) and are thus present in a concentration of $\sim 5 \times 10^{18} \text{ cm}^{-3}$ in a $\text{Li}(\text{BH}_4)_{0.75}\text{I}_{0.25}$ solid solution at room temperature, even without an applied bias. The formation energy of individual interstitials and vacancies is therefore expected to be very low and the solid solution can be classified as Type I ionic conductors, after Rice and Roth classification of ionic solids, [32,33] and for which the conduction mechanism is governed by vacancy migration. The DFT results for the Frenkel defect diffusion are nicely supported by the QENS results obtained at 380 K. Indeed, we observed diffusion motions with jump lengths about

one unit cell and diffusion rates about $8 \times 10^9 \text{ s}^{-1}$, results in adequacy with the calculated direct jumps between the more favorable interstitial and vacancy sites, with comparable jump lengths and rates of $8.3 \times 10^9 \text{ s}^{-1}$ for the direct Li^+_{int} 1/3 to 1/3 site jumps and $9.8 \times 10^8 \text{ s}^{-1}$ for the V^-_{Li} , Γ to BH_4^- migration. As mentioned, the short lifetime of the thermal Frenkel pairs will increase under an applied bias which will drive the oppositely charged Li^+_{int} and V^-_{Li} apart, and the main source of defects in that case will be the electrolyte/electrode interfaces, where Li^+ ions leave and enter the material.

The calculations show that the most favorable mechanisms for the Li^+ conduction are taking place in the hexagonal plane, the jumps with a component in the c direction having higher energy barriers, leading to a two-dimensional conductivity, as previously suggested in [6,11,34]. Thus, the values of D calculated with $n=4$ are the most representative of the mean diffusion constant. One should note here that the D values are almost doubled when a 3V potential was applied.

TABLES:

Table 1: Calculated transition barriers, jump lengths and rates for different diffusion mechanisms in the $\text{Li}(\text{BH}_4)_{0.75}\text{I}_{0.25}$ system. All mechanisms are single particle jumps except for the exchange mechanism. Different transition barriers depending on the direction of the jumps are caused by relative energy differences between different sites.

Defect	Mechanism	Transition Barrier [eV]	Jump length [Å]	Rate 300 K [s ⁻¹]	Rate 380 K [s ⁻¹]
Li ⁺ interstitial					
	1/3 to 1/3 site	0.26	4.32	9.95e+08	8.26e+09
	1/3 to 2/3 site	0.28/0.14	4.31	4.59e+08	4.49e+09
	1/3 to 3/3 site	0.32/0.18	4.36	9.77e+07	1.32e+09
	Exchange 1/3 to 1/3 site	0.44	3.00/4.07	9.41e+05	3.39e+07
	1/3 to 1/3* site	0.20/0.02	2.34	7.29e+09	3.72e+10
	1/3* to 2/3 site	0.09/0.15	3.30	7.70e+12	9.07e+12
Li ⁺ Vacancy					
	I to I site	0.23	4.27	3.17e+09	2.07e+10
	I to BH ₄ ⁻ site	0.33/0.28	4.27	6.63e+07	9.75e+08
Frenkel Pair	Formation	0.46/0.02	3.32	4.35e+05	2.94e+06

Table 2: Values for the jump length (L) and rate (τ_D^{-1}) obtained from the Chuddley–Elliot fit (eq. 2) of the experimental HWHM (Γ) of the QENS spectra plotted versus Q for the $^3\text{Li}^{11}\text{BD}_4+^7\text{LiI}$ solid solution at 300 K and 380 K with or without the application of a potential (3V). Values of the corresponding diffusion rate for the different dimensionality.

Temp. (K)	300		380	
Potential (V)	0	0	0	3 V
L (Å)	1.7 ± 0.3	2.34 (fixed)	3.6 ± 0.3	4.3 ± 0.2
$\tau_D^{-1} \times 10^9$ (s ⁻¹)	1.25 ± 0.16	1 ± 0.2	8.3 ± 0.3	10 ± 0.16
$\mathbf{D} \times 10^{-7}$ (cm ² /s)				
n=2	1.8 ± 0.5	2.7 ± 0.5	54 ± 6	92 ± 6
n=4	0.9 ± 0.3	1.4 ± 0.4	27 ± 3	46 ± 3
n=6	0.6 ± 0.15	0.9 ± 0.2	18 ± 2	31 ± 2

FIGURES:

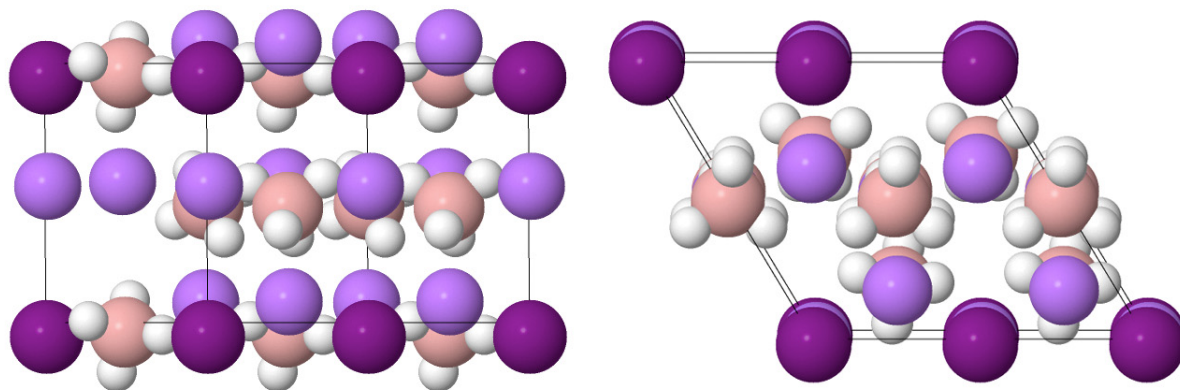


Figure 1. Shows the supercell used in the DFT calculations along with few neighbouring atoms for better visualization of the model structure. The figure displays the difference in local environments, iodine rich areas close to neighbouring I^- ions, iodine sparse areas in iodine free crystal planes and areas with moderate iodine concentration between neighbouring BH_4^- and I^- ions. Li: pale purple, I: dark purple, B: pink and H white.

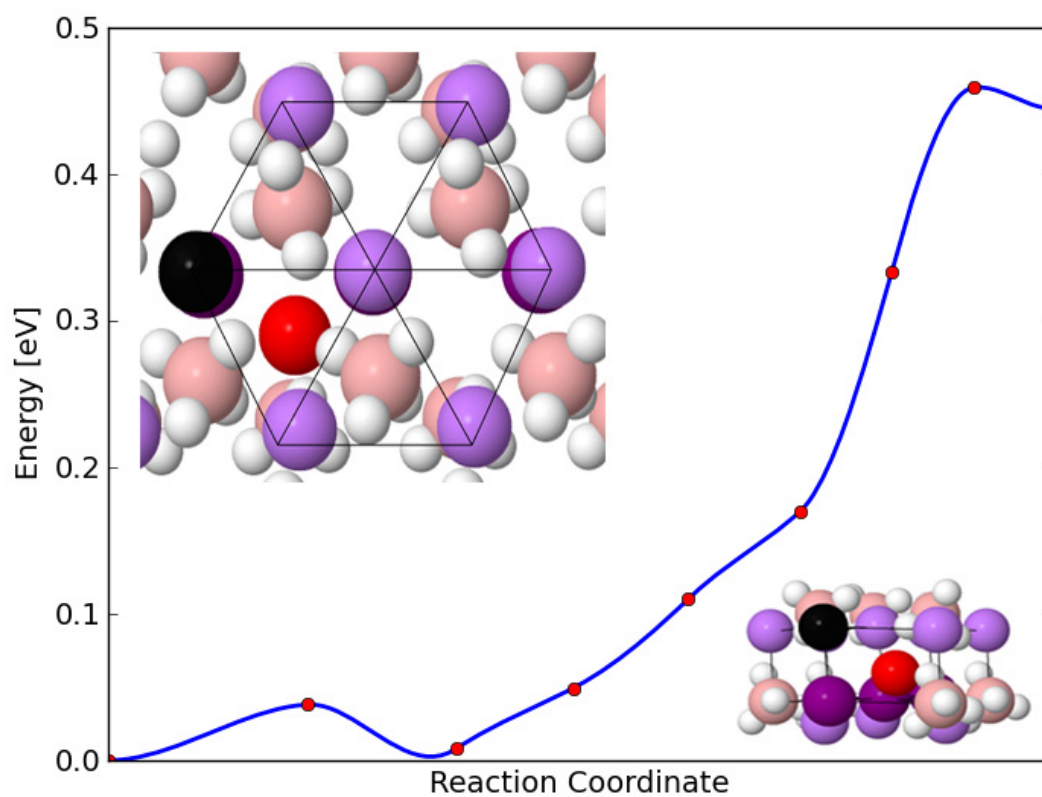


Figure 2. The minimum energy path for formation of a Frenkel defect pair and the corresponding atomic structure. The created Li^+ interstitial, seated in a 1/3 site, and vacancy are shown as red and black spheres respectively. The transition barrier for creating the defect pair is 0.46 eV. The lattice atoms are displayed as follows; Li: pale purple, I: dark purple, B: pink and H: white.

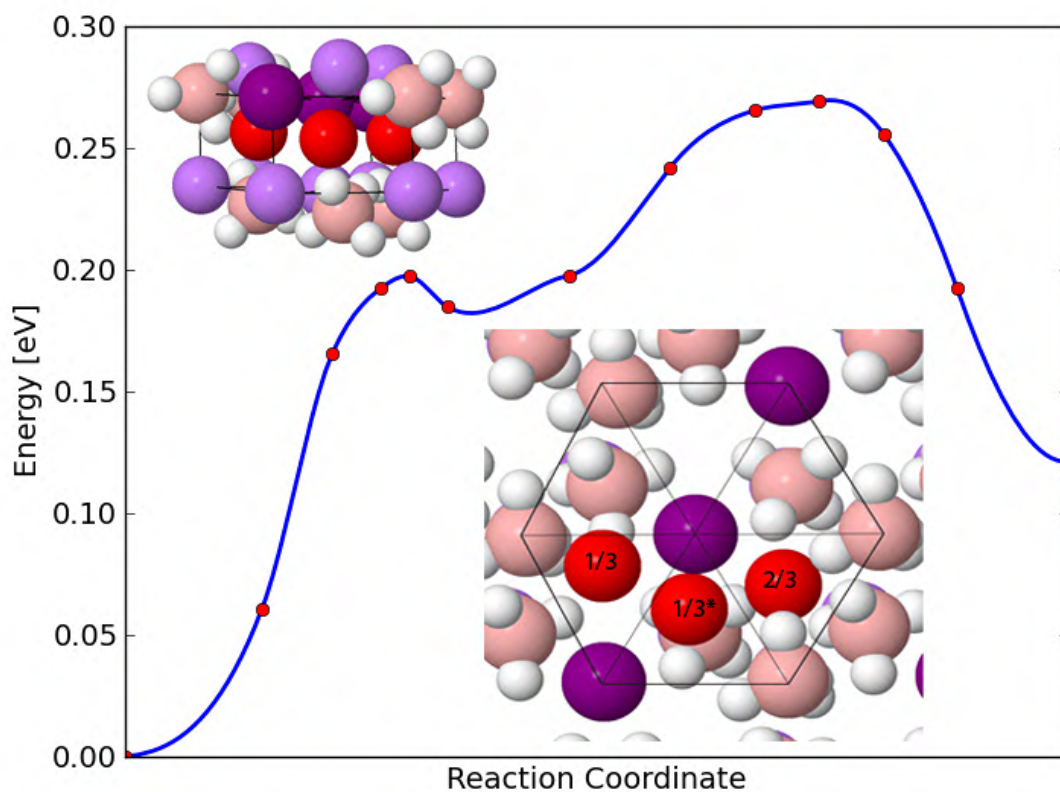


Figure 3. The minimum energy path from a $1/3$ to a $2/3$ interstitial site, passing through a $1/3^*$ interstitial site. The atomic positions of the interstitial in the three different sites are shown from left to right in the same order as the sites occur along the path. The $1/3^*$ site opens up the possibility for interstitials with lower kinetic energy. The lattice atoms are displayed as follows; Li: pale purple, I: dark purple, B: pink and H: white.

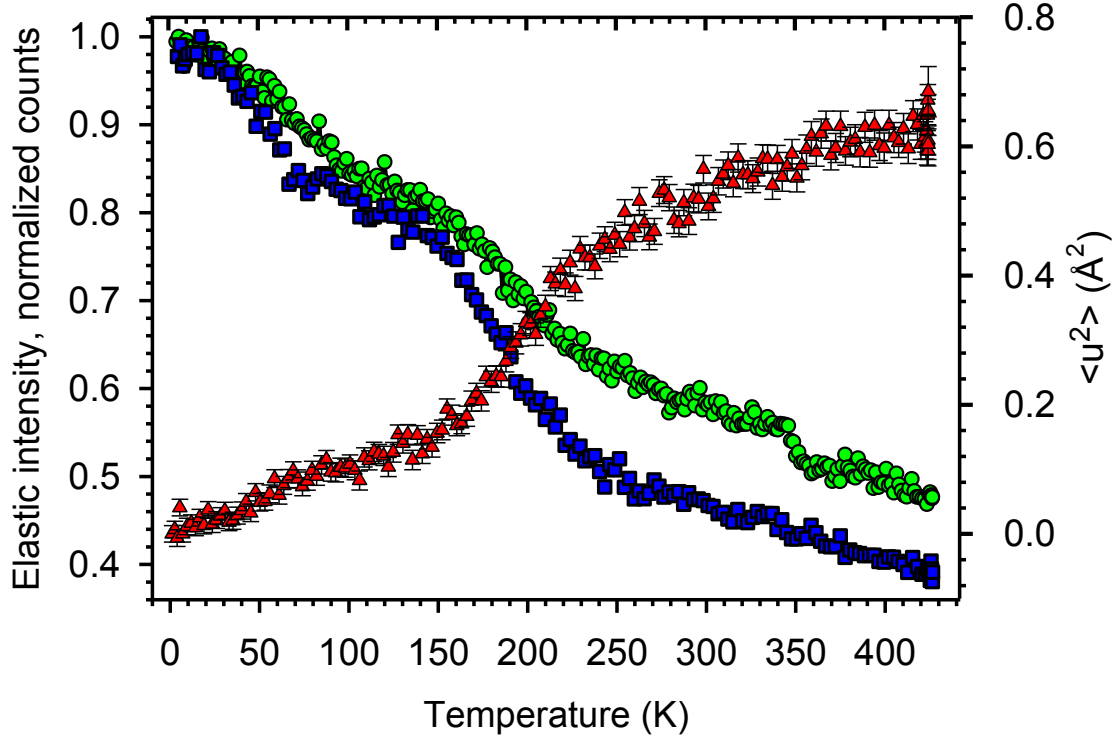


Figure 4. Evolution of the normalized elastic intensities as function of the temperature for $3^7\text{Li}^{11}\text{BD}_4+1^7\text{LiI}$ (green circles) and $3^7\text{Li}^{11}\text{BH}_4+1^7\text{LiI}$ (blue squares), from 3 to 430 K, heating ramp $2\text{K}\cdot\text{min}^{-1}$, measured at IN10 spectrometer. Evolution of the deduced mean square displacement, for $3^7\text{Li}^{11}\text{BH}_4+1^7\text{LiI}$ in the same temperature range (red triangle). $\langle u(T)^2 \rangle$ is obtained from the fit of the elastic intensity with the following expression $I(T) = I(0) \cdot \exp[-Q^2 \cdot \langle u(T)^2 \rangle]$ where Q is taken as the average momentum transfer for the seven detectors.

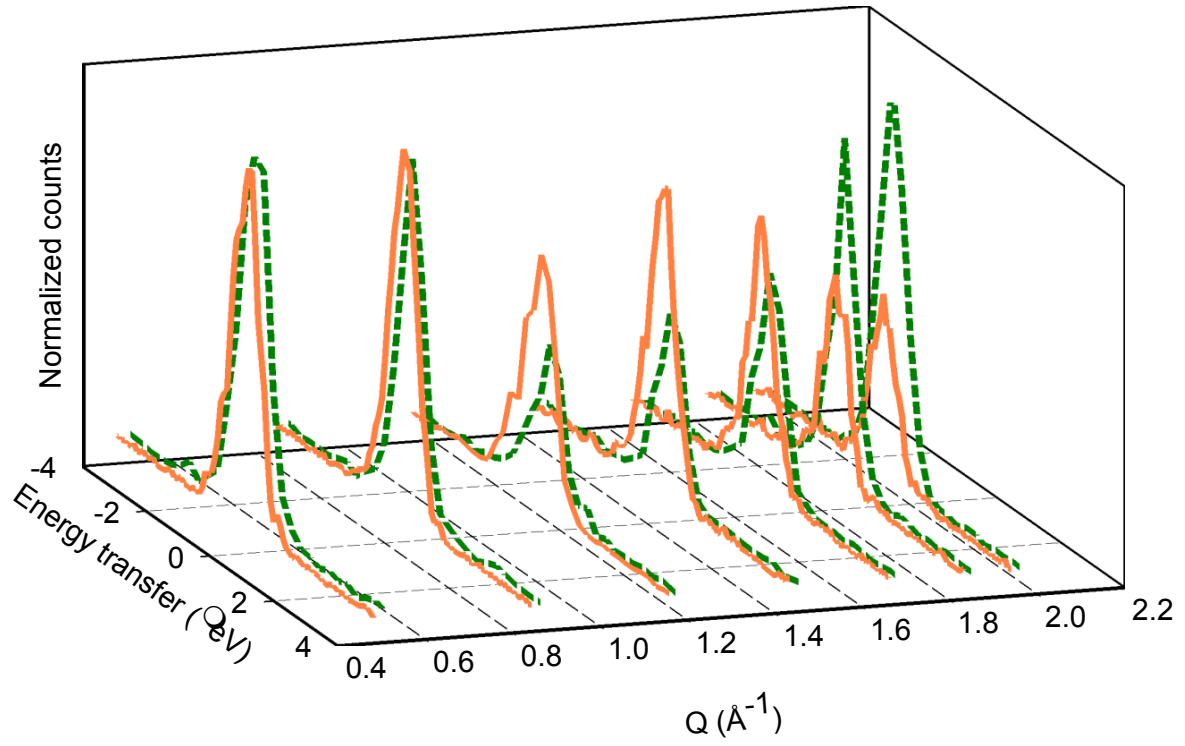


Figure 5. QENS spectra recorded for $3^7\text{Li}^{11}\text{BD}_4+1^7\text{LiI}$, at 300 K, without (orange solid line) and with (green dashed line) the application of a potential ($f = 1$ kHz, $U = 3$ V and $I = 0.4$ mA). Note the pronounced change in the intensity, at high Q , between the two measurements.

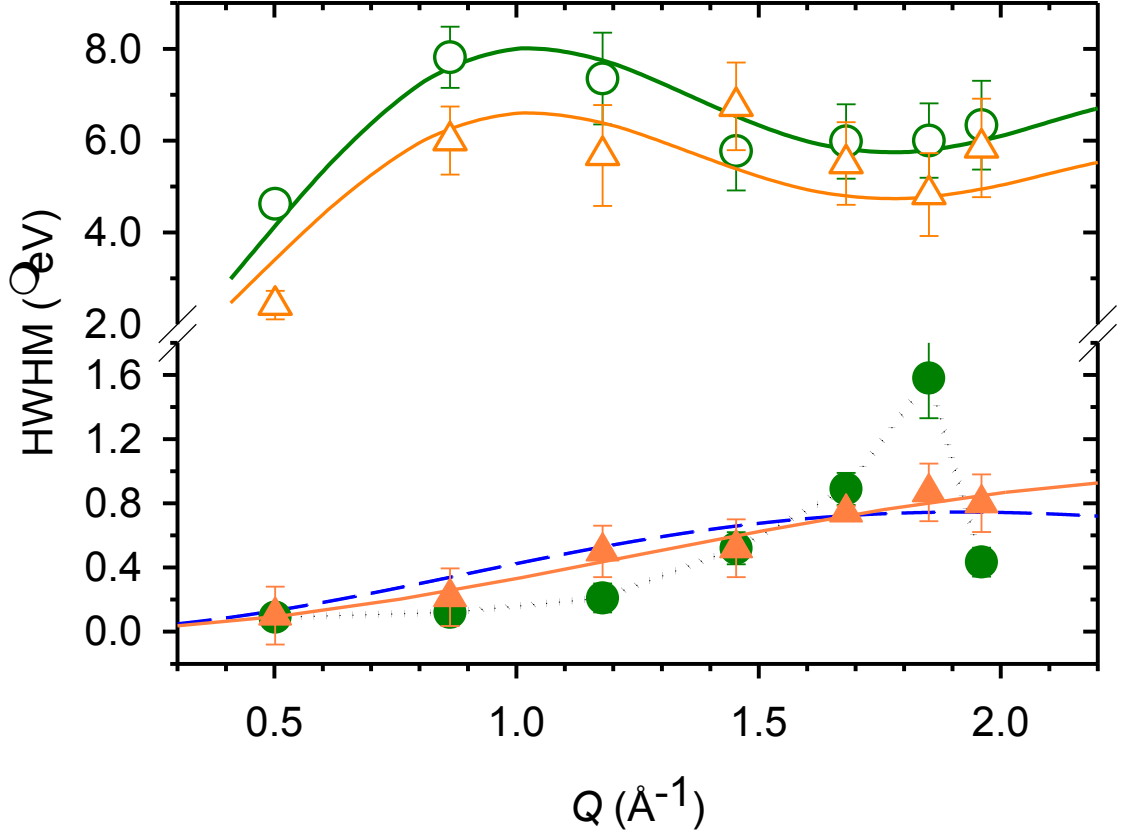


Figure 6. Q and potential dependent Half Width at Half Maximum (HWHM) of the Lorentzian for the non localized dynamics. Upper plots, measurement performed at 380 K. Lower plots, measurements performed at 300K. Filled Circles, measurements performed with potential ($f = 1$ kHz, $U = 3$ V, $I = 0.4$ mA), open circles ($f = 1$ kHz, $U = 3$ V and $I = 1$ mA), triangles without potential. The solid orange lines are the results of the fits with the Chudley-Elliott model (equ. 2) with L and τ_D fitted, the long dashed blue line when only τ_D was set free to vary (L fixed to 2.3 Å), the black broken line is to guide the eye.

References

- [1] A. K. Shukla and T. Prem Kumar, *Current Science* **94**, 314 (2008).
- [2] K. Mizushima, P. C. Jones, P. J. Wiseman, and J. B. Goodenough, *Material Research Bulletin* **15**, 783 (1980).
- [3] M. M. Thackeray, W. I. F. David, P. G. Bruce, and J. B. Goodenough, *Material Research Bulletin* **18**, 461 (1983).
- [4] M. Armand and J. M. Tarascon, *Nature* **451**, 652 (2008).
- [5] J. M. Tarascon, *Phil. Trans. R. Soc.* **368**, 3227-3241 (2010).
- [6] M. Matsuo, Y. Nakamori, S. Orimo, H. Maekawa, and H. Takamura, *Applied Physics Letters* **91**, 224103 (2007).
- [7] H. Maekawa, M. Matsuo, H. Takamura, M. Ando, Y. Noda, T. Karahashi, and S. Orimo, *Journal of the American Chemical Society* **131**, 894 (2009).
- [8] H. Oguchi, M. Matsuo, J. S. Hummelshøj, T. Vegge, J. K. Nørskov, T. Sato, Y. Miura, H. Takamura, H. Maekawa, and S. Orimo, *Applied Physics Letters* **94**, 141912 (2009).
- [9] D. Sveinbjörnsson, J. S. Myrdal, D. Blanchard, T. Hirata, M. B. Mogensen, P. Norby, S. Orimo, and T. Vegge, *Journal of Physical Chemistry C* (2012).
- [10] T. Ikeshoji, E. Tsuchida, T. Morishita, K. Ikeda, M. Matsuo, Y. Kawazoe, and S. Orimo, *Physical Review B* **83**, 1 (2011).
- [11] P. Aeberhard, S. Williams, D. Evans, K. Refson, and W. David, *Physical Review Letters* **108**, 095901 (2012).
- [12] D. Blanchard, J. B. Maronsson, M. D. Riktor, J. Kehres, D. Sveinbjörnsson, E. G. Bardají, A. Léon, F. Juranyi, J. Wuttke, K. Lefmann, B. C. Hauback, M. Fichtner, and T. Vegge, *J. Phys. Chem. C* **116**, 2013 (2012).
- [13] D. Blanchard, M. D. Riktor, J. B. Maronsson, H. S. Jacobsen, J. Kehres, D. Sveinbjörnsson, E. G. Bardají, A. Léon, F. Juranyi, J. Wuttke, B. C. Hauback, M. Fichtner, and T. Vegge, *J. Phys. Chem. C* **114**, 20249 (2010).
- [14] J. Voss, Q. Shi, H. S. Jacobsen, M. Zamponi, K. Lefmann, and T. Vegge, *J. Phys. Chem. B* **111**, 3886 (2007).
- [15] S. Bahn and K. Jacobsen, *Computing in Science & Engineering*, **4**, 56 (2002).

- [16] W. Kohn and L. J. Sham, Physical Review. **140**, A1133 (1965).
- [17] P. Hohenberg and W. Kohn, Physical Review **155**, B864 (1964).
- [18] J. Enkovaara et al., J. Phys.: Condens. Matter **22**, 253202 (2010).
- [19] J. J. Mortensen, L. B. Hansen, and K. W. Jacobsen, Physical Review B, **71**, 035109 (2005).
- [20] P. E. Blöchl, Physical Review **50**, 17953 (1994).
- [21] J. Perdew, K. Burke, and M. Ernzerhof, Physical Review Letters **77**, 3865 (1996).
- [22] G. Henkelman and H. Jónsson, The Journal of Chemical Physics **113**, 9978 (2000).
- [23] H. Jonsson, G. Mills, and K. W. Jacobsen, *Classical and Quantum Dynamics in Condensed Phase Systems* , edited by B. J. Berne, G. Cicotti, and D. F. Coker, World Scientific, (1998).
- [24] G. Henkelman, B. Uberuaga, and H. Jónsson, The Journal of Chemical Physics **113**, 9901 (2000).
- [25] G. Vineyard, Journal of Physics and Chemistry of Solids **3**, 121 (1957).
- [26] Z. Lodziana and T. Vegge, Physical Review Letters **93**, 145501 (2004).
- [27] Z. Lodziana and T. Vegge, Physical Review Letters **97**, 119602 (2006).
- [28] Y. Filinchuk, D. Chernyshov, and R. Cerny, Journal of Physical Chemistry C **112**, 10579 (2008).
- [29] R. T. Azuah, L. R. Kneller, Y. Qiu, C. M. Brown, J. R. D. Copley, and R. M. Dimeo, Journal of Research of the National Institute of Standards and Technology **114**, 341 (2009).
- [30] M. Bée, Chemical Physics **292**, 121-141 (2003).
- [31] N. Verdal, T. J. Udovic, and J. J. Rush, Journal of Physical Chemistry C **116**, 1614 (2012).
- [32] M. J. Rice and W. L. Roth, Journal of Solid State Chemistry **4**, 294 (1972).
- [33] S. Chandra, *SuperIonic Solids* (North-Holland Publishing Company - Amsterdam.New York.Oxford, 1981), p. 1981.
- [34] V. Epp and M. Wilkening, Physical Review B **82**, 4 (2010).



The role of transition metal interfaces on the electronic transport in lithium–air batteries

Jingzhe Chen^a, Jens S. Hummelshøj^b, Kristian S. Thygesen^a, Jon S.G. Myrdal^{a,c},
Jens K. Nørskov^{b,d}, Tejs Vegge^{c,*}

^a Center for Atomic-scale Materials Design and Department of Physics, Technical University of Denmark, DK-2800 Lyngby, Denmark

^b SUNCAT Center for Interface Science and Catalysis, SLAC National Accelerator Laboratory, Menlo Park, CA 94025, USA

^c Materials Research Division, Risø National Laboratory for Sustainable Energy, Technical University of Denmark, DK-4000 Roskilde, Denmark

^d Department of Chemical Engineering, Stanford University, Stanford, CA 94305, USA

ARTICLE INFO

Article history:

Received 30 September 2010

Received in revised form 3 December 2010

Accepted 6 December 2010

Available online 20 January 2011

Keywords:

Lithium–air batteries

Density functional theory

Electronic transport

ABSTRACT

Low electronic conduction is expected to be a main limiting factor in the performance of reversible lithium–air, Li–O₂, batteries. Here, we apply density functional theory and non-equilibrium Green's function calculations to determine the electronic transport through lithium peroxide, Li₂O₂, formed at the cathode during battery discharge. We find the transport to depend on the orientation and lattice matching of the insulator–metal interface in the presence of Au and Pt catalysts. Bulk lithium vacancies are found to be available and mobile under battery charging conditions, and found to pin the Fermi level at the top of the anti bonding peroxide $\pi^*(2p_x)$ and $\pi^*(2p_y)$ levels in the Li₂O₂ valence band. Under an applied bias, this can result in a reduced transmission, since the anti bonding $\sigma^*(2p_z)$ level in the Li₂O₂ conduction band is found to couple strongly to the metal substrate and create localized interface states with poor coupling to the Li₂O₂ bulk states. These observations provide a possible explanation for the higher overpotential observed for charging than discharge.

© 2010 Elsevier B.V. All rights reserved.

1. Introduction

The need for better and more sustainable methods for energy storage is growing rapidly, in particular in the energy and transportation sectors. New solutions and materials for high energy and power density storage are needed to solve the increasing demand for competitive (Hybrid) Electric Vehicles (H)EVs, where existing nickel metal hydride (used in the Toyota Prius) and lithium-ion (Tesla Roadster) battery technologies fall short on price, range, charge- and lifetime.

Since its commercialization in 1991 [1–3], the Li-ion battery has dominated the market for rechargeable batteries [4,5], but only small improvements have subsequently been made in terms of the energy capacity [6,7], and the best Li-ion batteries are currently storing ~300 mAh/g [8]. While materials like Si or Ge nanowires [9,10] and 3D-integrated all-solid-state battery concepts [11] could provide some improvements to Li-ion batteries, it is generally recognized that radically new approaches are needed for batteries to offer a real alternative to fossil fuels and to achieve consumer acceptance, i.e. improved reliability and safety, and most importantly, improvements in driving range and charge/discharge rates.

Li–O₂, generally referred to as Li–air, batteries with non-aqueous (aprotic) electrolytes were first demonstrated to be rechargeable in 1996 [12] by formation of Li₂O₂ during discharge. Although progress has recently been made [13–22], e.g. by addition of MnO₂ [5], Au [21] and Pt [22] catalysts, substantial improvements are still needed. The main challenges facing the Li–air battery is the limited electrical efficiency resulting from the overpotential/polarization losses at the cathode under charge and discharge [5], and the limited power and current densities currently achievable [23]. The overpotential is the difference between the equilibrium potential ($U_0 = 2.96$ V for Li/Li₂O₂) and the voltage during current-flowing conditions, i.e. the energy loss in the process, $\eta_{\text{discharge}} = U_0 - U_{\text{discharge}}$ and $\eta_{\text{charge}} = U_{\text{charge}} - U_0$, respectively.

A large asymmetry is also observed in the overpotentials for charge and discharge, i.e. a significantly higher potential is needed for charging, e.g. $U_{\text{charge}} \approx 4.5$ V and $U_{\text{discharge}} \approx 2.5$ V on a porous carbon electrode [24]; making the charging overpotential the most pertinent challenge to solve. We have previously proposed the initial step in the critical charging process to involve the formation of bound lithium superoxide species, LiO₂^{*}, on the surface of Li₂O₂ [25]. These species form as a consequence of the creation of a lithium vacancy, V_{Li} , and subsequent transport of a lithium ion (Li⁺) through the electrolyte and an electron (e[−]) through Li₂O₂ to the electrode. We also showed that the presence of lithium vacancies in Li₂O₂ makes the otherwise insulating Li₂O₂ overlayer conduct-

* Corresponding author. Tel.: +45 4677 5818; fax: +45 4677 5758.

E-mail address: teve@risoe.dtu.dk (T. Vegge).

ing via holes in the valence band. For thin Li_2O_2 overlayers, surface vacancies are likely sufficient to obtain electronic conduction, but under high discharge rates, e.g. for automotive applications, where Li_2O_2 islands and thicker films are formed, either energetically expensive bulk lithium vacancies or other conduction channels, such as deposited Au-clusters [21], must be available to achieve electronic conduction.

Highly different conditions exist during charge and discharge, and the combined use of two distinctly different catalysts may be required, similar to the catalysts for Oxygen-Reduction-Reaction (ORR) [26,27] and Oxygen-Evolution-Reaction (OER) [28], respectively. Au has been shown to lower the overpotential for discharge [21] and recent experiments by Lu et al. [24] have shown Pt to lower the overpotential for charging dramatically, although at the cost of a reduced capacity. A bifunctional PtAu/C catalyst was also demonstrated [22] to retain the main properties of the two catalysts on charge and discharge, respectively. These results were obtained under optimized O_2 -conditions and at low current densities, and the authors showed that the overpotentials grow significantly at increased currents. This effect is observed for both charge and discharge, although significantly more pronounced for the charging overpotential, where an increase of $\eta_{\text{charge}}(50 \text{ mA/g}) \approx 0.5 \text{ V}$ to $\eta_{\text{charge}}(250 \text{ mA/g}) \approx 1.0 \text{ V}$ is observed on the PtAu/C catalyst [22]. These observations underline the importance of obtaining a detailed understanding of the electronic conduction mechanisms at the insulator–catalyst interface.

Here, we apply non-equilibrium Green's function (NEGF) calculations [29] to determine the electronic transport through Li_2O_2 as well as Li_2O_2 deposited on the two promising transition metal catalysts, Au and Pt. This method has been used extensively to study quantum transport in a variety of different nano-scale systems including molecular junctions [30,31], atomic metal chains [32] and carbon nanotubes [33,34]. Here, we investigate the transport through Li_2O_2 grown on the close packed metal (1 1 1) facets, for the defect free interfaces as well as in the presence of lithium vacancies.

2. Theoretical methods

2.1. GPAW calculations

All calculations are performed within density functional theory [35,36] as implemented in the GPAW package [37,38] using the Atomic Simulation Environment [39] developed at the Technical University of Denmark. The GPAW package is a real space grid algorithm based on the projector augmented wavefunction method [40] with frozen core approximation. All calculations are spin polarized and performed using the RPBE exchange correlation functional [41]. All systems are sampled with a grid spacing of 0.2 \AA and the slab systems (see Section 3) are sampled with a $(2,2,1)$ k -point grid, while calculations of bulk metals are sampled using $(8,8,8)$ k -points.

2.2. Non-equilibrium electron transport Green's function method

Finite bias electron transport calculations are performed using a localized LCAO basis set, i.e. linear combination of atomic orbitals, as implemented in GPAW [42]. Here, a central device region (C) is connected to two semi-infinite leads (L) and (R), e.g. Au(1 1 1) (L) and $\text{Li}_2\text{O}_2(0001)$ slabs (R) as seen in Fig. 1, which are kept at fixed electronic chemical potentials, μ_L and μ_R , to simulate an applied bias voltage of $V = (\mu_L - \mu_R)/e$ across the device region; in this case the $\text{Li}_2\text{O}_2(0001)@Au(111)$ interface (Fig. 1). As a consequence of the electronic screening, the electron potential inside the leads converges rapidly to the bulk value and sets the boundary conditions for the electrostatic potential inside C. Rather than obtaining the

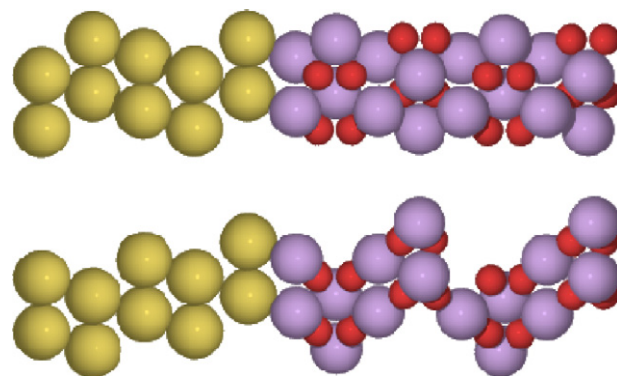


Fig. 1. The calculational setup for the scattering region for the $\text{Li}_2\text{O}_2(0001)@Au(111)$ (upper) and $\text{Li}_2\text{O}_2(0001)_{\text{vac}}@Au(111)$ (lower) interfaces, i.e. the same interface with a Li-vacancy in the middle of the Li_2O_2 layer. The super cells contain 5 metal layers and 4 Li_2O_2 layers and 21 (upper) and 41 (lower) atoms in total.

wavefunctions from the eigenvalue equation we work with the Green's function (GF) of the central region defined by

$$G(E) = [ES - H_C - \Sigma_L(E) - \Sigma_R(E)]^{-1} \quad (1)$$

where S and H_C are, respectively, the overlap and Hamiltonian matrix of the central region in the LCAO basis. Note that we have suppressed the dependence on the bias voltage, V , in the above expression for notational simplicity. The self-energies, $\Sigma_{L/R}$, incorporate the open boundary conditions of the infinite bulk electrodes. We obtain the electron density, $n(r)$, by integrating the diagonal of the Green function, $G(r,r;E)$, along a contour in the complex energy plane. The Poisson equation is solved on the real-space grid to obtain the electrostatic contribution to the effective potential, $v(r)$, in region C. The boundary conditions for the Poisson equation at the C–L and C–R interfaces are given by the bulk potential of the leads (shifted by the applied bias voltage $\pm eV/2$), while periodic boundary conditions are used in the plane perpendicular to the direction of transport. The cycle $G \rightarrow n(r) \rightarrow v(r) \rightarrow H_C \rightarrow G$ is iterated until self-consistency using Pulay density mixing [43]. At self-consistency the elastic transmission function is calculated from [38,44]

$$T(E; V) = \text{Tr}[G(E)\Gamma_L(E)G(E)^\dagger\Gamma_R(E)] \quad (2)$$

where $\Gamma_{L/R}(E) = i(\Sigma_{L/R}(E) - \Sigma_{L/R}(E)^\dagger)$ and the trace is taken over the central region basis functions. In physical terms $T(E; V)$ gives the transmission probability for an electron incident on the interface with an energy E under an applied bias V . Finally, the current *per unit cell* is obtained from

$$I(V) = G_0 \int_{\mu_L}^{\mu_R} T(E; V) dE \quad (3)$$

where $G_0 = 2e^2/h$ is the quantum unit of conductance and corresponds to a resistance of $12.9 \text{ k}\Omega$.

2.3. Reaction pathways and defect mobility

To analyze the mobility of the lithium vacancies, we determine the minimum energy path and energy barriers using the nudged elastic band NEB method [45,46]. We then determine the thermally activated reaction rates, $r(T)$, within harmonic transition state theory (hTST) [47,48], using the ground state activation energy, E_a , and the vibrational frequencies at the initial (ν_{IS}) and saddle points (ν_{TS}):

$$r(T) = \nu \text{Exp}\left(-\frac{E_a}{k_B T}\right) = \left(\frac{\Pi \nu_{\text{IS}}}{\Pi \nu_{\text{TS}}}\right) \text{Exp}\left(-\frac{E_a}{k_B T}\right) \quad (4)$$

The vibrational frequencies are obtained using a finite difference approximation of the Hessian matrix with back and forward displacements of 0.01 Å. The prime indicates that the imaginary frequency corresponding to the reaction coordinate is omitted.

3. Computational setup

To investigate the influence of transition metals on the electronic transport during charge and discharge conditions, we have investigated the following three systems: (a) Li_2O_2 , (b) $\text{Li}_2\text{O}_2(0001)@\text{Au}(111)$ and (c) $\text{Li}_2\text{O}_2(0001)@\text{Pt}(111)$. The super cell slabs contain 21 atoms separated by 9–19 Å vacuum layers and the systems are modeled by 4 layers of Li_2O_2 on top of 5 metal layers using the lattice constants of the metals as retrieved from optimizations of the bulk metals (see Fig. 1); the bulk calculations use an orthorhombic super cell of 4 atoms to represent the fcc lattice. The slabs are optimized internally by keeping the two lowest metal layers in their bulk positions and relaxing the remaining atoms to a total force below 0.05 eV/Å. Lithium vacancies are modeled by removing a Li atom from a double super cell and relaxing the system internally; the resulting system has 41 atoms and half of the Li atoms in one of the 8 Li layers are removed, corresponding to a total vacancy concentration $[V_{\text{Li}}]$ of 6.25%.

For the transport calculations, the central region (C) describing the metal– Li_2O_2 interface also contains 5 layers of metal and 4 layers of Li_2O_2 . We have verified that this is sufficient to achieve convergence of the current and potential drop across the interface. The electrode regions, i.e. bulk metal and Li_2O_2 , are calculated with normal DFT with periodical boundary conditions. We used a (6,2,1) k -point sampling for the NEGF self-consistent loop and a (12,4,1) k -point grid for evaluating the current. The PBE functional [49] is used for exchange–correlation, and an LCAO basis set corresponding to single-zeta plus polarization is adopted for all atomic species. We have verified that the results are converged with respect to the size of the LCAO basis set.

In the finite bias calculations, a positive bias is defined as sending electrons from the left to the right, i.e. in the case of $\text{Li}_2\text{O}_2(0001)@\text{Au}(111)$, Fig. 1, sending electrons from the metal to Li_2O_2 , corresponding to battery discharge ($2\text{Li}^+ + 2\text{e}^- + \text{O}_2 \rightarrow \text{Li}_2\text{O}_2$); negative bias then corresponds to battery recharge.

4. Results and discussion

In our analysis of the electronic transport, we have focused on the electrode/catalyst interface in the steady state situation where the first layers of Li_2O_2 are already formed; corresponding to the situation following the initial discharge or under charging conditions. In this study, we do not include possible effects at the Li_2O_2 –electrolyte interface.

We have previously determined the free energies of the reaction intermediates on a stepped $\text{Li}_2\text{O}_2(1-\bar{1}00)$ surface [25], and by correcting for a small error in the applied Li_{BCC} formation energy, we find a heat of formation of Li_2O_2 of $\Delta H = -5.92$ eV (free energy of formation of $\Delta G = -5.28$ eV) as compared to experimental values of $\Delta H = -6.56$ eV and $\Delta G = -5.91$ eV, respectively [50]. The calculated equilibrium potential is thus $U_0 = -\Delta G/2e = 2.64$ V compared to 2.96 V from experiments. During discharge, all steps remain downhill in free energy until a potential of $U_{\text{discharge}} = \min[-\Delta G_i/e] = 2.26$ V is reached, yielding an overpotential for discharge of $\eta_{\text{discharge}} = U_0 - U_{\text{discharge}} = 0.38$ V. During charging, a potential of 3.32 V or higher is needed for all steps to be downhill in free energy, giving $U_{\text{charge}} = \max[-\Delta G_i/e] = 3.32$ V, and resulting in a charging overpotential of $\eta_{\text{charge}} = U_{\text{charge}} - U_0 = 0.68$ V, i.e. a 0.3 V asymmetry compared to $\eta_{\text{discharge}}$. For details on the free energy calculations, please refer to Ref. [25].

In the presence of transition metal catalysts, e.g. Au and Pt as investigated here and previously by Xu and Shelton [51], the Li_2O_2 discharge product can grow on the energetically preferred (111) metal facets, which both have a reasonable lattice match with to the (0001) facet of Li_2O_2 , i.e. $a_{\text{Li}_2\text{O}_2} = 3.22$ Å, $a_{\text{Au}} = 2.97$ Å and $a_{\text{Pt}} = 2.83$ Å, see Fig. 1. Other interfaces are also possible [52], and e.g. the lattice constant of the reconstructed $\text{Li}_2\text{O}_2(1-\bar{1}00)$ facet, $c_{\text{Li}_2\text{O}_2(1-\bar{1}00)} = 7.83$ Å, has a reasonable match with the 8.40 Å and 8.00 Å found for the (110) metal facets of Au and Pt, respectively. TEM experiments by Lu et al. [22] show the Au, Pt and PtAu nanoparticles, used in their Li–air experiments, to be dominated by (111) facets, favoring growth at this interface.

In the following, we show that the electronic transport depends on the specific orientation and lattice matching at the interface region, due to the alignment of the O_2^{2-} peroxide ion and its distance to the metal atoms. We find that pinning of the Fermi level by lithium vacancies at the top of the valence band of Li_2O_2 can lead to a lowering of the electronic transport across the interface, as a consequence of the creation of localized interface states.

4.1. Pure Li_2O_2

From the projected electronic density of states (PDOS) for Li_2O_2 (Fig. 2), it is seen that the conduction and valence bands are dominated by the oxygen 2p orbitals and show a strong resemblance to molecular O_2 . Here, two neighboring lithium atoms have donated their 2s electrons to fill the empty states in the anti bonding $\pi^*(2p_x)$ and $\pi^*(2p_y)$ levels and form the peroxide ion, O_2^{2-} , causing an extension of the O–O bond from 1.24 Å to 1.56 Å. The conduction band is almost exclusively comprised of the oxygen $2p_z$ orbitals (see Fig. 2) forming the anti bonding $\sigma^*(2p_z)$ peroxide level. In contrast to the occupied $\pi^*(2p_x)$ and $\pi^*(2p_y)$ orbitals, the $\sigma^*(2p_z)$ orbital is aligned along the O–O axis.

As expected for GGA calculations, the band gap of bulk Li_2O_2 is substantially underestimated in GPAW, yielding a value of only 1.3 eV, compared to the 4.9 eV obtained with the more accurate GW calculations [25]. This underestimation of the band gap is likely to influence the absolute numbers for the onset potentials for electronic transmission, but the fundamental understanding and trends are still expected to hold. The absolute values of the determined onset potentials for charge and discharge can thus be expected to be correspondingly underestimated compared to experiments.

We have previously outlined the importance of lithium vacancies on the electronic conduction in bulk Li_2O_2 [25], where they were shown to pin the Fermi level at the top of the valence band (Fig. 2). Here, we see that the lithium vacancy induces a splitting of the conduction band into two separate bands around 2 and 4 eV.

We determine the V_{Li} formation energy to be 3.09 eV in the bulk for a low vacancy concentration of $[V_{\text{Li}}] = 1/32$ (3%), marginally lower (3.04 eV) at the 1/16 concentration used in the transport calculations and 3.00 eV in high concentration limit (1/8). The formation energy is slightly lower in the surface region, depending on the specific facet and site, and the value at the interface is likely to depend on the specific coordination to the metal. Although the absolute numbers may be sensitive to the concentration and specific configuration of the vacancies, this effectively means that for potentials $U_{\text{charge}} > 3.09$ V, there will be a thermodynamic driving force to create lithium vacancies. Using NEB calculations, we find the barrier for bulk V_{Li} migration to be 0.36 eV with a corresponding hTST prefactor of $\nu = 3.4 \times 10^{12} \text{ s}^{-1}$, resulting in a jump rate of $r = 3.6 \times 10^6 \text{ s}^{-1}$ (Eq. (4)) at room temperature. Recent experiments have shown a significant decrease in the capacity and output voltage of Li–air batteries when operated at lower temperatures [53], indicating the importance of thermally activated processes. The formation energy and barrier for V_{Li} mobility are, however, sufficiently

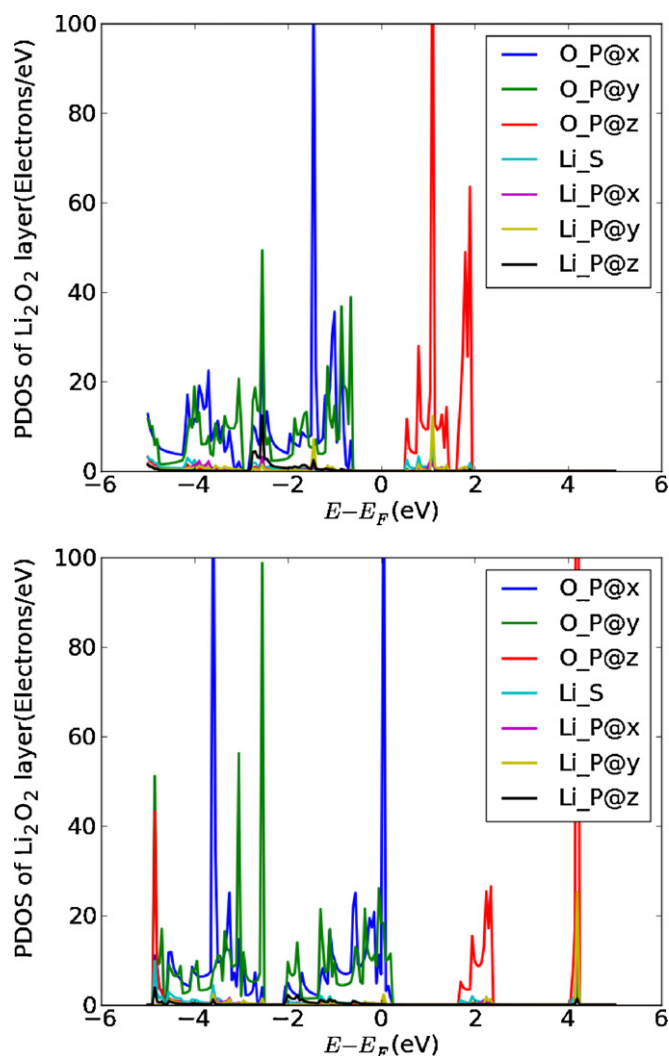


Fig. 2. The projected electronic density of states (PDOS) relative to the Fermi energy for bulk Li_2O_2 (upper) and bulk $\text{Li}_2\text{O}_{2\text{vac}}$ (lower), i.e. bulk Li_2O_2 with a lithium vacancy. The top of the valence and conduction bands are seen to be dominated by the oxygen p orbitals, and bulk Li_2O_2 is found to have band gap of 1.3 eV. The lithium vacancy is seen to pin the Fermi level (dashed line) at the top of the valence band and induce a splitting of the conduction band and a corresponding up-shift in energy.

low to assume that under changing conditions, i.e. $U_{\text{charge}} > 3.5$ V, mobile bulk vacancies will expectedly be present and distributed throughout the Li_2O_2 layers. Whereas surface vacancies are likely to be present during discharge, $U_{\text{discharge}} < 2.8$ V, the bulk concentration is expected to be low.

Fig. 3 shows the calculated transmission coefficient at zero applied bias (0 V) for the vacancy free Li_2O_2 system (black) and the system containing a lithium vacancy (red). In the figure it is seen that transport is only possible in the presence of lithium vacancies (due to the band gap of the defect free system), where the Fermi level is pinned at the top of the valence band. In this case, the conduction occurs via the holes in valence band.

4.2. $\text{Li}_2\text{O}_2(0001)\text{@Au}(111)$

The relaxed $\text{Li}_2\text{O}_2(0001)\text{@Au}(111)$ and $\text{Li}_2\text{O}_2(0001)_{\text{vac}}\text{@Au}(111)$ interfaces are shown in Fig. 1. From the figure, it is seen the peroxide ions are aligned perpendicular to the interface region and located at distance of ~ 4.2 Å above the gold surface. The lithium vacancy is located in the middle of the Li_2O_2 part of the scattering region, thus creating a higher vacancy concentration (1/2) in one

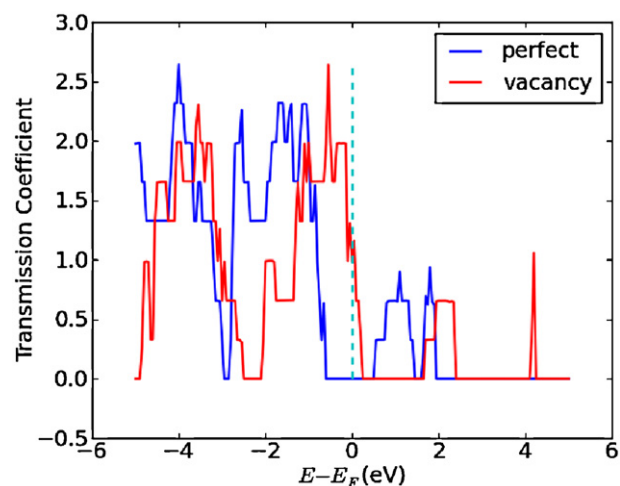


Fig. 3. Calculated transmission coefficients at zero bias (0 V) for bulk Li_2O_2 without lithium vacancies (blue) and with a lithium vacancy (red). The conductance is seen to be zero for the perfect system, but the presence of the lithium vacancy pins the Fermi level (dashed line) at the top of the valence band. (For interpretation of the references to color in this figure legend, the reader is referred to the web version of the article.)

lithium plane compared to the average value (1/16). This setup was chosen due to the requirements of the transport calculations, and in light of the limited sensitivity observed for the vacancy formation energy and PDOS, the obtained results are expected to be representative of different vacancy concentrations, although variations in the absolute currents are expected depending on the specific concentration and configuration of the vacancies.

The projected electronic density of states of the scattering region is shown in Fig. 4 for two different situations, i.e. the defect free $\text{Li}_2\text{O}_2(0001)\text{@Au}(111)$ interface (upper), where the anti bonding $\sigma^*(2p_z)$ level is seen to be broadened compared to the bulk Li_2O_2 situation in Fig. 2 (upper), and the $\text{Li}_2\text{O}_2(0001)_{\text{vac}}\text{@Au}(111)$ interface with a lithium vacancy (lower). For both systems, the top of valence band and the conduction band is seen to be dominated by the oxygen p orbitals. The lithium vacancy pins the Fermi level at the top of the anti bonding $\pi^*(2p_x)$ and $\pi^*(2p_y)$ peroxide levels in the valence band (lower), as seen for bulk $\text{Li}_2\text{O}_{2\text{vac}}$. The conduction band is also seen to split into an interface state at slightly lower energy, around 1–2 eV, and a bulk-like band, which has been shifted up in energy by an amount similar to that observed for the pinning in bulk Li_2O_2 (Fig. 2). The splitting is a consequence of the short spacial separation of the relevant molecular orbitals to the metal. Since the conduction band consists mainly of oxygen $2p_z$ orbitals (the anti bonding $\sigma^*(2p_z)$ peroxide level), which are aligned along the molecular axis, the coupling of the O_2^{2-} ions closest to the metal is so strong that they will follow the electronic chemical potential of the metal, μ_L , resulting in a weak coupling to the bulk-like Li_2O_2 states and thus a low electronic transport.

Since the formation energy of a lithium vacancy is below the minimum charging potential of $U_{\text{charge}} \geq 3.5$ V, such vacancies will be present during charging conditions and the charging currents should thus be evaluated in the presence of lithium vacancies. At discharge potentials, $U_{\text{discharge}} \leq 2.8$ V, the concentration of bulk lithium vacancies will be lower and the defect free scenario is likely to be applicable.

During the critical charging process (negative bias, V), the Fermi level in Au is lowered by $eV/2$ and correspondingly raised by $eV/2$ in Li_2O_2 ; causing electron transfer from Li_2O_2 to Au (Fig. 5). Due to the band gap in Li_2O_2 this will only be possible when the applied bias is sufficient to overcome the band gap and allow transfer from the conduction band of Li_2O_2 . At a negative bias of -2 V, the PDOS for

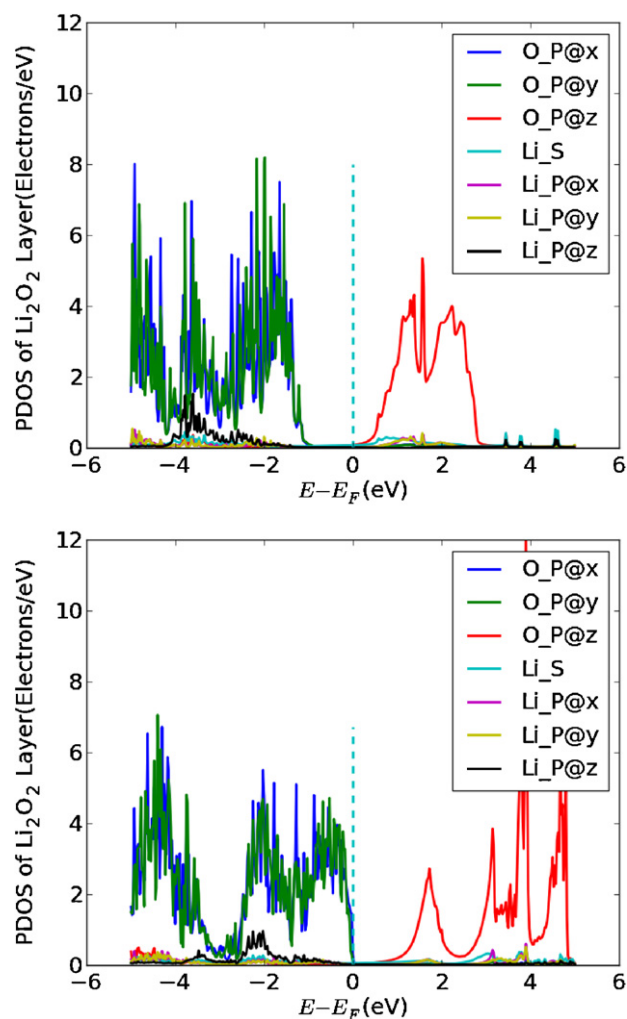


Fig. 4. The project electronic density of states (PDOS) relative to the Fermi energy for $\text{Li}_2\text{O}_2(0001)@Au(111)$ (upper) shows a valence band dominated by oxygen the p_x and p_y orbitals and a conduction band which is dominated by oxygen p_z orbitals, separated by a band gap of 1.8 eV. In the PDOS for $\text{Li}_2\text{O}_2(0001)_{vac}@Au(111)$ (lower), the lithium vacancy is seen to pin the Fermi level (dashed line) at the top of $\pi^*(2p_x)$ and $\pi^*(2p_y)$ level in the valence band and split the conduction band into a low energy interface state at 1–2 eV and a bulk-like band around 4 eV.

the vacancy system shows that the $\sigma^*(2p_z)$ interface state couples strongly to the metal and follows the electronic chemical potential of gold (μ_L). The $\pi^*(2p_x)$ and $\pi^*(2p_y)$ levels on the other hand follow the Fermi level in Li_2O_2 . Looking at Fig. 2, there are no bulk states corresponding to the $\sigma^*(2p_z)$ interface state and hence there will be poor transport through this state.

Fig. 6 shows the calculated transmission curves for $\text{Li}_2\text{O}_2(0001)@Au(111)$ (upper) and $\text{Li}_2\text{O}_2(0001)_{vac}@Au(111)$ (lower) at three different bias potentials: 0 V (blue), 1 V (red) and 2 V (green); corresponding to three stages of the battery discharge. At zero bias (blue), the transmission is seen to be zero in both systems. At 1 V (red), the transmission peak is seen to be at the edge of the bias window for the defect free system giving a small transmission, but effectively zero for the system with a vacancy. At 2 V (green), the transmission peak in the conduction band of $\text{Li}_2\text{O}_2(0001)@Au(111)$ (upper) is clearly within the bias window (dashed green lines), and resulting in significant transmission, whereas the $\text{Li}_2\text{O}_2(0001)_{vac}@Au(111)$ (lower) system only has a limited transmission through the valence band. The conduction band transmission peak is seen to remain fixed in the perfect system, but shift with the Fermi level of Li_2O_2 for the vacancy system.

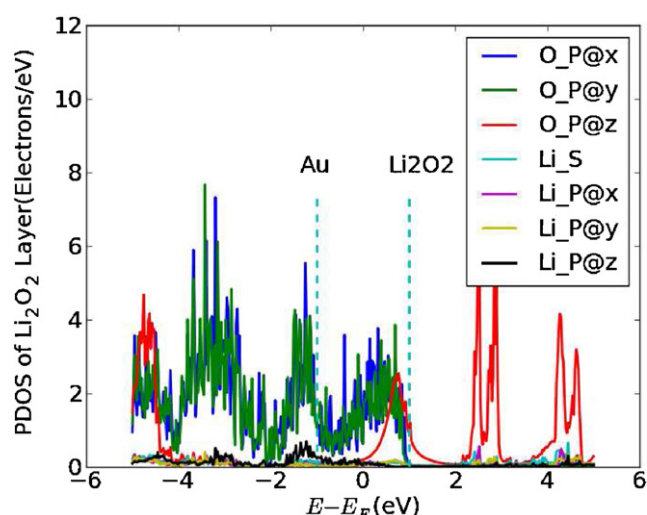


Fig. 5. The project density of states (PDOS) relative to the Fermi energy for $\text{Li}_2\text{O}_2(0001)_{vac}@Au(111)$ at a negative bias of -2 V (charging conditions), where the Fermi level of Au is seen to be shifted down by 1 eV and correspondingly up by 1 eV for Li_2O_2 (dashed lines). The oxygen p_x and p_y orbitals are seen to follow the electronic chemical potential of Li_2O_2 , whereas the localized p_z orbital follows the electronic chemical potential of Au. The bulk-like part of the p_z orbital couples primarily to Li_2O_2 and remains outside the bias window.

Fig. 7 shows the equivalent transmission curves at 0 V (blue) as a reference and two negative bias potentials (charging): -1 V (red) and -2 V (green). At -1 V (red), a small transmission is possible through the valence band in the vacancy system and the conduction band peak is seen to be at the edge of the bias window (dashed red lines) for the perfect system. At -2 V (green), the transmission peak is in the bias window (dashed green lines) for the perfect system and resulting in significant transmission through the conduction band, whereas only a limited transmission is possible in the vacancy system.

4.3. $\text{Li}_2\text{O}_2(0001)@Pt(111)$

Identical calculations have been performed on the $\text{Li}_2\text{O}_2(0001)@Pt(111)$ and $\text{Li}_2\text{O}_2(0001)_{vac}@Pt(111)$ interfaces as for Au. The lattice constant of Pt is also found to have a good match with the $\text{Li}_2\text{O}_2(0001)$ surface, and the interface distances are comparable to those found for Au.

The calculated PDOS for the $\text{Li}_2\text{O}_2(0001)@Pt(111)$ and $\text{Li}_2\text{O}_2(0001)_{vac}@Pt(111)$ interfaces are shown in Fig. 8, and a strong resemblance to the gold interface is observed. Only a small difference is observed in the band gap, where 1.6 eV is found for the Pt(111) interface compared to 1.8 eV for the Au(111) interface. As for the PDOS, the calculated transmission coefficients at different bias potentials are also very similar to those obtained for Au and not shown here, since the main differences are well captured by the comparison of the IV curves presented in the following section.

4.4. Calculated IV curves

Fig. 9 shows the calculated IV curve for defect free $\text{Li}_2\text{O}_2(0001)@Au(111)$ (blue) and $\text{Li}_2\text{O}_2(0001)@Pt(111)$ (turquoise) systems. The conduction is found to be limited ($\sim 10^{-7}$ μA) at low bias (± 0.2 V) for both systems. At onset potentials of around ± 1 V, respectively, the current is seen to grow rapidly. A slight asymmetry is also observed, indicating a faster transport under charging than discharging conditions when no defects are present. Slightly lower onset potentials are seen for

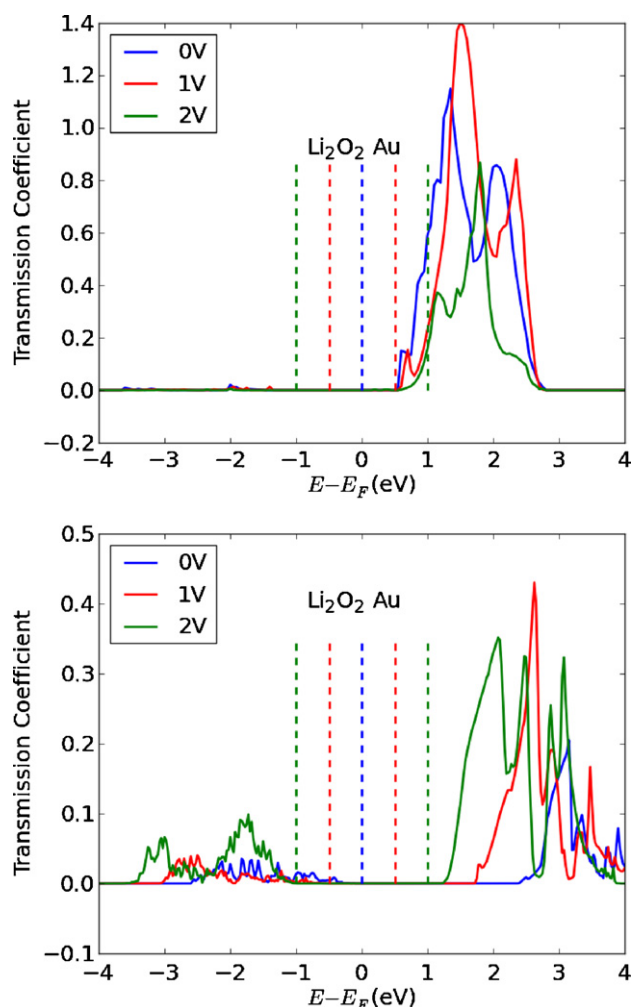


Fig. 6. Transmission curves for $\text{Li}_2\text{O}_2(0001)@Au(111)$ (upper) and $\text{Li}_2\text{O}_2(0001)_{\text{vac}}@Au(111)$ (lower) at three different bias potentials: 0V (blue), 1V (red) and 2V (green); corresponding to three stages of the battery discharge. At zero bias (blue), the transmission is seen to be zero in both systems. At 1V (red), the transmission peak is seen to be at the edge of the bias window (dashed red lines) for the defect free system, but effectively zero for the vacancy system. At 2V (green), the transmission peak in the conduction band of $\text{Li}_2\text{O}_2(0001)@Au(111)$ (upper) is in the bias window (dashed green lines) resulting in significant transmission, whereas the $\text{Li}_2\text{O}_2(0001)_{\text{vac}}@Au(111)$ (lower) system only has a limited transmission through the valence band. The conduction band transmission peak is seen to remain fixed in the perfect system, but shift with the Fermi level (dashed lines) of Li_2O_2 for the vacancy system. (For interpretation of the references to color in this figure legend, the reader is referred to the web version of the article.)

Pt than Au, which is a likely consequence of the smaller interface band gap.

Given the higher potentials needed for charging, part of the explanation for the experimentally observed asymmetry in the overpotentials for charging and discharging can be a result of bulk lithium vacancies being readily formed at charging potentials and highly mobile at room temperature, $r_{\text{jump}} = 3.6 \times 10^6 \text{ s}^{-1}$, in contrast to discharge conditions.

Fig. 10 shows the calculated IV curve for $\text{Li}_2\text{O}_2(0001)_{\text{vac}}@Au(111)$ (red) and $\text{Li}_2\text{O}_2(0001)_{\text{vac}}@Pt(111)$ (green) systems with lithium vacancies. The conduction is found to be limited but high ($\sim 10^{-4} \mu\text{A}$) compared to the defect free interface at low bias ($\pm 0.2 \text{ V}$) for both systems. At an onset potential of around -0.5 V (charging), the current is seen to grow, whereas no increase is observed for discharge up to 2 V . The current is found to be highly asymmetric and the absolute currents during charging (negative

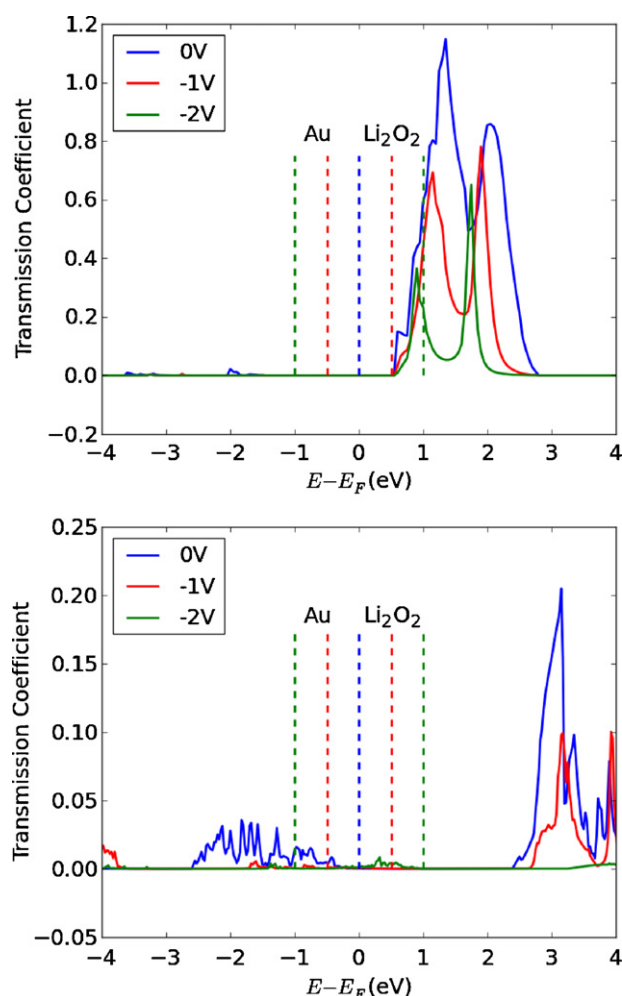


Fig. 7. Transmission curves for $\text{Li}_2\text{O}_2(0001)@Au(111)$ (upper) and $\text{Li}_2\text{O}_2(0001)_{\text{vac}}@Au(111)$ (lower) at three different bias potentials: 0V (blue), -1 V (red) and -2 V (green); corresponding to three stages of the battery charge. At zero bias (blue), the transmission is seen to be zero in both systems. At -1 V (red) a small transmission is possible through valance band in the vacancy system and the conduction band peak is seen to be at the edge of the bias window (dashed red lines) for the perfect system. At -2 V (green), the transmission peak is in the bias window (dashed green lines) for the perfect system, resulting in significant transmission through the conduction band, whereas only a limited transmission is possible in the vacancy system. (For interpretation of the references to color in this figure legend, the reader is referred to the web version of the article.)

bias) are found to be an order of magnitude below those for the defect free systems.

Under discharge conditions (without vacancies), a significantly higher current can be drawn on $Au(111)$, $I_{Au(111)}(2 \text{ V}) \sim 1.5 \mu\text{A}$, compared to charging situation (with vacancies), where the current is roughly an order of magnitude lower, $I_{Au(111)-\text{vac}}(-2 \text{ V}) = -0.18 \mu\text{A}$ (see Fig. 9). The situation is very similar on $Pt(111)$, having a significantly higher discharge current (without vacancies), $I_{Pt(111)}(2 \text{ V}) \sim 3.0 \mu\text{A}$ than that observed under charging conditions, $I_{Pt(111)-\text{vac}}(-2 \text{ V}) = -0.17 \mu\text{A}$ (with vacancies). Given the underestimation of the band gap in the calculation, the absolute values of the onset potentials are likely underestimated compared to experiments. Based on these results, the effect of the metal substrate is clear, and although the transport appears to be sensitive to the interface band gap, the observed differences between $Au(111)$ and $Pt(111)$ are within the uncertainty of the calculations; a good interface matching is, however, found to be important.

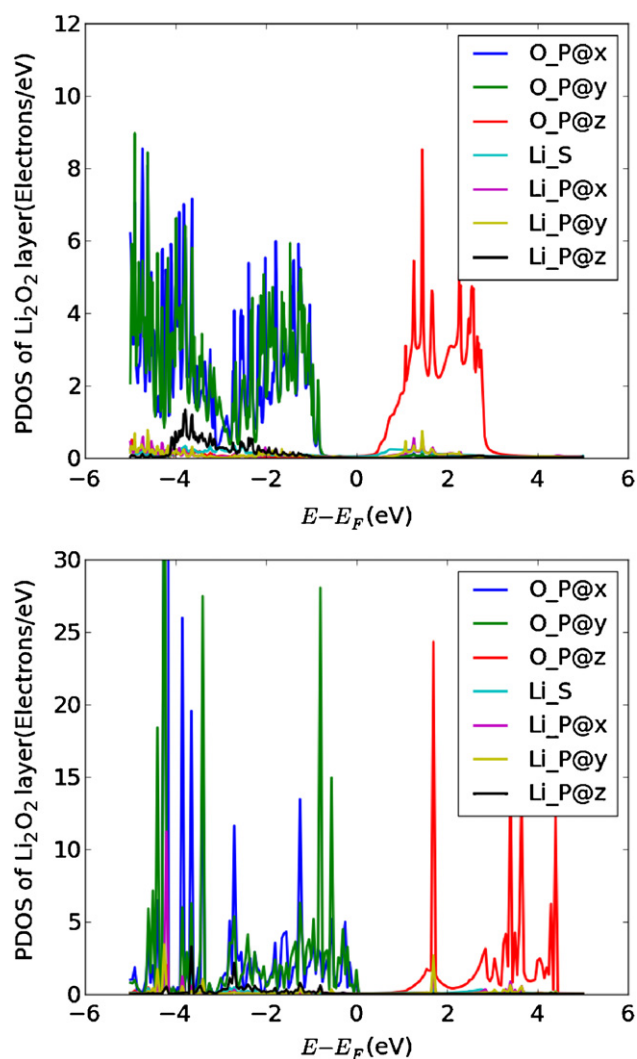


Fig. 8. The projected density of states (PDOS) relative to the Fermi energy for $\text{Li}_2\text{O}_2(0001)@\text{Pt}(111)$ (upper) and $\text{Li}_2\text{O}_2(0001)_{\text{vac}}@\text{Pt}(111)$ (lower). A band gap of 1.6 eV is found for the defect free interface, and the lithium vacancy is seen to pin the Fermi level (dashed line) at the top of the valance band of Li_2O_2 .

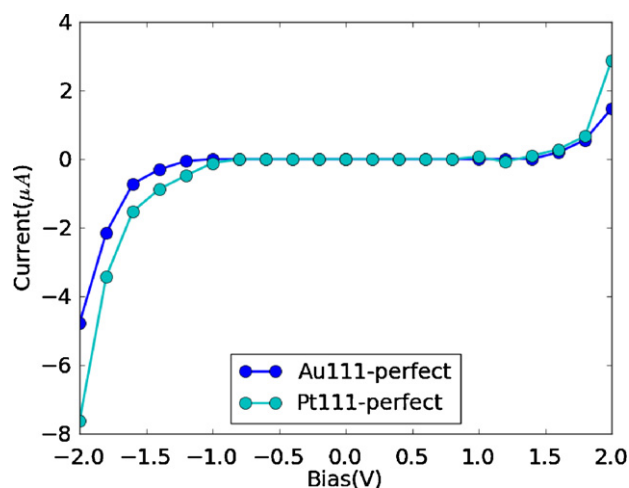


Fig. 9. Calculated IV curves for the defect free $\text{Li}_2\text{O}_2(0001)@\text{Au}(111)$ (blue) and $\text{Li}_2\text{O}_2(0001)@\text{Pt}(111)$ (turquoise) systems. The conduction is found to be limited ($\sim 10^{-7} \mu\text{A}$) at low bias ($\pm 0.2 \text{ V}$) for both systems. At the onset potentials of around $\pm 1 \text{ V}$, respectively, the current is seen to grow rapidly. A slight asymmetry is observed, indicating faster transport under charging conditions. Slightly lower onset potentials are seen for Pt than Au. (For interpretation of the references to color in this figure legend, the reader is referred to the web version of the article.)

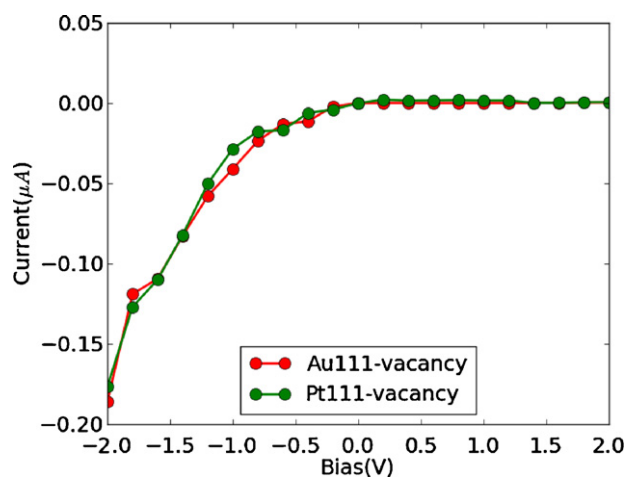


Fig. 10. Calculated IV curves for the $\text{Li}_2\text{O}_2(0001)_{\text{vac}}@\text{Au}(111)$ (red) and $\text{Li}_2\text{O}_2(0001)_{\text{vac}}@\text{Pt}(111)$ (green) systems with lithium vacancies. The conduction is found to be limited ($\sim 10^{-4} \mu\text{A}$) at low bias ($\pm 0.2 \text{ V}$) for both systems. At the onset potential of around -0.5 V (charging), the current is seen to grow, whereas no increase is observed for discharge up to 2 V . The current is found to be highly asymmetric and the absolute currents during charging are found to be an order of magnitude below those for the defect free systems (see Fig. 9). (For interpretation of the references to color in this figure legend, the reader is referred to the web version of the article.)

Experiments clearly show a decrease in the overpotentials when operating at low currents, most pronounced for the charging overpotential (negative bias) [22], where we also see the lowest conduction when the lithium vacancies are introduced. It should also be noted that the absolute currents obtained at high bias in this study ($\sim 1 \mu\text{A}/\text{nm}^2$ metal surface area) are significantly above those typically realized experimentally, e.g. $\sim 0.1 \text{ mA}/\text{cm}^2_{\text{electrode}}$ [24]. At low bias ($\pm 0.2 \text{ V}$), the absolute currents are significantly lower, e.g. $\sim 10^{-7} \mu\text{A}/\text{nm}^2_{\text{metal surface}}$ for $\text{Li}_2\text{O}_2(0001)@\text{Au}(111)$ and $\sim 10^{-4} \mu\text{A}/\text{nm}^2_{\text{metal surface}}$ for the $\text{Li}_2\text{O}_2(0001)_{\text{vac}}@\text{Au}(111)$ interface. This would correspond to a current of $\sim 10^{-4} \text{ mA}/\text{cm}^2_{\text{Au}(111)\text{ surface}}$ for the defect free system, and even when taking in to account that only a fraction of the electrode area consists of exposed (111) metal facets, the calculated currents are still significantly above those realized experimentally. It should also be noted that these numbers do not include the Li_2O_2 –electrolyte interface, which may cause the transport to depend on the thickness of the Li_2O_2 layer, such that arbitrarily low currents can be obtained depending on the thickness. Such a dependence would also be consistent with the observed drops in the required overpotential in the later stages of charging (thin Li_2O_2 layers) as reported by Lu et al. on Pt and PtAu/C [22,24].

The calculated transport is also assumed to be coherent, but it is uncertain whether this approximation holds under experimental conditions, where electron–phonon coupling and polarons, morphological effects and interactions with the electrolyte are likely to be important. The observed temperature dependence reported by Wilcke and co-worker [53] on the capacity and output voltage could be an indication of such interactions.

5. Conclusion

The electronic conduction is found to be sensitive to the orientation and lattice matching of the metal–insulator interface, and we show that the transport depends on the alignment of the O_2^{2-} peroxide ions in Li_2O_2 to the metal surface. The anti bonding interface $\sigma^*(2p_z)$ state in the conduction band couples strongly to the metal state and its electronic chemical potential (μ_L) in the $\text{Li}_2\text{O}_2(0001)@\text{Au}(111)$ and $\text{Li}_2\text{O}_2(0001)@\text{Pt}(111)$ interfaces.

Bulk lithium vacancies are found to be present under charging conditions and to pin the Fermi level at the top of the anti bonding peroxide $\pi^*(2p_x)$ and $\pi^*(2p_y)$ levels in the valence band of Li_2O_2 . Under an applied bias, these states follow the electronic chemical potential of Li_2O_2 (μ_R), whereas the interface $\sigma^*(2p_z)$ states are aligned along the O–O bond and have a strong coupling to the metal states and follow its electronic chemical potential, resulting in a reduced transport during charging.

These observations lead to a possible explanation for the experimentally observed asymmetry in the overpotentials for battery charge and discharge, which may enhance the $\sim 0.3\text{ V}$ asymmetry resulting from the formation of LiO_2^* species and the 4 electron process previously reported [25].

More work has to be done to understand the role of transition metal interfaces on the electronic transport in Li–air batteries. This includes a better understanding of the concentration of lithium and peroxide defects under different potentials, as well as other interfaces, e.g. the $\text{Li}_2\text{O}_2(100)/\text{Au}(110)$ interface, where the O_2^{2-} ions are aligned parallel to the metal and the dependence of thickness of the Li_2O_2 layers and the effect of the Li_2O_2 –electrolyte interface.

In addition to the electronic properties, a better understanding of the role of the electrolyte reactions in Li–air batteries is also required.

Acknowledgements

The authors would like to acknowledge the Danish Center for Scientific Computing, the Catalysis for Sustainable Energy (CASE) initiative and the Center of Atomic-Scale Materials Design (CAMD). CASE is funded by the Danish Ministry of Science, Technology and Innovation, and CAMD is funded by the Lundbeck Foundation. U.S. Department of Energy, Office of Basic Energy Sciences under Center on Nanostructuring for Efficient Energy Conversion (CNEEC) and Center for Interface Science and Catalysis – Sustainable energy through Catalysis (SUNCAT).

References

- [1] K. Mizushima, P.C. Jones, P.J. Wiseman, J.B. Goodenough, *Mater. Res. Bull.* 15 (1980) 783.
- [2] M.M. Thackeray, W.I.F. David, P.G. Bruce, J.B. Goodenough, *Mater. Res. Bull.* 18 (1983) 461.
- [3] T. Nagaura, *Prog. Batteries Solar Cells* 10 (1991) 209.
- [4] M.S. Whittingham, *Chem. Rev.* 104 (2004) 4271.
- [5] T. Ogasawara, A. Débart, M. Holzapfel, P. Novák, P.G. Bruce, *J. Am. Chem. Soc.* 128 (2006) 1390.
- [6] J.M. Tarascon, M. Armand, *Nature* 414 (2001) 359.
- [7] A. Shukla, T.P. Kumar, *Curr. Sci.* 93 (2008) 314.
- [8] M. Armand, J.M. Tarascon, *Nature* 451 (2008) 652.
- [9] L.F. Cui, R. Ruffo, C.K. Chan, H. Peng, Y. Cui, *Nano Lett.* 9 (2009) 491.
- [10] C.K. Chan, X.F. Zhang, Y. Cui, *Nano Lett.* 8 (2008) 307.
- [11] L. Baggetto, R.A. Niessen, F. Roozeboom, P.H. Notten, *Adv. Funct. Mater.* 18 (2008) 1057.
- [12] K.M. Abraham, Z. Jiang, *J. Electrochem. Soc.* 143 (1996) 1.
- [13] J. Read, et al., *J. Electrochem. Soc.* 150 (2003) A1351.
- [14] S.S. Zhang, D. Foster, J. Read, *J. Power Sources* 195 (2010) 1235.
- [15] C.O. Laoire, S. Mukerjee, K.M. Abraham, E.J. Plichta, M.A. Hendrickson, *J. Phys. Chem. C* 113 (2009) 20134.
- [16] B. Kumar, et al., *J. Electrochem. Soc.* 157 (2010) A50.
- [17] P.G. Bruce, B. Scrosati, J.M. Tarascon, *Angew. Chem. Int. Ed. Engl.* 47 (2008) 2930.
- [18] A. Débart, J. Bao, G. Armstrong, P.G. Bruce, *ECS Trans.* 3 (2007) 225.
- [19] A. Débart, J. Bao, G. Armstrong, P.G. Bruce, *J. Power Sources* 174 (2007) 1177.
- [20] J. Read, *J. Electrochem. Soc.* 153 (2006) A96.
- [21] F.U. Renner, et al., *Electrochim. Acta* 53 (2008) 6064.
- [22] Y.-C. Lu, Z. Xu, H.A. Gasteiger, *JACS Commun.* (2010), doi:10.1021/ja1036572.
- [23] X.-h. Yang, Y.-y. Xia, *J. Solid State Electrochem.* 14 (2010) 109.
- [24] Y.-C. Lu, Z. Xu, H.A. Gasteiger, M.C. Parent, V. Chiloyan, Y. Shao-Horn, *Electrochem. Solid State Lett.* 13 (2010) A69.
- [25] J.S. Hummelshøj, et al., *J. Chem. Phys.* 132 (2010) 1.
- [26] J. Greeley, J.K. Nørskov, *J. Phys. Chem. C* 113 (2009) 4932.
- [27] J. Greeley, et al., *Nat. Chem.* 1 (2009) 552.
- [28] R. Forgie, G. Bugosh, K.C. Neyerlin, Z.C. Liu, P. Strasser, *Electrochem. Solid State Lett.* 13 (2010) D36.
- [29] M. Brandbyge, J.L. Mozos, P. Ordejón, J. Taylor, K. Stokbro, *Phys. Rev. B* 65 (2002) 165401.
- [30] D.J. Mowbray, G. Jones, K.S. Thygesen, *J. Chem. Phys.* 128 (2008) 111103.
- [31] K.S. Thygesen, K.W. Jacobsen, *Phys. Rev. Lett.* 94 (2005) 036807.
- [32] K.S. Thygesen, K.W. Jacobsen, *Phys. Rev. Lett.* 91 (2003) 146801.
- [33] J.M. Garcia-Lastra, K.S. Thygesen, M. Strange, A. Rubio, *Phys. Rev. Lett.* 101 (2008) 236806.
- [34] K.S. Thygesen, K.W. Jacobsen, *Chem. Phys.* 319 (2005) 111.
- [35] P. Hohenberg, W. Kohn, *Phys. Rev. B* 136 (1964) B864.
- [36] W. Kohn, L.J. Sham, *Phys. Rev.* 140 (1965) 1133.
- [37] J.J. Mortensen, L.B. Hansen, K.W. Jacobsen, *Phys. Rev. B* 71 (2005) 035109.
- [38] J. Enkovaara, et al., *J. Phys.: Condens. Matter* 22 (2010) 253202.
- [39] S.R. Bahn, K.W. Jacobsen, *Comp. Sci. Eng.* 4 (2002) 56.
- [40] P. Blöchl, *Phys. Rev. B* 50 (1994) 17953.
- [41] B. Hammer, L.B. Hansen, J.K. Nørskov, *Phys. Rev. B* 59 (1999) 7413.
- [42] A.H. Larsen, M. Vanin, J.J. Mortensen, K.S. Thygesen, K.W. Jacobsen, *Phys. Rev. B* 80 (2009) 195112.
- [43] P. Pulay, *Chem. Phys. Lett.* 73 (1980) 393.
- [44] Y. Meir, N. Wingreen, *Phys. Rev. Lett.* 68 (1992) 2512.
- [45] G. Henkelman, H. Jonsson, *J. Chem. Phys.* 111 (1999) 7010.
- [46] H. Jónsson, G. Mills, K.W. Jacobsen, *Classical and Quantum Dynamics in Condensed Phase Simulations*, World Scientific, Singapore, 1998.
- [47] P. Hänggi, P. Talkner, M. Borkovec, *Rev. Mod. Phys.* 62 (1990) 251.
- [48] T. Vegge, T. Rasmussen, T. Leffers, O.B. Pedersen, K.W. Jacobsen, *Phys. Rev. Lett.* 85 (2000) 3866.
- [49] K. Burke, J.P. Perdew, Y. Wang, *Phys. Rev. Lett.* 77 (1996) 3865.
- [50] M.W. Chase Jr., *NIST-JANAF Thermochemical Tables*, fourth edition, *J. Phys. Chem. Ref. Data*, Monograph 9 (1998) 1–1951.
- [51] Y. Xu, W.A. Shelton, *J. Chem. Phys.* 133 (2009) 024703.
- [52] N. Seriani, *Nanotechnology* 20 (2009) 445703.
- [53] G. Girishkumar, B. McCloskey, A.C. Luntz, S. Swanson, W. Wilcke, *J. Phys. Chem. Lett.* 1 (2010) 2193.

DFT study of selective poisoning of Li-Air batteries for increased discharge capacity

Jón Steinar Garðarsson Mýrdal^{1,2} and Tejs Vegge^{1, a}

¹Department of Energy Conversion and Storage, Technical University of Denmark, Frederiksborgvej 399 Building 238, DK-4000 Roskilde, Denmark.

²Center for Atomic-scale Materials Design and Department of Physics, Technical University of Denmark, DK-2800 Lyngby, Denmark

^a E-mail: teve@dtu.dk

Abstract

The main discharge product at the cathode of non-aqueous Li-air batteries is insulating Li_2O_2 and its poor electronic conduction is a main limiting factor in the battery performance. Here, we apply density functional theory calculations to investigate the potential of circumventing this passivation by controlling the morphological growth directions of Li_2O_2 using directed poisoning of specific nucleation sites and steps. We show SO_2 to bind preferentially on steps and kinks on the (1-100) facet and effectively lowering the discharge potential by 0.4 V, yielding a more facile discharge on the (0001) surface. This process may prevent the growth of insulating thin films and ultimately lead to an increased accessible battery capacity resulting from improved electronic conduction to the active sites.

The demand for high-density energy storage solutions for electric appliances has increased the research on metal-air batteries in recent years. Despite the large success of the Li-ion battery, from its early days in the 1990's, there is a significant push for a more energy dense batteries. Even though there is still room for improving the Li-ion battery technology, there are fundamental limitations on how high energy densities you can reach in the frame of the Li-ion technology¹. Today one of the main limitations on the applicability of electronic products, such as laptops computers, smartphones and power tools is the time you can work without a recharge. These limitations become an even larger factor for electric vehicles (EV), where the competition is from highly energy dense fossil or synthetic fuels.

Of all the metal-air batteries, Li-air is the one with the highest theoretical energy density. If a commercial, secondary Li-air battery can be developed, it is estimated that it could have up to an order of magnitude higher energy density than modern Li-ion batteries¹. A Li-O₂ battery with aprotic solvent was first shown to be rechargeable in 1996 by Abraham *et al*, where Li₂O₂ was formed at the cathode during discharge². The massive interest in Li-air batteries as future, high energy density batteries has resulted in a plethora of publications and significant new insight into the fundamental mechanisms and challenges of aprotic Li-O₂ batteries has been gained in the last few years.

Still there are number of challenges that need to be overcome before the Li-air technology will be a practical application. A significant limitation for high capacity and power density batteries is the insulating nature of the Li₂O₂ deposits. With a band gap of 4.9 eV, as obtained from G₀W₀ calculations³, Li₂O₂ will ultimately limit the electronic conduction from the electrode to the active site⁴⁻⁶. It has been documented that the electronic conduction through Li₂O₂ becomes limiting for the electrochemical discharge already after a ~5 nm film is deposited (depending on the current density)⁵.

An essential aspect in solving the conduction limitations is the understanding the mechanisms governing growth and depletion of Li₂O₂ on Li₂O₂. Computational work by

Hummelshøj et al.³ showed that steps on reconstructed (1-100) surface could act as nucleation sites for low overpotential discharge. Subsequent work by e.g. Radin et al.^{7,8}, Lau et al.⁹ and Mo et al.¹⁰ has shown that a number of other facets have similar surface energies and will likely be exposed, including (0001), (1-100) and (11-20). Recent work by Hummelshøj et al.¹¹ has shown that these terminations will depend on potential and can be different under charge and discharge conditions, but kinks and steps on (1-100) and (0001) surfaces will control the growth of Li_2O_2 at lower current densities.

Computational and experimental work has shown that although coherent electron transport through Li_2O_2 is limited^{4,5}, hybrid functional (HSE06) and PBE+U calculations show that polaronic transport may still be significant, both in the bulk as hole¹² or electron¹³ polarons or a surface polarons⁸. Recent work by Garcia-Lastra *et al.*⁶ has demonstrated preferential conduction in the directions perpendicular to the [0001] direction, e.g. the [1-100] and [11-20] directions. This may explain the formation of toroidal Li_2O_2 particles consisting of stacked Li_2O_2 platelets with a highly uniform size and shape as observed by Mitchell et al. using HRTEM¹⁴. These platelets reach a thickness of about 5nm in the [0001] direction and a up to 200 nm in radius in the [1-100] directions¹⁴. A detailed control of the directions of growth and the Li_2O_2 morphology is therefore expected to be able to postpone the onset of sudden death resulting from lack of electronic conduction.

Large organic molecules such as sodium dodecyl sulfate (SDS) have been used to control the morphology of oxide particles during electrochemical growth¹⁵. Selective blocking of nucleation sites could thus enable preferential growth in directions where the electronic conduction is facile and/or formation of e.g. nanopillars or particles¹⁶, where surface conduction will be sufficient or simply delay the complete coverage of the electrode, in order to sustain the electrochemical discharge. It is also well documented in the catalysis literature^{17,18} that sulfur preferentially adsorbs to kink and step sites and here we combine

these aspects to proactively control the Li_2O_2 growth morphology by addition of sulfur rich species during battery discharge.

In this letter, we present a computational investigation of the binding of sulfur and SO_2 on kink and step sites of (1-100) and oxygen rich (0001) Li_2O_2 surfaces and determine the implications for the electrochemical discharge and growth of Li_2O_2 . We use the computational lithium electrode approach³ to determine the free energy of the reaction intermediates and to identify the preferred reaction mechanisms and the corresponding over- and effective potentials where charge/discharge is no longer exergonic. With the lithium electrode we define $U=0$ when bulk Li and ($\text{Li}^+ + \text{e}^-$) are at equilibrium. At an applied bias the free energy of a reaction is shifted by $-neU$, where n is the number of electrons that are reacted at the cathode.

All calculations presented here are performed using density functional theory (DFT)^{19,20} as it is implemented in the GPAW code^{21,22} using the atomic simulation environment (ASE)²³. GPAW is based on real space grids and uses the projector-augmented wave method (PAW) to describe non-valence electrons^{24,25}. The RPBE functional is used to approximate the electrons exchange and correlation²⁶. For the atomic structural energy minimization the calculation is continued until all forces are below 0.03 eV/Å. For the (1-100) surface calculations we used super cells consisting of 56-64 atoms slab with an approximately 18 Å vacuum layer between periodic images along the z-axis. The super cell is sampled with (4,4,1) k-point mesh and the distance between grid points is 0.15 Å. For the (0001) surface calculations, the super cells consisted of 121-124 atoms and was sampled with a (2,2,1) k-point mesh and 0.15 Å grid spacing.

To study the reaction of sulfur and sulfur oxide species on (1-100) (Figure 1) and (0001) (Figure 2) surfaces and the effect their presence has on the Li_2O_2 growth, we first calculate the reaction mechanisms for two formula units of Li_2O_2 at a step on a (1-100) surface, following the approach previously used by Hummelshøj et al.^{3,11} This leaves the

surface unchanged and prevents energy differences from changing the concentration of surface defects between the initial to the final state in playing a role in the overall reaction paths.

We considered 4 step reaction mechanisms on (1-100)^{3,11}, where all reaction steps are electrochemical and involve either Li^+ or LiO_2^+ . The calculations yield a heat of formation for Li_2O_2 of $\Delta H = -6.09$ eV and free energy of formation of $\Delta G = -5.46$ eV, which is slightly lower than the experimental values $\Delta H_{\text{Exp}} = -6.56$ eV and $\Delta G_{\text{Exp}} = -5.91$ eV²⁷. This gives us an equilibrium potential $U_0 = -\Delta G / 2e = 2.73$ V compared the experimental value $U_{0,\text{Exp}} = 2.96$ V. For the considered reaction mechanisms we get a free energy difference for each of the four reaction steps, ΔG_i . At zero potential all the reaction steps are downhill, but with an applied potential the free energy difference changes for each step as $\Delta G_{i,U} = \Delta G_i - eU$. For discharge the reaction will start to become limited when the lowest free energy step, $\Delta G_{i,\min}$, along the reaction path becomes uphill with applied potential, $U_{\text{dis}} = \min[-\Delta G_i/e] = 2.66$ V. In the same way it is the largest free energy step that is last to become downhill for the reversed reaction, at an applied potential of $U_{\text{ch}} = \max[-\Delta G_i/e] = 2.81$ V, opening up for charging. The overpotentials for discharge and charge are then given by $\eta_{\text{dis}} = U_0 - U_{\text{discharge}} = 0.07$ V and $\eta_{\text{ch}} = U_{\text{ch}} - U_0 = 0.08$ V, respectively.

As can be seen in Table 1, atomic sulfur is found to bind preferentially at the step/kink sites on the (0001) surface (see figure 2b) by nearly 0.7 eV compared to the step valley site on (1-100). It is, however, more relevant to study the binding of SO_2 which may be supplied in low concentrations in the O_2 feed at specific stage during discharge. Here, it is seen that SO_2 binds preferentially by ~ 0.7 eV at the step sites on (1-100) compared to (0001). A reduced binding energy is seen for SO_2 at higher concentrations, indicating that at low concentration it should spread over the step edges rather than clustering in high concentration islands.

The presence of SO₂ at the step valley site (see figure 1b) is found to reduce the binding energy of the initial LiO₂* species (c) compared to the pure discharge. The preferred next step is the addition of the second LiO₂* species (d), followed by two Li⁺ additions (e) and (f). It can be seen in the figure 3 that by completing the growth of Li₂O₂ at the step, SO₂ is effectively displaced from the step to the less stable terrace site, resulting in a loss in the equilibrium potential of 0.39 eV compared to growth on a clean step. The overpotential for discharge is also seen to increase from 0.07 eV to 0.33 eV resulting from a shift in the potential limiting step. This results in an effective lowering of the discharge potential by 0.54 eV, i.e. from $U_{\text{dis}} = 2.66 \text{ V}$ to $U_{\text{dis-SO}_2} = 2.02 \text{ V}$. The overpotential for charge is seen to increase from 0.08 V to 0.66 V and the potential for charge is found to exceed that of the pure system for the calculated mechanism. It is, however, possible that the charging process may proceed through another mechanism, e.g. as proposed by Peng et al.²⁸, which has not been considered here.

The DFT results indicate that selective poisoning with low concentrations of SO₂ in the O₂ feed will preferentially bind to step edges on the (1-100) facets and limit the initial growth on these facets. The substantial decrease in the discharge potential, lead by the lowering of the equilibrium potential, results in a shift of the Li₂O₂ growth from the kink sites on (1-100) surface to kink sites on the (0001) surface¹¹ (see figure 2). This process may limit rapid growth of passivating 2D platelet/islands with a surface normal in the poorly conducting [0001] direction and postpone the onset of sudden death resulting from loss of electronic conduction. Experimental investigations are currently ongoing to identify whether an increase in accessible discharge capacity can be achieved.

Acknowledgements

The authors acknowledge support from the Copenhagen Graduate School for Nano Science and Nano Technology, Center for Atomic-scale Materials Design (CAMD), Danish

Center for Scientific Computing and the ReLIable project funded by the Danish Council for Strategic Research – Programme Commission on Sustainable Energy and Environment (project #11-116792).

Table 1: Shows the adsorption energy for S and SO₂ at different surface sites. The most preferable adsorption takes place for SO₂ at a step valley site on a (1-100) surface.

Species	Surface	Site	Adsorption Energy [eV]
S	(1-100)	Step ridge	-1.33
		Step valley	-1.72
		Terrace valley	-0.61
S	(0001)	Step	-2.50
SO ₂	(1-100)	Step ridge	-7.11
		Step valley	-7.37
		Terrace valley	-5.82
		Step	-6.92
2nd SO ₂	(1-100)	Step ridge	-6.69

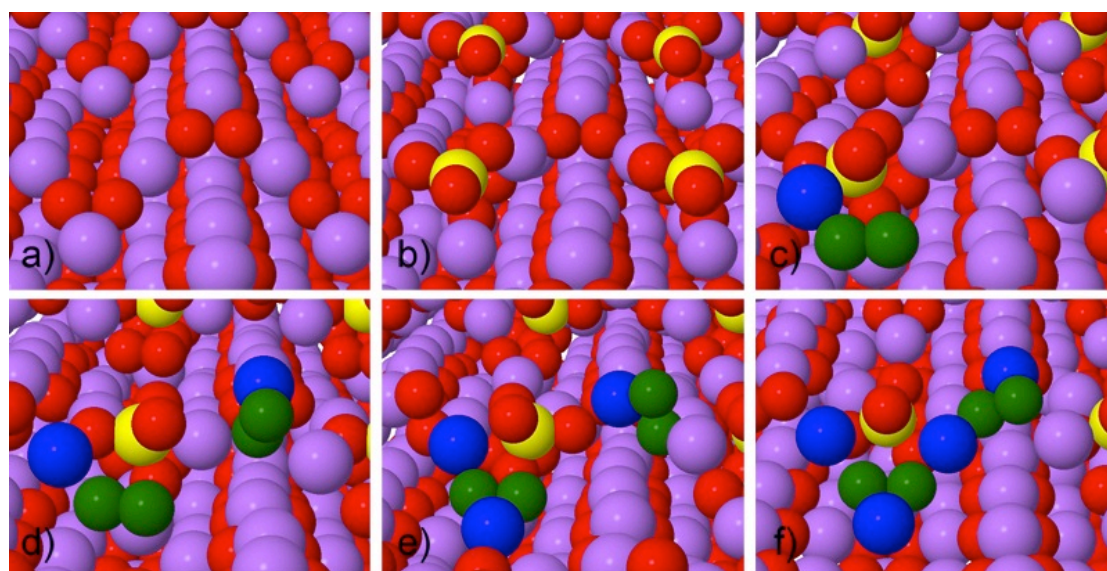


Figure 1. Surface structure of stepped Li₂O₂ (1-100) surface before and after adsorption of SO₂, as well as reaction steps during discharge. a) Clean stepped Li₂O₂ (1-100) surface. b) SO₂ adsorbs to the valley site of the step forming SO₄ surface specie. c) Li₂O₂ binds to surface. d) 2nd Li₂O₂ binds to surface. e) Li binds to surface. f) Second Li binds to surface, finishing discharge of 2 f.u., the growth of the step effectively moves the SO₂ from the step to the less favorable terrace site.

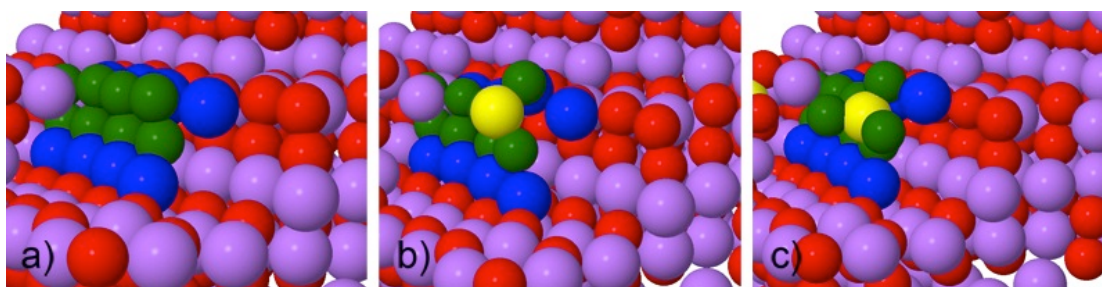


Figure 2. Surface structure of a step and a kink at Li_2O_2 (0001) surface, before and after adsorption with S and SO_2 has taken place. a) Clean kink, b) S adsorbs at the kink site and forms SO_2 surface species, c) SO_2 adsorbs at the kink site and form SO_4 surface species.

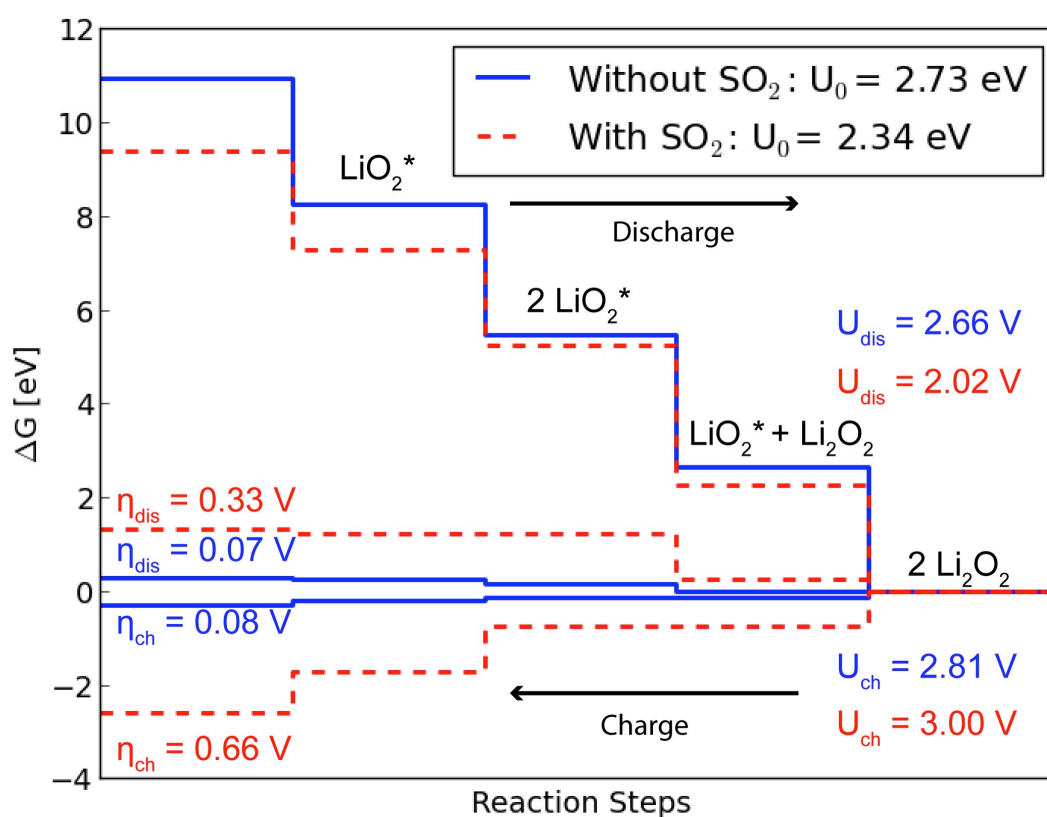


Figure 3. Calculated free energy diagrams for discharge from stepped (1-100) surface with and without adsorbed SO_2 . The diagram shows how the adsorbed SO_2 lowers the equilibrium potential and thereby the effective discharge potential making the discharge less favorable in the presence of SO_2 .

References:

- (1) Ogasawara, T.; Débart, A.; Holzapfel, M.; Novák, P.; Bruce, P. G. *J. Am. Chem. Soc.* **2006**, *128*, 1390–1393.
- (2) Abraham, K. M.; Jiang, Z. *J. Electrochem. Soc.* **1996**, *143*, 1–5.
- (3) Hummelshøj, J. S.; Blomqvist, J.; Datta, S.; Vegge, T.; Rossmeisl, J.; Thygesen, K. S.; Luntz, A. C.; Jacobsen, K. W.; Nørskov, J. K. *The J. of Chem. Phys.* **2010**, *132*, 071101.
- (4) Chen, J.; Hummelshøj, J. S.; Thygesen, K. S.; Myrdal, J. S. G.; Nørskov, J. K.; Vegge, T. *Catalysis Today* **2011**, *165*, 2–9.
- (5) Viswanathan, V.; Thygesen, K. S.; Hummelshøj, J. S.; Nørskov, J. K.; Girishkumar, G.; McCloskey, B. D.; Luntz, A. C. *J. Chem. Phys.* **2011**, *135*, 214704.
- (6) Garcia-Lastra, J. M.; Myrdal, J. S. G.; Thygesen, K. S.; Vegge, T. *J. Phys. Chem. C* (submitted).
- (7) Radin, M. D.; Rodriguez, J. F.; Tian, F.; Siegel, D. J. *J. Am. Chem. Soc.* **2011**, *134*, 1093–103.
- (8) Radin, M. D.; Tian, F.; Siegel, D. J. *J. Mat. Sci.* **2012**, *47*, 7564–7570.
- (9) Lau, K. C.; Curtiss, L. a.; Greeley, J. J. *Phys. Chem. C* **2011**, *115*, 23625–23633.
- (10) Mo, Y.; Ong, S.; Ceder, G. *Phys. Rev. B* **2011**, *84*, 205446.
- (11) Hummelshøj, J. S.; Luntz, A. C.; Nørskov, J. K. *J. Chem. Phys.* (submitted).
- (12) Ong, S.; Mo, Y.; Ceder, G. *Phys. Rev. B* **2012**, *85*, 081105.
- (13) Kang, J.; Jung, Y. S.; Wei, S.-H.; Dillon, A. *Phys. Rev. B* **2012**, *85*, 035210.
- (14) Mitchell, R.; Gallant, B.; Shao-Horn, Y.; Thompson, C. V. In *ECS Honolulu PRiME 2012*; 2012; Vol. 2952, p. 1105.
- (15) Siegfried, M. J.; Choi, K.-S. *Adv. Mat.* **2004**, *16*, 1743–1746.
- (16) Mitchell, R. R.; Gallant, B. M.; Thompson, C. V.; Shao-Horn, Y. *Energy Environ. Sci.* **2011**, *4*, 2952.
- (17) Vendelbo, S. B.; Johansson, M.; Nielsen, J. H.; Chorkendorff, I. *Phys. Chem. Chem. Phys.* **2011**, *13*, 4486–93.
- (18) Matsuzaki, Y.; Yasuda, I. *Solid State Ionics* **2000**, *132*, 261–269.
- (19) Hohenberg, P.; Kohn, W. *Phys. Rev.* **1964**, *136*, 864.

- (20) Kohn, W.; Sham, L. J. *Phys. Rev.* **1965**, *140*, 1133.
- (21) Mortensen, J. J.; Hansen, L. B.; Jacobsen, K. W. *Phys. Rev. B* **2005**, *71*, 035109.
- (22) Enkovaara, J.; Rostgaard, C.; Mortensen, J. J.; Chen, J.; Dulak, M.; Ferrighi, L.; Gavnholt, J.; Glinsvad, C.; Haikola, V.; Hansen, H. A.; Kristoffersen, H. H.; Kuisma, M.; Larsen, A. H.; Lehtovaara, L.; Ljungberg, M.; Lopez-Acevedo, O.; Moses, P. G.; Ojanen, J.; Olsen, T.; Petzold, V.; Romero, N. A.; Stausholm-Møller, J.; Strange, M.; Tritsarlis, G. A.; Vanin, M.; Walter, M.; Hammer, B.; Hakkinen, H.; Madsen, G. K. H.; Nieminen, R. M.; Nørskov, J. K.; Puska, M.; Rantala, T. T.; Schiøtz, J.; Thygesen, K. S.; Jacobsen, K. W. *J. Phys.: Condens. Matter* **2010**, *25*, 253202.
- (23) Bahn, S. R.; Jacobsen, K. W. *Comput. Sci. Eng.* **2002**, *4*, 56–66.
- (24) Blöchl, P. E. *Phys. Rev.* **1994**, *50*, 17953.
- (25) Blöchl, P. E.; Först, C. J.; Schimpl, J. *Bull. Mater. Sci.* **2003**, *26*, 33–41.
- (26) Hammer, B.; Hansen, L. B.; Nørskov, J. K. *Phys. Rev. B* **1999**, *59*, 7413–7421.
- (27) Chase, M. W. *J. Phys. Chem. Ref. Data* **1998**, *Monograph*, 1–1951.
- (28) Peng, Z.; Freunberger, S. a; Hardwick, L. J.; Chen, Y.; Giordani, V.; Bardé, F.; Novák, P.; Graham, D.; Tarascon, J.-M.; Bruce, P. G. *Angew. Chem. Int. Ed.* **2011**, *50*, 6351–6355.

